Active Metamaterials for Terahertz Communication and Imaging

A dissertation submitted by

Saroj Rout

in partial fulfillment of the requirements for the degree of

Doctor of Philosophy

in

Electrical Engineering

TUFTS UNIVERSITY

May 2016

© 2016, Saroj Rout

Advisor: Professor Sameer Sonkusale

Active Metamaterials for Terahertz Communication and Imaging

by

Saroj Rout

Submitted to the Department of Electrical and Computer Engineering
on April 29, 2016, in partial fulfillment of the
requirements for the degree of
Doctor of Philosophy

Abstract

In recent years there has been significant interest in terahertz (THz) systems mostly due to their unique applications in communication and imaging. One of the primary reason for this resurgence is the use of metamaterials to design THz devices due to lack of natural materials that can respond to this electromagnetic spectrum, the so-called "THz gap". Even after years of intense research, THz systems are complex and expensive, unsuitable for mainstream applications.

This work focuses on bridging this gap by building all solid-state THz devices for imaging and communication applications in a commercial integrated circuit (IC) technology. One such canonical device is a THz wave modulator that can be used in THz wireless communication devices and as spatial light modulator (SLM) for THz imaging systems.

The key contribution of this thesis is a metamaterial based THz wave modulator fabricated in a commercial gallium arsenide (GaAs) process resonant at 0.46 THz using a novel approach of embedding pseudomorphic high electron mobility transistors (pHEMTs) in metamaterial and demonstrate modulation values over 30%, and THz modulation at frequencies up to 10 MHz.

Using the THz wave modulator, we fabricated and experimentally demonstrated an all solid-state metamaterial based THz spatial light modulator (SLM) as a 2x2 pixel array operating around 0.46 THz, by raster scanning an occluded metal object in polystyrene using a single-pixel imaging setup. This was an important step towards building an low-voltage (1V), low power, on-chip integrable THz imaging device.

Using the characterization result from the THz SLM, we computationally demonstrated a multi-level amplitude shift keying (ASK) terahertz wireless communication system using spatial light modulation instead of traditional voltage mode modulation, achieving higher spectral efficiency for high speed communication. We show two orders of magnitude improvement in symbol error rate (SER) for a degradation of 20 dB in transmit signal-to-noise ratio (SNR).

We have computationally demonstrated a novel pictorial modulation technique showing $N/\log_2(N)$ improvement in bandwidth using a N-tile SLM compared to standard spatial modulation using a single-pixel detector.

Finally, we demonstrate a path to realize a terahertz focal plane array (FPA) using a commercial 0.18 μm CMOS foundry process. Through EM simulation and circuit simulation we have demonstrated a metamaterial based THz detectors at 230-325 GHz that can be used in a focal plane array.

Advisor: Professor Sameer Sonkusale
Title: Associate Professor of Electrical and Computer Engineering

Acknowledgments

As I sit to write this acknowledgment, I am fully aware that words will not be sufficient to describe the help and support I have had from people from all walks of life for me to achieve this and yet it's my pleasure to express my gratitude to them. I am also aware that I will invariably leave people who have played a role in this journey and my sincere apologies to them.

I like to first thank my advisor, Professor Sameer Sonkusale, for allowing me to work in this exciting field of metamaterials, a journey which has been more fulfilling than I can show on paper. I am especially grateful to him for having the confidence in me to work in this area of applied physics, knowing very well my background and all my training being in electrical engineering. I am also very thankful to him for giving me the freedom to pursue my ideas, at the same time giving me guidance when I needed to. It is that balance which has nurtured our relationship resulting in this work and I look forward to a life long collaboration in the future. Much more than this work, I will take away some valuable lessons including, his ability to stretch beyond boundaries that are set by norms and persevere to achieve that which seems to be out of your reach. Finally, I thank him for being a great friend.

I want to thank Professor Willie Padilla at Boston College, providing us all the help with our initial effort in metamaterial design, which was extremely valuable for having no prior experience in the field. I deeply thank Dr. David Shrekenhamer at Boston College, for long hours of simulation and experimental help with the initial characterization using the terahertz time domain spectrometer. During those long hours, we developed a friendly relationship that I will cherish forever. I also would like to thank Chris Bingham at Boston College for helping us with initial CST simulation. I thank Professor Richard Averitt and Dr Andrew Strikwerda at Boston University for allowing us to use their THz-TDS system.

During my tenure at Nanolab, I was fortunate to work and be friends with

some amazing people whose friendly nature always made my time in the lab fun and lively. I am grateful to Dr. Ali Mirvakili, Dr. Pooria Mostafalu, Krenar Komoni, Dr. Sungkil Hwang, Dr. Jerry Guo, Saber Bahranifard, Dr. Chirag Sthalekar and Dr. Enjin Fu. I would specially like to thank Dr. Wangren Xu for his help during my Ph.D. qualifying exam and always being a sport for discussions ranging from metamaterials to driving his new Ford Mustang. I am also grateful to Dr. Sam MacNaughton, Dr. Mike Trakimas, Dr. Kyoungchul Park, Ritika Agarwal, Vinay Agarwal, Dr. Pramod Singh, Dr. Shideh Kabiri, Guoqing Fu, Yu Chen, Robert D'Angelo and Meera Punjiya. I was also fortunate to know Professor Valencia Joyner Koomson and enjoyed attending some very interesting design reviews in her group.

My deepest thanks to Dr. Edward Lee at Alfred Mann Foundation, who gave me the chance in 1998 to be part of his research group at Iowa State University starting my wonderful journey in analog circuit design which we later continued as colleagues in Silicon Laboratories. I am deeply grateful to him for being a wonderful mentor, a colleague and a dear friend. I would also like to thank him for being in my thesis committee.

I would specially like to thank Professor Mohammed N. Afsar (Electrical Engineering, Tufts University), Professor Shuchin Aeron (Electrical Engineering, Tufts University) and Professor Xiaocheng Jiang (Biomedical Engineering, Tufts University) for generously providing their time to be in my thesis committee.

I would like to thank the staff in the Electrical and Computer Engineering department for all their help. Special thanks to George Preble and Mike Bauer for their incredible help with all my computing needs. Very thankful to Miriam Santi for getting me through all the administrative tasks.

I thank Jessie Tovera at Qualtre, Inc. for patiently spending hours after hours to help me assemble the spatial light modulator.

I am thankful to my dear friends, Albert K. Lu and Akhil Garlapati, for always encouraging me during difficult times of Ph.D. to push through it and

finish the work.

And, I thank the unknown postman, who mistakenly delivered a copy of the electronics magazine, *Electronics For You*, when I was about eight years old and forever changed my life.

Finally, words will do no justice but it's my duty to thank my parents, my sister, my brother, my sister-in-law and my lovely nephew Aryan for always having faith in me and unconditionally supporting me in whatever I did. I am forever grateful to them and I dedicate this thesis to them.

Contents

List of Figures xi

List of Tables xv

1 Introduction 1

1.1 Towards Closing the "Terahertz Gap" 1

1.1.1 Why is the "Terahertz Gap" Interesting 3

1.1.2 A Brief History of Terahertz Technologies 8

1.1.3 Motivation for this Research: Terahertz Technologies for Imaging and Communication 10

1.1.4 Metamaterials for Terahertz Devices 11

1.2 Introduction to Metamaterials 12

1.2.1 A Brief History 12

1.2.2 Overview of Metamaterials 13

1.2.3 Terahertz Metamaterials 19

1.3 Overview of Terahertz Wave Modulators 21

1.4 Organization of this Thesis 27

2 Background Theory 30

2.1 Plane Waves in a Nonconducting Medium 30

2.1.1 Negative Refractive Index 31

2.1.2 Propagation of Waves in Left-Handed Material 32

2.1.3 Propagation of Waves in Single Negative Medium . . . 33

2.2 Dispersion in Nonconductors 34
2.2.1 Lorentz Oscillator Model for Permitivity 34
2.2.2 Anomalous Dispersion and Resonant Absorption 36
2.3 Metamaterial as a Modulator 39

3 High Speed Terahertz Modulation from Metamaterials with embedded High Electron Mobility Transistors 43
3.1 Design principle of the HEMT controlled metamaterial modulator 44
3.2 Design and fabrication 49
3.3 Experimental Methods 52
3.3.1 Homogenous Parameter Extraction 52
3.3.2 Terahertz Time Domain Spectroscopy 54
3.4 Results and Discussion 55
3.4.1 THz Transmission with DC Biased HEMT 55
3.4.2 High Frequency THz Modulation 59
3.5 Summary 60

4 Low-voltage High-speed Terahertz Spatial Light Modulator using Active Metamaterial 62
4.1 Introduction to Single Pixel Imaging 65
4.1.1 A Brief Historical Perspective 65
4.1.2 Imaging Theory 66
4.1.3 A Review of THz Spatial Light Modulators 68
4.2 Spatial Light Modulator Design and Assembly 73
4.3 Circuit Design for Electronic Control of the SLM 76
4.4 Experimental Setup for Terahertz Characterization and Imaging 78
4.5 Results and Discussions 81
4.5.1 Terahertz Characterization of the Spatial Light Modulator 81
4.5.2 Single-Pixel Terahertz Imaging 83
4.6 Summary 85

5 A Wireless Multi-level Terahertz Amplitude Modulator using Active Metamaterial-based Spatial Light Modulation 87

5.1 Introduction . . . 87

5.2 Results . . . 89

5.2.1 Device Design and Experimental Setup . . . 89

5.2.2 Voltage Modulation Characterization . . . 90

5.2.3 Spatial Modulation Characterization . . . 92

5.2.4 Analysis and Simulation of symbol error rate for a multilevel amplitude modulation THz communication system 93

5.3 Summary . . . 98

6 Pictorial Modulation for High-Speed Wireless Communication 100

6.1 Basic Principle of Pictorial Modulation . . . 101

6.2 Bandwidth improvement for a N-tile Pictorial Modulator . . . 102

6.3 Symbol Error Rate Comparison with Standard Spatial Modulation . . . 103

6.4 Summary . . . 105

7 A Terahertz Metamaterial Detector Focal Plane Array using CMOS Process 107

7.1 A 0.18 um CMOS Foundry Process Technology . . . 109

7.2 Principle of Resistive Self-mixing Detection . . . 111

7.3 Metamaterial based Terahertz CMOS Detector Design . . . 116

7.3.1 Terahertz Detection using Source-Driven Self-Mixing Architecture . . . 116

7.3.2 Circuit Architecture for Terahertz Detection . . . 117

7.4 Metamaterial Design for Terahertz Detection . . . 119

7.5 Design of the Test Chip in 0.18um CMOS Process . . . 123

7.6 Circuit Simulation Results . . . 124

7.7 Summary . . . 126

8 Conclusion **127**

A Electromagnetic Waves **132**

A.1 Helmholtz's Equation 132

A.2 Electromagnetic Waves *are* Transverse 132

Bibliography **134**

List of Figures

1-1 Illustration of the "terahertz gap" 2

1-2 Continuous-wave (cw) terahertz system for inspection applications. 5

1-3 Giga-bit wireless link using 300-400 GHz bands. 7

1-4 Magnetic split ring resonators (SRRs) 15

1-5 Electrically coupled LC resonators (ELCs) 17

1-6 Recent progress THz metamaterial devices 20

1-7 Recent progress in terahertz wave modulators–Optically pumped frequency-agile THz MM. 23

1-8 Recent progress in terahertz wave modulators–Electrically controlled THz MM modulator. 24

1-9 Recent progress in terahertz wave modulators–Gate-controlled active graphene metamaterial. 25

1-10 Recent progress in terahertz wave modulators–Structurally reconfigurable THz MM fabricated on bimaterial cantilevers. . . 26

2-1 Anomalous Dispersion 36

2-2 Reflection coefficient, real and imaginary parts of refractive index as function of frequency for an example material 38

2-3 Dispersion plot for an electrically-coupled LC (ELC) resonator 39

2-4 An ELC based metamaterial as a modulator 40

2-5 An inductance tuned dynamic terahertz metamaterial. 42

3-1 Design and Fabrication details of the metamaterial with embedded pHEMT . . . 45
3-2 An HEMT heterostructure similar to this work and the energy band diagram . . . 47
3-3 A close-up microscope photograph of the metamaterial array near the pad . . . 49
3-4 DC characterization result of the pHEMT . . . 51
3-5 Schematic and example waveform of terahertz time domain spectroscopy (THz-TDS) setup. . . . 53
3-6 THz Transmission with DC Biased HEMT . . . 56
3-7 Comparison between experimental and simulated differential transmissions. . . . 57
3-8 Experimental results from high speed modulation . . . 59

4-1 A compact and low-cost single-pixel THz imaging system . . . 63
4-2 One of the first single-pixel imaging instrument to use binary optical masks based on Hadamard transforms. . . . 65
4-3 Schematic of single-pixel imaging reconstruction from multiplex imaging measurements. . . . 66
4-4 Schematic of a single-pixel terahertz imaging setup using CW pumped high-resitivity silicon as a spatial light modulator. . . . 69
4-5 Schematic of a single-pixel terahertz imaging setup using a SLM based on metamaterial absorber. . . . 70
4-6 A solid-state spatial light modulator for terahertz frequencies (0.36 THz). . . . 71
4-7 Liquid Crystal Metamaterial Absorber Spatial Light Modulator for THz Applications. . . . 72
4-8 SLM design and assembly details . . . 73
4-9 Magnified pictures of the SLM and the metamaterial. . . . 75
4-10 A top level view of the circuit architecture to control the SLM. 76

4-11 Details of the circuit, including the part numbers and the values, used to control one of the SLM's pixel. 77
4-12 Printed circuit board (PCB) for electronic control of the SLM. 78
4-13 Continuous-wave terahertz setup for SLM characterization and imaging 79
4-14 Terahertz characterization of the spatial light modulator . . . 82
4-15 Single-pixel terahertz imaging 83

5-1 Block diagram of a terahertz wireless communication system using multi-level amplitude shift keying (ASK) modulation . . 87
5-2 Characterization of the metamaterial for voltage controlled modulation. 91
5-3 Characterization of the 4-tile (2x2) SLM. 92
5-4 System model for analysis and simulation of symbol error rate (SER) for a multilevel amplitude modulation THz communication system. 94
5-5 Symbol error rate (SER) results 96

6-1 Schematic of a basic pictorial modulation setup. 101
6-2 An example of pictorial symbols for a 2x2 spatial tile. 102
6-3 Bandwidth improvement comparison for SLM and pictorial modulation. 103
6-4 Symbol Error Rate Comparison with Standard Spatial Modulation. 104

7-1 Cross section view and layer information for a 0.18 um CMOS foundry process. 109
7-2 Quasi-static analysis of self-mixing 111
7-3 Non Quasi-static (NQS) analysis of self-mixing 114
7-4 Terahertz CMOS detector design using source-driven distributive mixing 116

7-5 Circuit architecture for terahertz detection. 118
7-6 Metamaterial design and EM simulation results. 120
7-7 S-parameter (S11) and voltage per watt of incident power at the discrete port representing the THz detector. 122
7-8 Design of the test chip in 0.18um CMOS process. 123
7-9 Circuit simulation results. 125

List of Tables

1.1 Summary of recent THz modulator performance characteristics. 28

5.1 Symbol error rate (SER) results from analysis and Monte Carlo simulation 96

7.1 Properties of the CMOS materials used for electromagnetic simulations. 110

7.2 Transistor sizes for the terahertz detector circuit in Fig. 7-5 . . 117

7.3 Design parameters of the four different configurations in the test chip. 124

Chapter 1

Introduction

1.1 Towards Closing the "Terahertz Gap"

The terahertz (THz) regime of the electromagnetic (EM) spectrum is broadly recognized by the frequency range of 100 GHz to 10 THz [1] (where 1 THz corresponds to a frequency of 10^{12} Hz, a wavelength of $300\mu m$ and photon energy of 4.1 meV)[1, 2]. This region, alternatively called the far-IR, lies between infrared light and the microwave frequencies as shown in Fig.-1-1(a).

Most modern devices are based on the response of the electrons in materials to applied EM field and the nature of the response is dependent on the frequency of the EM field. At frequencies few hundred gigahertz and lower, the motion of free electrons forms the basis of most EM devices characterized broadly as *electronics*. It is well known that fundamental sources of power in electronics exhibit decrease in power with increasing frequency. This is a consequence of few main factors such as, characteristic transit distance, for example related to length of a channel in a FET; second is the saturation velocity of carriers in the device, typically 10^5 m/s; and the third being the maximum electric field that is sustainable in a device before breakdown. The accumulation of these limits have led to practical electronic RF sources around

[1] Some define THz to be the submillimeter-wave energy that fills the wavelength range between 1 - 0.1 mm (300 GHz - 3 THz) [3].

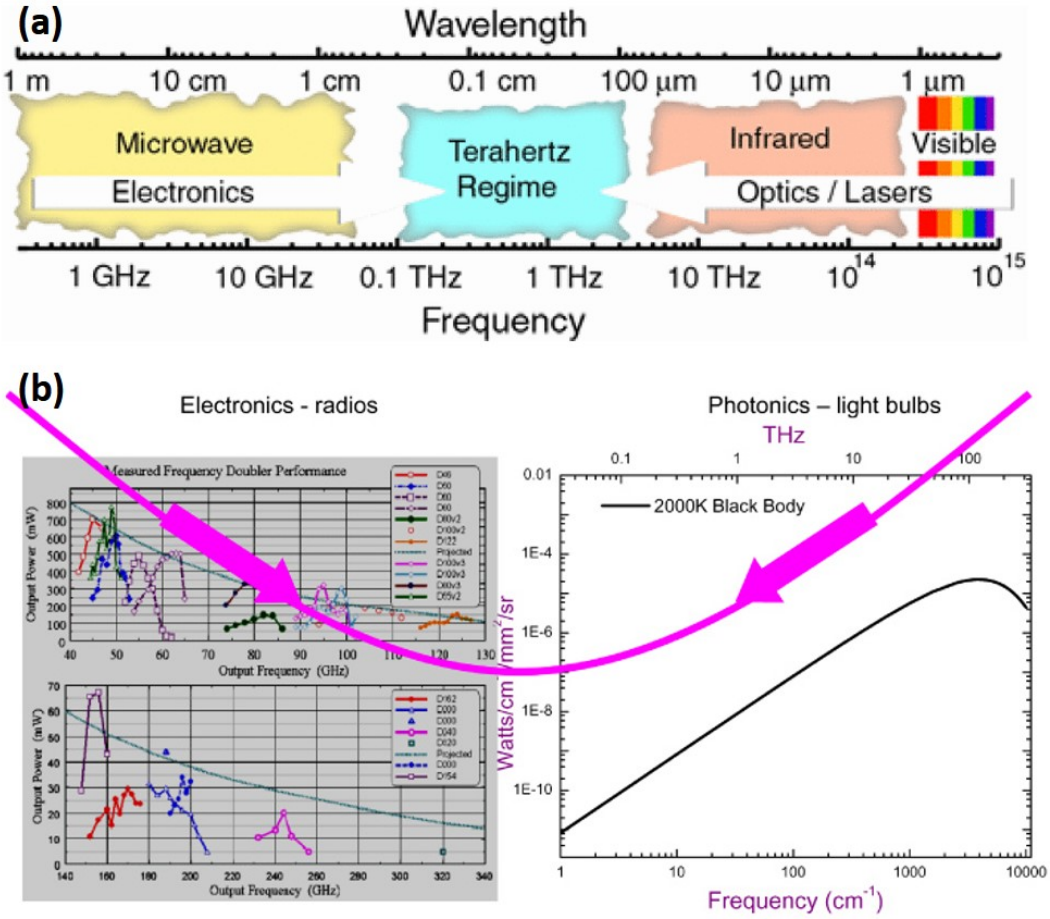

Figure 1-1: The THz gap – (a) THz regime of the EM spectrum extends from 100 GHz to 10 THz, which lies below visible and infrared (IR) wavelengths and above microwave wavelengths[1]. (b) Illustration of the real THz gap - the decline in power as electronics goes to higher frequencies, and photonics goes to lower frequencies[2].

300 GHz with sub-milliwatt power output [4] and much lower power for frequencies near THz, for example, 15 μW at 1.8 THz for a Schottky multiplier chain [5].

On the other hand, at infrared through optical and ultra-violet wavelengths the devices are characterized as *photonics*. It is also well known that photonics sources exhibit decrease in output power with decreasing frequency and the fundamental reason for this is lack of photon energy to meet the band-gap requirements for most photonics sources: for example the longest wavelength lead salt laser diodes do not extend below 15 THz. Thus, in between these two regions, there exists the so-called "THz gap", where the efficiency of electronic and photonics responses tend to taper off as illustrated in Fig.-1-1(b). Because of the lack natural materials that respond to the THz region of EM spectrum, this regime is arguably the least developed and least understood of the EM spectrum[2, 4, 6].

1.1.1 Why is the "Terahertz Gap" Interesting

The past three decades have seen a revolution in THz systems motivated in part by vast range of unique applications ranging from imaging, sensing to spectroscopy[7]. Astronomy and space research has been one of the early drivers for THz research because of the vast amount spectral information available concerning the presence of abundant molecules such as oxygen, water and carbon monoxide in stellar dusts, comets and planets [8]. The application of THz sources in astronomy is as local oscillator sources for submillimetre-wave heterodyne receivers used to perform high-resolution spectroscopy [3]. Back on Earth, the two most pervasive applications for terahertz technology have been in the areas of plasma fusion diagnostics and gas spectroscopy[9]. THz spectroscopy development has been a active research topic due to its potential in extracting material characteristics that are unavailable when using other frequency bands. Terahertz spectroscopy has been used to determine the carrier concentration and mobility of doped semiconductors such as GaAs and silicon

wafers[10, 11] and high-temperature superconductor characterization[12]. THz systems have been developed for biomedical applications that are facilitated by the fact that the collective vibrational modes of many proteins and DNA molecules are predicted to occur in the THz range[13]. A further biomedical application of THz systems is the THz biosensor. A simple biosensor[14] has been demonstrated for detecting the glycoprotein avidin after binding with vitamin H (biotin) using the technique of differential THz-TDS.

In recent years, terahertz (THz) imaging has captured significant interest due to its ability to penetrate most dielectric materials and non-polar liquids [15, 16]. Its harmless interaction with human tissue has resulted in wide range of applications such as bio-detection[17], security screening[18], illicit drug detection[19] and skin cancer detection[20], to name a few. Another attraction of THz imaging is largely due to the availability of phase-sensitive spectroscopic images, which holds the potential for material identification or 'functional imaging'. THz systems are ideal for imaging dry dielectric substances including paper, plastics and ceramics. These materials are relatively non-absorbing in this frequency range, yet different materials may be easily discriminated on the basis of their refractive index, which is extracted from the THz phase information. Many such materials are opaque at optical frequencies, and provide very low contrast for X-rays. THz imaging systems may therefore find important niche applications in security screening and manufacturing quality control[21]. Interest in using THz imaging to study cellular structure is also increasing[22].

Another emerging area for the terahertz regime is high speed wireless communication. The demand for high speed wireless access is increasing due to large amounts of data needed for new emerging applications such as the consumer market that is already demanding 20, 40 and 100 Gbit/s wireless technologies for Super Hi-Vision (SHV) and Ultra High-Def (UHD) TV data[23]. Terahertz (THz) carrier frequencies will offer the advantage of higher data speed, sub-millimeter antenna size and short range security especially suit-

able for portable devices. Although they are susceptible to atmospheric loss, THz digital communication systems have been demonstrated near certain windows, especially around the 300-400 GHz range that has shown promise for high bit-rate data transmission [23–25].

Next we show two examples of terahertz systems to highlight the significance of this frequency regime.

Continuous-wave Terahertz System for Inspection Applications

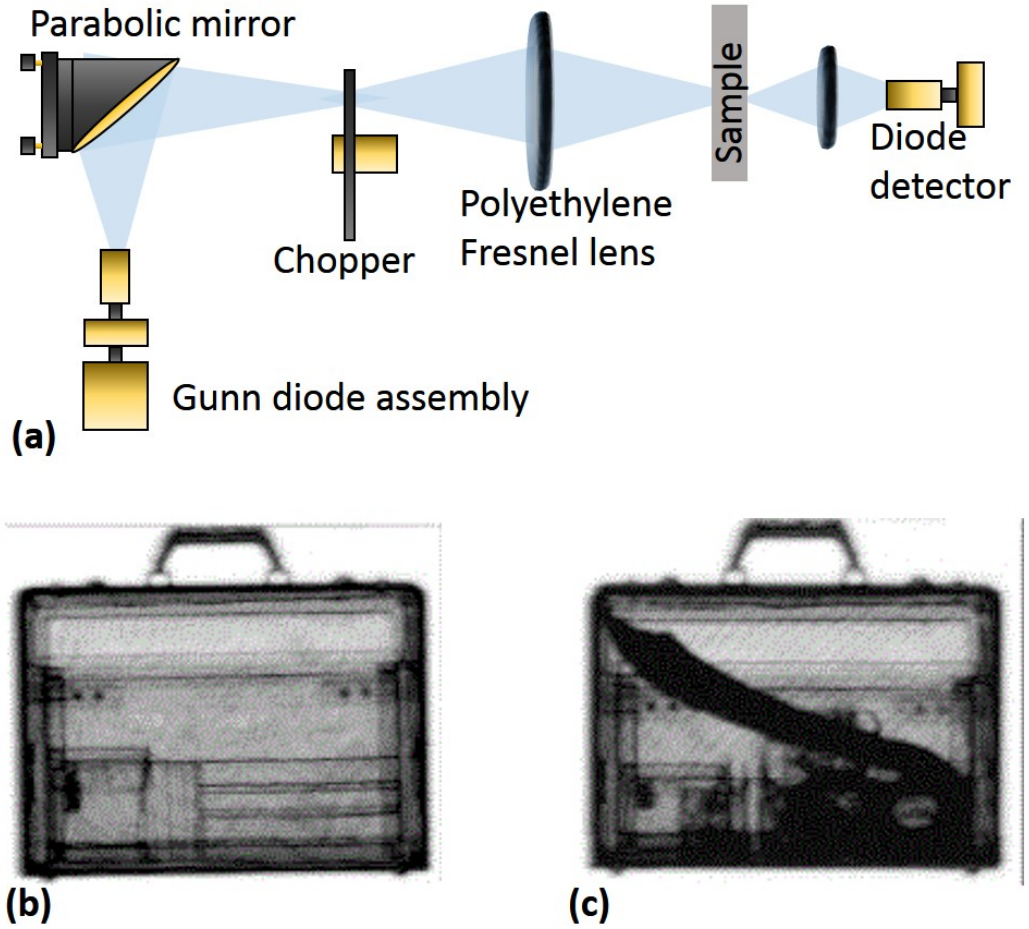

Figure 1-2: (a) Schematic diagram of the imaging system in transmission geometry. (b) Transmission geometry 0.2 THz cw image of an empty leather briefcase. (c) Image of the same briefcase holding a large knife and various harmless contents such as a compact disc, a video cassette, and audio cassette and pens [18].

The unique property of terahertz waves to penetrate most dielectric ma-

terial makes them an ideal candidate for security screening applications. One such system, a compact continuous-wave (cw) 0.2 THz imaging system using entirely electronic generation and detection with a minimal number of components is shown in Fig. 1-2(a) [18]. The system consists of a frequency-doubled Gunn diode oscillator with an output power of 12 mW as a source, and a Schottky diode as the detector. After being emitted by the Gunn diode, the beam is focused by a parabolic mirror to a 4 mm spot where it is modulated by an optical chopper at 1.2 kHz. The chopped beam is focused twice, one on the sample and again on the diode detector by a pair THz optics. The sample is mounted on a translation stage to raster scan the object.

Fig. 1-2(b,c) shows a 0.2 THz cw scan of a standard size leather briefcase, both empty and containing benign and suspicious items. The strengths of the system can be immediately seen: objects can be recognized fairly easily, and since the radiation involved is nonionizing, it poses little threat to human beings.

Giga-bit Wireless Link Using 300-400 GHz Bands

Because of demand for high-speed wireless access, there is an urgency for designing wireless systems with data speeds of more than 1 Gbit/s. Fig. 1-3(a) shows a block diagram of a 300-400 GHz band system using a photonics-based transmitter [26]. This system is intended for use in short-distance ($\sim$0.5 m) applications. An optical RF signal is generated by heterodyning the two wavelengths of light from the wavelength-tunable light sources. The optical signal is digitally modulated by a optical intensity modulator driven by a pulse pattern generator (PPG). Finally, the optical signal is converted to an electrical signal by the modified Uni-Traveling-Carrier-Photodiode (UTC-PD). The THz wave is emitted to free space via a horn antenna with a gain of 25 dBi, and it is collimated by a 2-inch-diameter Teflon lens. The receiver consists of a Schottky barrier diode and an IF filter followed by a low-noise pre-amplifier and a limiting amplifier. The envelope detection is performed by the Schottky-

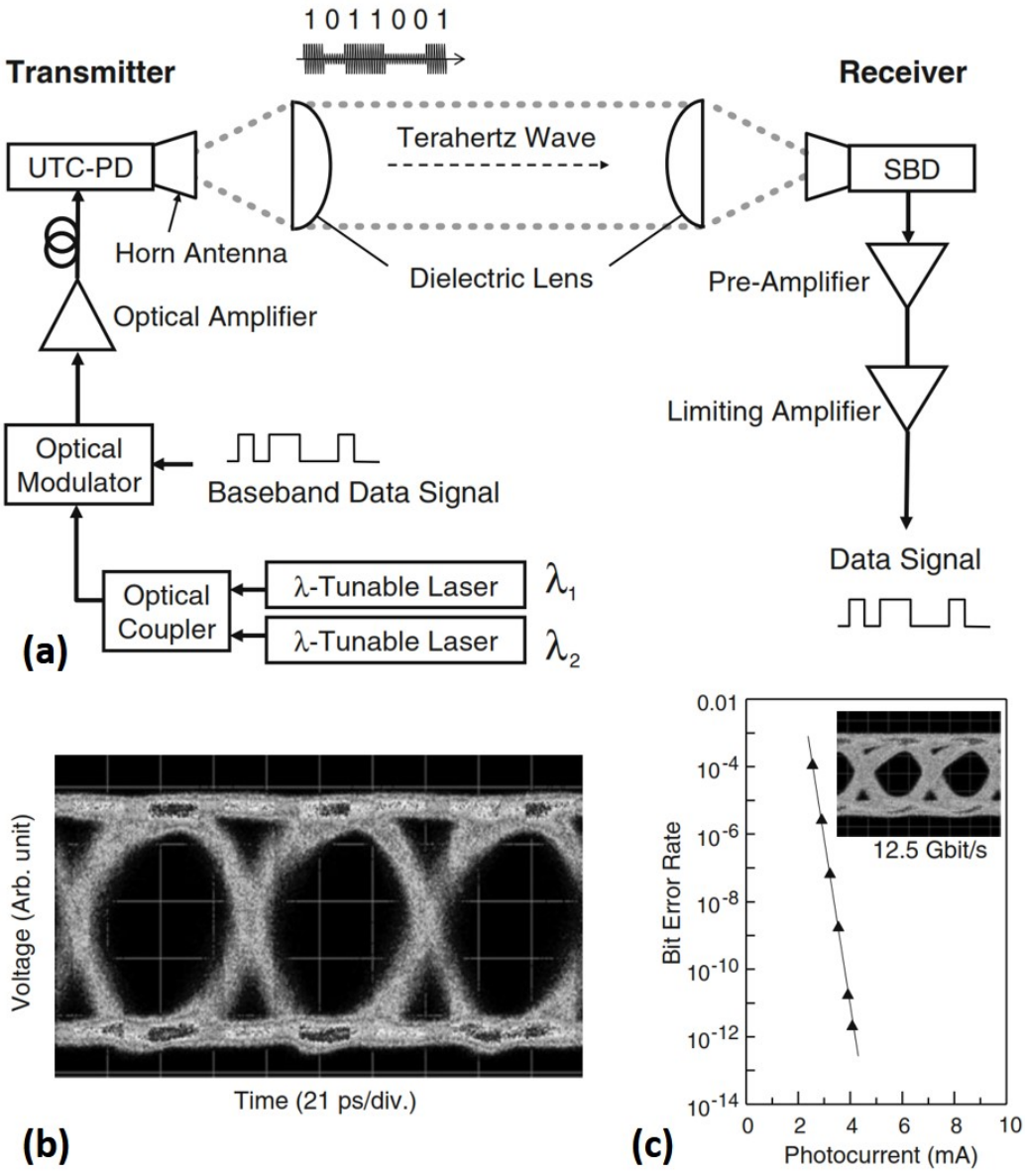

Figure 1-3: Giga-bit wireless link using 300-400 GHz bands [26]. (a) Block diagram of the wireless link using photonics-based terahertz-wave transmitter. UTC-PD: Uni-Traveling-Carrier-Photodiode. SBD: Schottky-Barrier-Diode. (b) Eye diagram at 14 Gbit/s. (c) BER characteristics at 12.5 Gbit/s.

Barrier-Diode (SBD) for amplitude shift keying (ASK) modulation.

Fig. 1-3(b) shows the eye diagram at 14 Gbit/s which is evidently error-free from the clear eye opening. Fig. 1-3(c) shows bit-error rate (BER) characteristics at 12.5 Gbit/s with a carrier frequency of 300 GHz. The horizontal axis corresponds to the photocurrent of the transmitter.

With 14 Gbit/s data rate, it is clear that we need terahertz carrier frequency for the demand we have in hand and these examples are promising for the next generation wireless technology.

1.1.2 A Brief History of Terahertz Technologies

For terahertz imaging, sources and detectors have been the focus of research since the 1960s and the early 1970s. A powerful source developed for terahertz radiation was the HCN laser operating at 1.12 THz [27]. Terahertz imaging got its first boost from the development of far-infrared gas laser and the schottky diode harmonic mixer in the mid-1970s by Hartwick *et al* [28]. At roughly the same time, the advent of lasers motivated research in far-infrared generation using the difference-frequency generation in non-linear crystals [29], which served as the seed for the development of terahertz time-domain spectroscopy (THz-TDS) [30–34], which still serves as a system of choice for high dynamic range THz spectroscopy. The THz-TDS system generated a great deal of interest in THz imaging after first images acquired using the THz-TDS was reported in 1995 [35]. Since the early days, the field has seen a rapid expansion in new technologies for terahertz sensing [3] including time-of-flight imaging [36], variety of different tomographic and synthetic aperture imaging [37–39], multi-element detector schemes, both microbolometer arrays [40] and electro-optic sampling with high-performance CCD cameras [41].

The semiconductor-laser model for terahertz generation has always been a topic of research interest, given their tremendous success in visible and near-infrared frequency range. Because of the lack of appropriate interband materials, in the past, artificially engineered materials to obtain the desired tran-

sitions has been natural route of pursuit for many years by researchers to create terahertz devices. This pursuit led to the demonstration of the first terahertz quantum-cascade (QC) laser in 1988 [42] and shorter wavelength of 4 μm (75 THz) in 1994 [43]. It was only in October of 2001 that the first QC laser with a photon energy less than the semiconductor optical phonon energy was demonstrated at 4.4 THz (67 μm) [44]. Since then, significant research has led to QC lasers demonstrating spectral coverage from 0.84–5.0 THz [45]. One of the major limitations that has prevented QC lasers from being a mainstream technology is the inability to deliver THz power at room temperature. But recent work in 2012 has demonstrated terahertz QC laser operation up to 200 K [46] and a recent work by Li et.al. in 2014 demonstrating powers >1W [47], showing a bright future for QC lasers and maybe the technology to fill the "THz gap". The success of QC lasers are already evident from their wide range applications: such as local oscillator sources for submillimetre-wave heterodyne receivers used to perform high-resolution spectroscopy in astronomy [3, 48] and in many high performance imaging applications [49–52], including a real-time, video-rate terahertz imaging application [45].

Although short range communication using THz waves was first speculated by Gebbie in 1970[53], we are still far from realizing systems for our consumer wireless needs due to enormous challenges associated with the technology and the medium as well. Due to the increasing demand for high speed wireless communication in the last decade, we are starting to see communication systems developed for the THz regime. A photonics-based 120 GHz system has been successfully demonstrated multi-channel transmission of uncompressed high-definition TV signal over a distance of 100m [54, 55]. With progress in the semiconductor IC technologies, all solid-state THz communications systems are being developed which contributes to reduction in size, weight and cost together with ease of operation [56]. A trial use of this system was conducted within the live broadcast of the 2008 Olympic Games in Beijing by Nippon Telegraph and Telephone Corporation (NTT) and Fuji Television Network

Inc. Towards 20+ Gbit/s wireless systems using the 300-400 GHz band has been experimentally demonstrated using a photonics-based THz system over a short range, suggesting possible utilization of the band for multi-channel gigabit links [26]. Another unique advantage with THz wireless communication is it's secure at a physical level for several reasons: highly directional beams compared to microwave communications, less scattering of radiation compared to IR wireless, limited propagation distance due to atmospheric attenuation, encryption of the beam, large channel bandwidth for spread spectrum techniques which enable antijamming and low probability of detection systems, and hidden THz signals in the background noise.

1.1.3 Motivation for this Research: Terahertz Technologies for Imaging and Communication

In spite of the intense research activity in THz devices and systems, we are still ways from bringing these technologies to the main stream due to the cost and complexity of the systems. These imaging and communications systems are often built around photonics based system that are complex, large and expensive, unsuitable for mainstream applications. The ones using solid-state devices often use custom and exotic fabrication process which makes it expensive and complex as well. To move towards closing the "THz gap", these THz systems need to be all solid-state based, be able to operate in the industrial temperature range ($-40°C$ to $+85°C$) and be manufactured using consumer grade integrated circuit process which will make it small, cheap and additionally allows us to add very complex control and signal processing systems on the same integrated circuit.

Also, research effort in THz technologies have focused mostly on THz sources and detectors. THz wave modulators, a key component in THz systems, are still in their infancy.

The motivation of this research is to build all solid-state terahertz (THz)

devices, for imaging and communication, in a commercial integrated circuit (IC) technology that can be mass produced at very low cost and operate under electrical and environmental condition same as consumer grade devices. One such device is a terahertz wave modulator that can be used in terahertz communication system to modulate free-space THz waves based on data stream. The same technology can also be used in THz imaging to create spatial light modulator (SLM) for compressed imaging.

1.1.4 Metamaterials for Terahertz Devices

Metamaterials (MMs) are macroscopic composites of periodic structures whose electromagnetic (EM) response can be designed over a large portion of the EM spectrum by, to first order, simply scaling the dimensions of the periodic structures. MMs are essentially effective mediums requiring the periodic structures to be fraction of the wavelength ($\sim \lambda/10$) of the incident EM wave. For THz MMs, the unit cells are few tens of microns ($3\mu m - 300\mu m$) with critical feature sizes of few microns. They also offer the two critical materials for construction, non-conducting substrate and metal layers separated from the substrate using dielectrics. These scales and the materials, make them the perfect candidate for conventional microfabrication using a large pool of commercially available integrated circuit (IC) technologies. In last decade we have seen a rapid increase in metamaterial devices created for the THz regime using planar IC fabrication technologies for a wide range applications including absorbers, quarter waveplates, switches/modulators, structurally reconfigurable MMs and MMs with memory effects[1].

1.2 Introduction to Metamaterials

1.2.1 A Brief History

Veselago's 1968 seminal work on simultaneous negative values of permittivity(ϵ) and permeability(μ)[57], proposed a systematic analysis of electromagnetic behaviors in left-handed materials(LHM) predicting some exotic EM behaviors from them. Although some these behaviors like negative refraction and backward-wave media had been discovered theoretically much earlier [58–61], Veselago also showed some new features like reversed Doppler shift and backward Cerenkov radiation in LHM. Veselago's work [57] went literally unnoticed for three decades until in 1999 Smith, et.al.[62], trying to model plasmons at microwave frequencies, stumbled upon negative refractive index artificial material [63]. Since there was no such material known to mankind till that time, their work was received with utmost skepticism and initially rejected from being published. With experimental results in their hand, they were determined to find prior work, if any, and thus stumbled upon Veselago's work[57]. Since then, metamaterial research has exponentially grown and expanded into fields previously un-imagined by the pioneers themselves. This includes negative refractive index [64–68], super-lensing [69–72], perfect absorbers [73, 74], cloaking [75–78], and more generally, coordinating transformation materials [79–82]. Bulk of the research has been focused on passive metamaterials, sub-wavelength metallic inclusions in dielectric material, allowing for a predetermined resonant response of the electrical permittivity or magnetic permeability. Although passive metamaterials have given us the power to engineer material properties of our choice, they cannot be changed dynamically. For many potential applications, it would be desirable to control these properties through means of electrical, optical, mechanical, temperature methods or any combinations of them.

In 2006, for the first time, dynamical control of the electrical response of the split ring resonators (SRRs), a basic building block of metamaterials, was

demonstrated by Padilla, et.al. [83], through photo-excitation of free carriers in the substrate. Later that year, Chen, et.al. [84] also demonstrated electrical control of terahertz metamaterials using dynamic substrate bias voltage. Since then, research into active and tunable metamaterials have grown and expanded into fields previously unrealized using passive metamaterials. This includes photo-controlled [85, 86], electrical controlled [87, 88], temperature controlled [89], MEMS controlled [90] metamaterials. Although these dynamically controlled metamaterials have expanded the scope of application, they are still limited by slow response to the control method. It is due to the fact that the entire substrate of the metamaterial is controlled resulting in large device capacitance [87] in case of electrically controlled metamaterials and similar limitations in other control methods. To alleviate some of these limitations and expand into the next frontier of metamaterial research, it is required to embed and interface solid-state devices locally into every metamaterial unit.

1.2.2 Overview of Metamaterials

Metamaterials are macroscopic composite of periodic or non-periodic sub-wavelength structures, whose EM property is primarily a function of the cellular structure allowing great flexibility in creating new effective materials, unavailable in nature. The sub-wavelength inclusions are like the atomic particle in conventional material and the EM response of the metamaterial is characterized by the effective permittivity(ϵ) and permeability(μ), determined in the homogenization of the periodic inclusions by averaging the local fields [91, 92]. In the early days, the term metamaterial referred to negative-refractive index material (NIM), a phenomena first postulated by Veselago in 1968 [57]. He theoretically predicted materials with simultaneous negative values of the ϵ and μ, hence giving an index of refraction, $n = \sqrt{\epsilon_r \mu_r}$ that is less than zero, a material not naturally found even today. Along with negative-refractive index, Veselago also predicted other exotic properties such as reverse Cerenkov

radiation, reverse Doppler shift, and opposite phase and group velocity, among others [57]. In it's long history, metamaterials, Left-Handed materials (LHM), NIM, double-negative materials (DNG), and backward-wave materials have been regarded as the same terms. But today, the term metamaterial has a much broader scope than LHM. They constitute any artificial EM materials constructed from sub-wavelength periodic or non-periodic inclusions resulting in a user defined effective ϵ, μ or both.

Design of negative-index metamaterial (NI MM) constitutes magnetic and electric elements that respectively give rise to negative ϵ and negative μ. Various types of sub-wavelength resonators for building MMs have been designed and demonstrated, for example, thin metallic wires [93, 94], Swiss rolls [95, 96], pairs of rods and crosses [97, 98], fishnet structures [99, 100] and split-ring resonators (SRRs) and electric variants of it [63, 74, 84, 90, 91, 96, 101–105]. Among these resonator structures, the SRRs and their variants are the canonical sub-wavelength structures used in majority of the metamaterials. In the next two sections, we will discuss design techniques to realize negative ϵ or negative μ metamaterials.

Magnetic Split Ring Resonator (SRR)

The first artificial magnetic material was demonstrated in the microwave frequency range by Pendry et.al. in 1999 [96] using an 'magnetic atom' very similar to a frequently-used split ring resonators (SRRs) arranged in an array as shown in Fig.1-4(a). The SRR array is built from non-magnetic conducting sheets on a FR4 dielectric whose effective material response is shown in Fig.1-4(b,c) that is determined solely by the SRR geometry. The general form of the frequency dependent permeability of the SRR has the generic form [96, 107]

$$\begin{aligned} \mu_{eff}(\omega) &= 1 + \frac{F\omega^2}{\omega_0^2 - \omega^2 - i\gamma\omega} \\ &= \mu_{eff}^{'} + i\mu_{eff}^{''} \end{aligned} \tag{1.1}$$

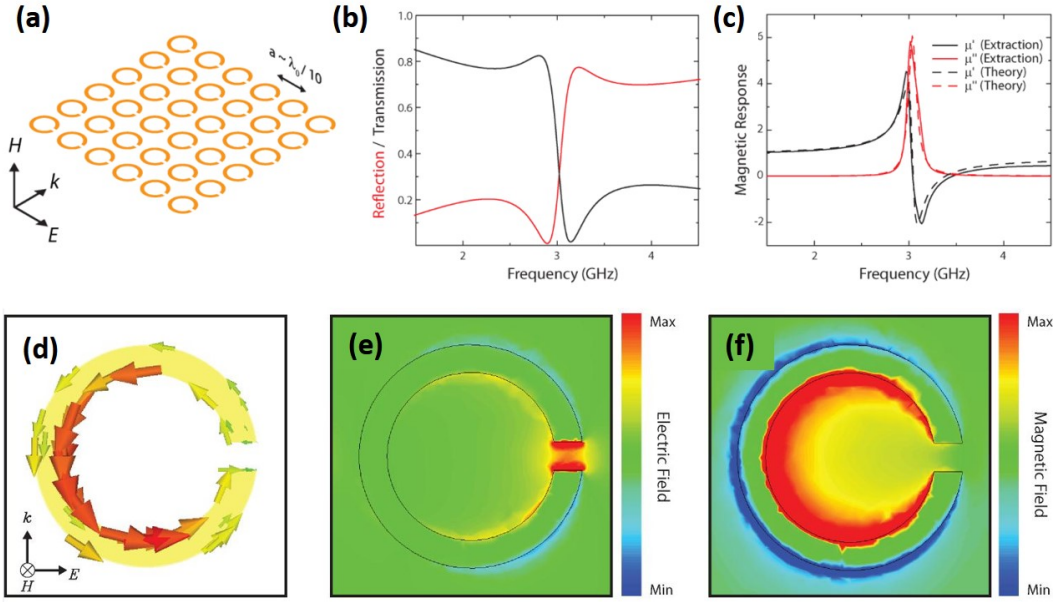

Figure 1-4: Magnetic split ring resonators (SRRs). (a) Incident electromagnetic wave propagates across the SRR array, where the element spacing a is 1/10 of the free space wavelength λ_0. (b) The simulated reflection and transmission for an SRR with $a = 10mm$. (c) The extracted magnetic response (solid curves) from simulation results shown in (b) and the response when fit with the theoretical model listed in Eq.-1.1, where $F = 0.20$, $\omega_0 = 2\pi \times 3.03$ GHz, and $\gamma = 0.10s^{-1}$. (d-f) Resonant field distributions in the plane of the metamaterial where (d) shows the resonant current density (e) the maximum electric field, and (f) plots maximum magnetic field.[106]

where F is a geometrical factor, ω_0 is the resonance frequency and γ is the resistive damping factor. The quality factor of the resonator can be expressed as $Q = \omega_0/\gamma$ where γ is the bandwidth of the resonator. The Q is related inversely to the resistive damping factor (γ). If the Q of the resonator is high enough, the *real* part of equation (1.1) will result in a negative value around the resonant frequency, yielding an effective negative magnetic response from the SRR array.

In it's simplest form, the SRR can be thought of as a inductor-capacitor (LC) resonator, with a resonance frequency of $\omega_0 \approx \sqrt{1/LC}$, where the inductance results from the circular current path in the split-ring and the capacitance from the dielectric in the split-gap. When a time varying magnetic field polarized perpendicular to the plane of SRR is incident on the material as shown in Fig.1-4(a), it induces a circulating current according to Faraday's law that causes charges of opposite polarity to accumulate at the split gap of the split ring, thereby producing a strong enhancement of electric field as shown in Fig.1-4(e). For frequencies below ω_0, the current in the loop and the incident field are in phase, resulting in a positive response. However, when the frequency of the **B**-field is in the proximity of the resonant frequency, ω_0, the currents in the SRR lag thus resulting in a negative response. Fig.1-4(d-f) shows the resonant current, electric, and magnetic field distributions respectively for the excited SRR.

The LC resonator model is very simple but powerful design tool for achieving an initial resonant response very close to the desired frequency by simply scaling these variables. In practice, other parameters such as frequency dependent dielectrics and scattering effects will affect the resonant frequency. EM simulators are used to iterate and fine tune the resonant frequency to the desired one. This description is also helpful for designing dynamic metamaterials, wherein majority of research focuses on different mechanisms of controlling the capacitance associated with the split gap.

A potential limitation of SRRs to be used for planar THz devices is that the

magnetic field needs to be perpendicular to the SRR plane for full magnetic coupling. However the EM plane waves are usually incident normal to the planar SRR structure with the magnetic field lying in the SRRs plane, which does not excite the magnetic resonance directly. Variants of the SRR which respond to the electric field instead, allowing normal incident of the plane wave, is introduced in the next section.

Electrically Coupled LC Resonator (ELC)

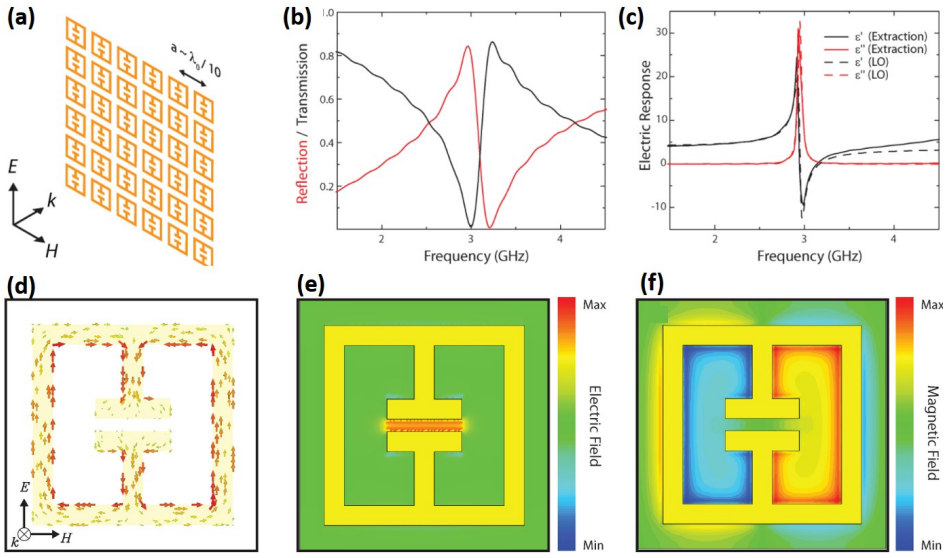

Figure 1-5: Electrically coupled LC resonators (ELCs). (a) Incident electromagnetic wave propagates normal to the ELC array, where the element spacing a is 1/10 of the free space wavelength λ_0. (b) The simulated reflection and transmission for an ELC with $a = 10mm$. (c) The extracted electric response (solid curves) from simulation results shown in (b) and the response when fit with the theoretical model listed in Eq.-1.4, where $\epsilon_\infty = 4.3$(FR4), $F = 0.55$, $\omega_0 = 2\pi \times 2.96$ GHz, and $\gamma = 0.05s^{-1}$. (d-f) Resonant field distributions in the plane of the metamaterial where (d) shows the resonant current density (e) the maximum electric field, and (f) plots maximum magnetic field.[106]

Researchers have been constructing artificial EM materials with $\epsilon < 0$ (artificial plasmas) for decades now [108–111]. The technology has been reintroduced in recent years with more physics-oriented understanding [93, 112]. The first artificial electric material was demonstrated in the microwave frequency range by Pendry et.al. [93], using the straight wire medium, a principle first

demonstrated by Rotman in 1962 [109]. The generic form of the frequency dependent permittivity, in naturally occurring materials, can be written as a Drude-Lorentz relation:

$$\epsilon_{eff}(\omega) = 1 - \frac{\omega_p^2}{\omega^2 - \omega_0^2 - i\gamma\omega} \tag{1.2}$$

where plasma frequency, ω_p^2, is

$$\omega_p^2 = \frac{4\pi n e^2}{m^*} \tag{1.3}$$

and n is the carrier density, e is the charge of an electron, γ is the damping factor and m^* is the effective mass of carriers. In artificially EM materials, including MMs, n and m^* are related to the geometry of the lattice, giving MMs much greater flexibility than conventional materials.

For planar metamaterial design, an electrical variant of the SRR, termed Electrically coupled LC Resonator (ELC) as shown in Fig. 1-5(a), has become the canonical structure for implementing negative values of permittivity (ϵ) for frequencies ranging from low RF to the optical [63, 74, 84, 90, 91, 96, 101–105]. One of the fundamental reason for using an electric structure such as the ELC is, so that the plane EM wave can be incident normal to the planar structure as shown in 1-5(a) with the electric field polarized perpendicular to the split gap. The modified symmetric geometry compared to conventional SRRs, enables them to effectively cancel the magnetic moment and only couple to the incident electric field vector as shown in Fig.1-5(d-f) [113, 114].

The electric response is shown in Fig.1-5(c) similar to that of the magnetic response of the SRR in Fig.1-4(c), where ϵ_{eff} can be expressed as [91, 115, 116]

$$\begin{aligned} \epsilon_{eff}(\omega) &= \epsilon_\infty - \frac{F\omega^2}{\omega^2 - \omega_0^2 - i\gamma\omega} \\ &= \epsilon_{eff}^{'} + i\epsilon_{eff}^{''} \end{aligned} \tag{1.4}$$

where ϵ_∞ is the frequency independent dielectric permittivity in the supporting dielectric substrate (eg. FR4 or GaAs substrate). F is a geometrical factor, ω_0 is the resonance frequency and γ is the resistive damping factor. As in the case of SRRs, if the Q of the resonator is high enough, the *real* part of equation (1.4) will result in a negative value around the resonant frequency, yielding an effective electric response from the ELC array.

1.2.3 Terahertz Metamaterials

As briefly introduced in section 1.1.4, metamaterials (MMs) are a suitable candidate for planar terahertz (THz) devices using conventional microfabrication process because of their unit cell sizes in the order of tens of microns ($3\mu m - 300\mu m$) and provides the base materials for construction, non-conducting substrate and metal layers, which results in cost effective, highly efficient means of production. The added benefit of using conventional microfabrication process, especially integrated circuit (IC) design processes, it allows researchers and engineers to select a vast range of solid-state devices to dynamically control the response as well as spectral selectivity of MM devices. Both of which are useful properties to develop novel THz imaging and communication devices previously not possible with available technologies.

This has allowed researchers in the last decade to create MM devices for terahertz frequencies that are not easily obtainable in nature, most notably a magnetic response that is particularly rare at THz frequencies. One of the first THz MM was experimentally demonstrated by Yen *et al.* in 2004, showing a strong magnetic response at 1 THz, using a single planar double SRR array as shown in Fig.1-6(a) [117]. Limitation to normal incident wave with planar magnetic SRRs is explained in Sec.1.2.2.

Although SRRs can exhibit either purely negative electric or magnetic response for a chosen polarization of electric or magnetic field, the electric and magnetic resonances are coupled, resulting in a complex bianistropic EM response. A number of alternative SRR structures have been designed to

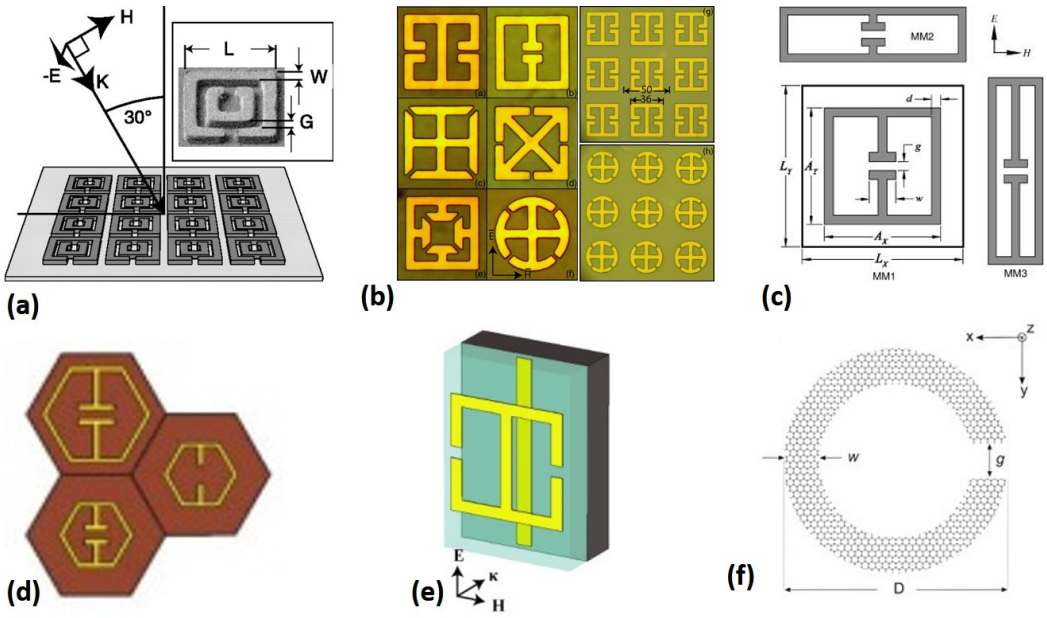

Figure 1-6: Recent progress THz metamaterial devices (a) Magnetically coupled SRRs [117]. (b) THz electric MMs with symmetry geometries [114]. (c) Tuned coupling between the LC and dipole resonances [118]. (d) Electric MMs with multiple resonances [119]. (e) Schematic of a THz MM absorber [74]. (f) Graphene based split ring resonator [120]

suppress the magnetic response in favor of a pure electric response [114], as shown in Fig.1-6(b).

Along with the fundamental mode of LC resonance in the SRRs or ELCs, higher mode dipole resonances associated with the sidebars of the SRR or ELC is present and may couple strongly with the fundamental mode depending on the design. The dipole resonance can be tuned by changing the distance between SRR sidebars, which are parallel to the electric field [118], as shown in Fig.1-6(c). Tuning the dipole resonance independent to the LC resonance is very important in applications where resonance reshaping due to LC-dipole coupling is undesirable.

One of the drawbacks of metamaterial devices is the narrow spectral range making it unsuitable for broadband applications. Efforts have been made to broaden the bandwidth by packing two or more resonators in a unit cell with different resonances [119], as shown in Fig.1-6(d).

While most applications require the minimum loss related to the MMs,

conversely, for many applications it would be desirable to maximize the loss. This is particularly important for THz frequencies where finding naturally occurring materials as an absorber for a desired frequency is difficult. MM-based absorbers have been demonstrated with a high absorptivity at terahertz frequencies [73, 74, 115, 121]. A single unit cell consists of an electrical ring resonator and a magnetic resonator as shown in Fig.1-6(e). The electric resonator is a standard ELC structure to cancel the magnetic moment and the magnetic resonator is realized by combining the center wire of the electric resonator on the top layer with a cut wire below it using a bottom layer metal. The EM responses are tuned to match the free-space impedance and minimize the transmission at a specific frequency.

The major limitations in developing high frequency metamaterial devices is the loss associated with the metal layer and the dielectric as well. Recently, studies have speculated the use of graphene to construct SRRs [120], as shown in Fig.1-6(f), allowing high confinement, long lifetimes and fast electrical tunability compared to the conventional gold structures. Recently, active circuits have been used to demonstrate loss compensation in microwave metamaterials [122, 123], but application of the same principle in terahertz frequencies is difficult and yet to be realized.

1.3 Overview of Terahertz Wave Modulators

Terahertz (THz) wave modulator is a key component in THz systems for wide range of applications ranging from imaging to communication. A key to high speed communication using THz wave is fast and efficient amplitude and/or phase modulator which is used to encode information in the carrier wave. It is also an important component in a single sensor THz imaging system where an array of THz wave modulators in the object plane is used to spatially encode the terahertz wave before being directed to the single sensor [124, 125]. Set of unique single sensor measurements corresponding to a set coded apertures is

used to reconstruct the image using a computational method known as compressed sensing (CS) [126]. A detailed discussion of such an imaging system is presented in section 4.1.

Apart from amplitude and phase control, modulators can be used to control polarization state, spatial propagation direction, pulse shape, pulse length and many more characteristic properties of electromagnetic waves. While active modulators are well established and considered standard devices in the optical realm, the THz frequency regime is still in great demand for highly efficient, fast and versatile active wave modulators.

Modulators can be categorized by the physical quantity they control, as e.g. amplitude, phase, pulse length and shape, spectrum, spatial and temporal properties or by the technique or material system which is employed to modulate the wave. In most cases, modulators manipulate multiple properties of the THz wave at once, either on purpose or as a consequence of an undesired side effect. This section will briefly review some of the technologies developed till date, including metamaterials, for terahertz wave modulators.

In the past, semiconductors have been used for all-optical modulation of electromagnetic (EM) waves. Generally, laser pulses are incident on the semiconductor producing free carriers for time a period associated with the recombination time (τ). Typically, the plasma frequency (ω_p) of the carriers are above 1 THz ($\omega_p > 2\pi \times 1THz$). Then, the surface looks "metallic" for frequencies below 1 THz acting like a reflective surface for time scales up to $t = \tau$. THz wave, co-incident on this area of high reflectivity, is thus modulated. This technique has been used since 90's to create THz modulators [127, 128]. In a more recent approach, spatially modulated laser light was used to induce one- and two-dimensional, tunable optical gratings in high-resistivity silicon to modulate terahertz waves [129, 130]. The same concept can applied to metamaterials (MMs) where, the resonance frequency of the metamaterial element is shifted by changing the capacitance of the split gap. The technique was used by Chen *et al.* to demonstrate a frequency-agile MM device, which

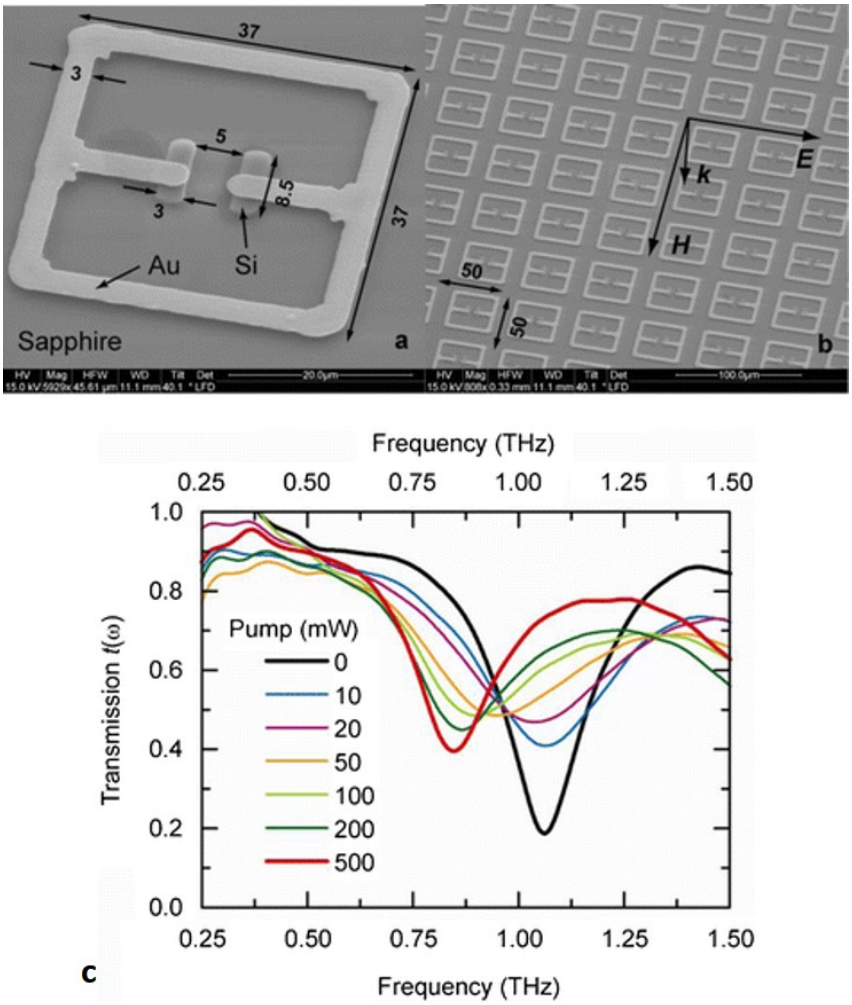

Figure 1-7: Optically pumped frequency-agile THz MM. SEM images of (a) An individual unit cell and (b) a periodically patterned square array. (c) Experimental measurements as a function of photoexcitation power [85].

is able to shift the center resonance frequency by 20% using external optical pumping [85], SEM photograph and measurement results shown in Fig.1-7.

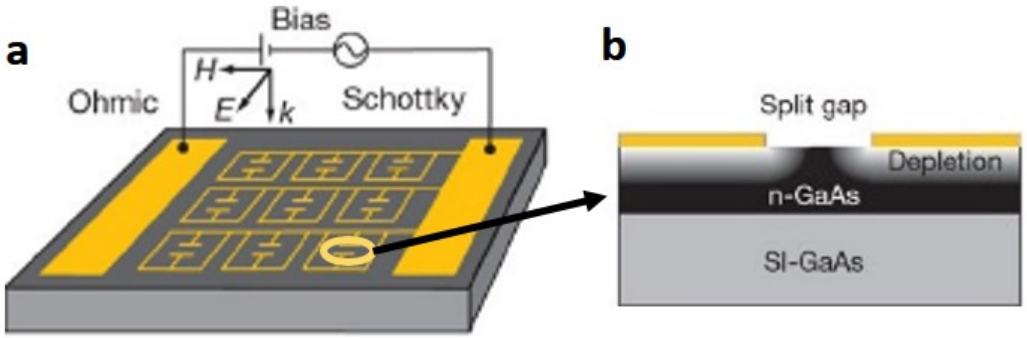

Figure 1-8: Electrically controlled THz MM modulator [84]. (a) A voltage bias applied between the Schottky and ohmic contacts controls the substrate charge carrier density near the split gaps, tuning the strength of the resonance. Orientation of the incident THz wave is indicated and the polarization of the electric field, E, magnetic field, H, and wave vector, k, are shown. (b) Diagram of the substrate and the depletion region near the split gap, where the grey scale indicates the free charge carrier density.

Although great progress in optically based THz modulators has been achieved, as described above, an all-electronic approach is an attractive proposition, especially with a view toward applications. It also allows for control circuit integration in the metamaterial device for achieving higher modulation speed [101]. Similar to the underlying principle of THz wave modulation by photo-doping of semiconductors, the carrier concentration in semiconductors can be changed by electric injection or depletion of charge carriers. Chen *et al.* first reported such a device [84]. A thin n-type GaAs layer was used to inject carrier into the split gap by applying a bias voltage across the metal layer and the n-type Gas layer, as shown in Fig.1-8. Similar principle of shunting the split gap capacitance by optically pumping the substrate has also been previous reported [83, 86]. One of the limitations of such technique is slow modulation speed since an entire substrate is being modulated by a pulsed voltage source with a large intrinsic capacitor. A similar structure was fabricated in which a hole array functioned as the GaAs epilayer [131], with 2% change in transmission peak frequency. Another work fabricated a similar structure and

demonstrated a maximum transmission modulation depth of 52% [132]. Ring apertures fabricated in silicon were shown to yield transmissive values of 60%, thus suggesting fabrication of THz modulators by CMOS architectures[133]. In the last decade the use if two-dimensional electron gases (2DEGs) in semiconductors has proven useful for control of THz waves and high electron mobility transistor (HEMT) has been a popular way to implement it [134]

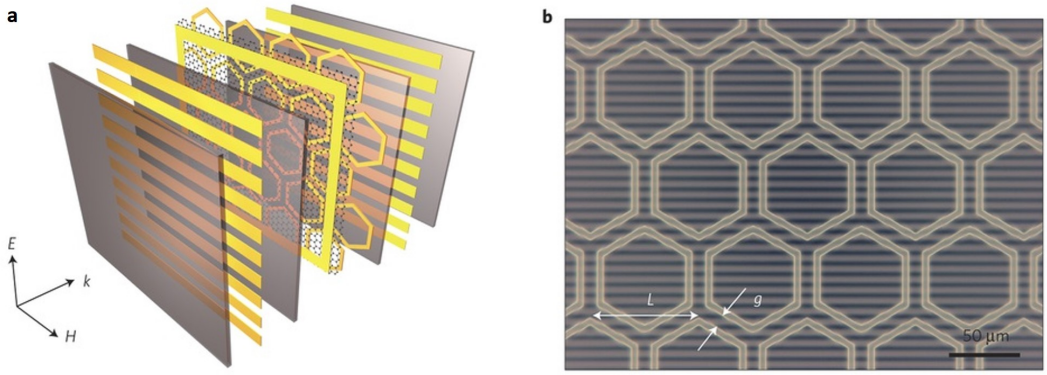

Figure 1-9: Gate-controlled active graphene metamaterial. (a) Schematic rendering of a gate-controlled active graphene metamaterial composed of a SLG deposited on a layer of hexagonal metallic meta-atoms. Metallic patterns and dielectric materials are represented by yellow and grey, respectively. The polarization of the incident terahertz wave is perpendicular to the line electrode, as indicated by the arrows. (b) Optical micrograph of the fabricated gate-controlled active graphene metamaterial without the top electrode. [135].

More recently, it has been found that graphene is superior to semiconductors when used as an electrically driven modulator [136–140], due to its unique band structure which exhibits a linear dispersion relation between energy and crystal momentum. This results in extremely high carrier mobilities of up to 20000 $cm^2V^{-1}s^{-1}$ for both holes and electrons. Furthermore, outstandingly high carrier concentrations up to $1 \times 10^{14}cm^{-2}$ can be obtained in graphene as well as extremely low carrier concentration at the Dirac point [140]. Thus, the carrier concentration can be tuned by applying an external electric field to the graphene layer. Sensale-Rodriguez et al. reported an electronically driven graphene terahertz wave modulator based on modification of the conductivity of graphene by controlling intraband transitions in a single graphene layer or

alternately in graphene-semiconductor stacks [140]. The intensity modulation depth was reported to be about 16% in the frequency range from 570 GHz to 630 GHz at 20 kHz modulation speed. Lee et al. demonstrated terahertz wave switching in gate-controlled graphene metamaterials [135]. The graphene metamaterial was composed of single-layer graphene on top of a metamaterial with a hexagonal unit cell deposited on a polyimide substrate as depicted in Fig.1-9. A maximum amplitude modulation depth of 90% was reported at the resonance frequency of 0.68 THz.

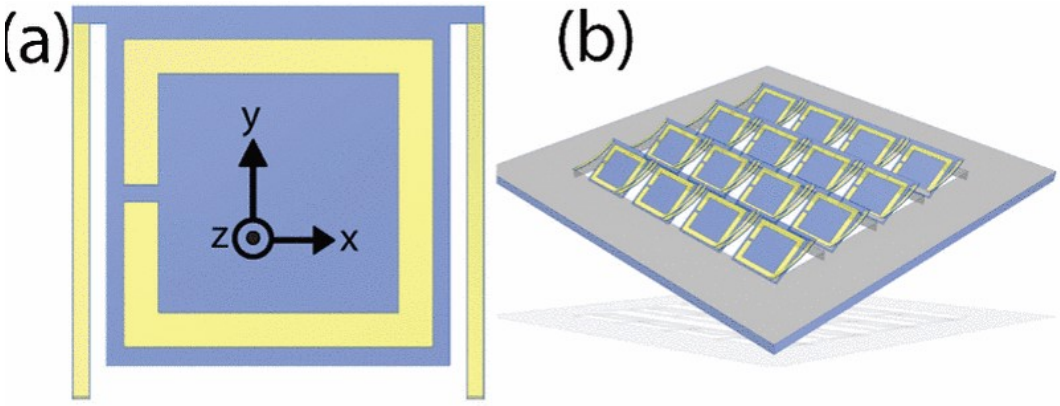

Figure 1-10: Structurally reconfigurable THz MM fabricated on bimaterial cantilevers.(a) Unit cell consisting of a split ring resonator and cantilever legs. (b) Schematic view of a portion of the metamaterial structure highlighting how the SRRs rotate as the cantilever legs bend [90].

One method of THz modulation is to thermally tune the electrical conductivity and thus the optical response of semiconductors or metal oxides [141], special insulator materials with metallic phase transition [89], or superconductors [142]. An example of a thermally tunable metamaterial modulator is shown in Fig.1-10 [90]. As a major disadvantage, thermal modulation is comparably slow with time constants in the range of several tens of milliseconds or longer.

Since most terahertz detectors today measure the incident power or the intensity of the THz wave, the terahertz modulators described so far are intensity modulators of the incident THz wave, either in transmission or reflection geometry. But there is an important subset of THz imaging which

benefits from phase-sensitive spectroscopic images for material identification. With progress in terahertz time-domain spectroscopy, quantum-cascade lasers and continuous-wave terahertz spectrometers, phase information can now be extracted easily, even in compact THz systems making terahertz phase modulators a desirable THz component. Given the difficulty in building terahertz phase modulators, recent demonstration of a metamaterial solid-state terahertz phase modulator [88], is promising for building linearly controllable terahertz phase shifters.

Few more methods for designing terahertz wave modulators are compiled in a very comprehensive review by Rahm *et al.* in [143]. The results of all the methods are summarized very succinctly which is reproduced in Table.1.1. And as seen from the summary, this work (in bold, Ref. [101]) still stands as the fastest electrically controlled THz solid-state modulator.

1.4 Organization of this Thesis

This research has focused on the analysis, design and applications of terahertz metamaterial devices in commercial semiconductor foundry process. In chapter 2, we elaborate the fundamentals of metamaterials from Maxwell's equation and from a Drude-Lorentz type expression of electrically-coupled LC (ELC) resonators, we analytically show the principle for designing a modulator using metamaterials.

In chapter 3, we show the fabrication and experimental verification of high-speed terahertz modulator using commercial GaAs process. The design process is detailed in this chapter with the basic theory of terahertz metamaterial modulator using a pHEMT embedded in each metamaterial unit cell. The characterization of the device using terahertz time-domain spectroscopy (THz-TDS) is also detailed in this chapter.

Chapter 4 shows design, implementation and characterization of a terahertz spatial light modulator (SLM) resonant at 0.45 THz. We demonstrate a single-

Method	**Material**	τ/f_{Mod}	Frequency	M_{A2}	Ref.
Optical	Silicon	28 ms	2.5 THz	-	[144]
Optical	Silicon	430 ns	2.5 THz	-	[127]
Optical	GaAs	10 ns	1.4 THz	-	[145]
Optical	Silicon	5 ns	1.4 THz	-	[128]
Optical	InSb (grating)	ps	-	0.25%,1%	[146]
Optical	Meta/GaAs	-	0.56 THz	80%	[83]
Optical	Meta/ErAs/GaAs	20 ps	0.75 THz	35%	[86]
Optical	Meta/SOS	-	0.6 THz	70%	[147]
Electrical	GaAs/AlGaAs(2DEG)	-	0.1-2 THz	3%	[134]
Electrical	Meta/nGaAs	-	0.72 THz	30%	[84]
Electrical	GaAs (hole array)	-	-	33%	[132]
Electrical	Meta/nGaAs	100 kHz	0.63 THz	36%	[148]
Electrical	Meta/nGaAs	2 MHz	-	-	[87]
Electrical	**Meta/HEMT**	**10 MHz**	**0.46 THz**	**33%**	[101]
Electrical	Graphene	-	0.57-0.63 THz	9%	[140]
Electrical	Meta/Graphene	-	0.68 THz	59%	[135]
Thermal	Meta/VO2	-	1.0 THz	70%	[149]
Thermal	Meta/YBCO	-	0.61-0.55 THz	90%	[142]

Table 1.1: The table summarizes some characteristic quantities of optically, electrically and thermally driven terahertz wave modulators for various material systems. The modulators are evaluated with respect to the modulation bandwidth f_{Mod} and the relaxation time τ as well as the operating frequency f. Furthermore, approximate values of the modulation depth are estimated. The modulation depth was defined by $M_{A2} = (E_{max} - E_{min})/E_{max}$, where E_{max} is the maximal transmitted electric field amplitude and E_{min} is the minimal transmitted field amplitude. The last column refers to the reference number as listed in the reference section [143].

pixel imaging set up using a continuous-wave terahertz spectrometer. Using the spectrometer and the 2x2 SLM, we present the result of raster scanning a metal object occluded behind a polystyrene screen.

Using the SLM characterization result from chapter 4, we computationally demonstrate in chapter 5, a multi-level amplitude shift keying (ASK) terahertz wireless communication system. We show through analysis and Monte Carlo simulation the noise figure improvement of a multi-level spatial modulation scheme compared to a standard voltage modulation technique.

In chapter 6, we present a novel modulation technique using an array of THz spatial light modulators that modulates the THz wave pictorially. In this chapter we computationally show improvement in bandwidth which is almost linear with number of spatial modulator tiles, compared to standard spatial modulation using single-pixel detector. We also show results of noise performance using Monte Carlo simulation.

Our final contribution is documented in chapter 7, where we show through electromagnetic and circuit simulation an implementation of a terahertz (230-325 GHz) focal plane array (FPA) detector designed using a 0.18 μm CMOS foundry process.

And finally, we conclude with the main contributions from our research work with notes on future direction related to this work.

Chapter 2

Background Theory

2.1 Plane Waves in a Nonconducting Medium

In the absence of sources, the Maxwell equations in an infinite, nonconducting medium described by spatially constant permeability and permittivity are [150]

$$\begin{aligned} \nabla \cdot \mathbf{B} &= 0, & \nabla \times \mathbf{E} + \frac{\partial \mathbf{B}}{\partial t} &= 0 \\ \nabla \cdot \mathbf{D} &= 0, & \nabla \times \mathbf{H} - \frac{\partial \mathbf{D}}{\partial t} &= 0 \end{aligned} \tag{2.1}$$

For sinusoidal solutions ($e^{-i\omega t}$), the equations for the $\mathbf{E}(\omega, \mathbf{x})$,etc.

$$\begin{aligned} \nabla \cdot \mathbf{B} &= 0, & \nabla \times \mathbf{E} - i\omega \mathbf{B} &= 0 \\ \nabla \cdot \mathbf{D} &= 0, & \nabla \times \mathbf{H} + i\omega \mathbf{D} &= 0 \end{aligned} \tag{2.2}$$

For uniform isotropic linear media, $\mathbf{D} = \epsilon \mathbf{E}, \mathbf{B} = \mu \mathbf{H}$ where ϵ and μ in general maybe complex functions of ω. For real and positive ϵ and μ (no losses), $\mathbf{D}$ and $\mathbf{B}$ can be substituted in equation (2.2) to get the Helmholtz wave equation (See Appendix A.1)

$$(\nabla^2 + \mu\epsilon\omega^2) \begin{Bmatrix} \mathbf{E} \\ \mathbf{B} \end{Bmatrix} = 0 \tag{2.3}$$

A plane wave solution, traveling in the x direction, that satisfies both the Maxwell's equation (2.2) and the Helmholtz's equation (2.3) can be shown to be

$$\begin{aligned} \mathbf{E}(\mathbf{x},t) &= \mathbf{E}_0 e^{i(kx-\omega t)} \\ \mathbf{B}(\mathbf{x},t) &= \mathbf{B}_0 e^{i(kx-\omega t)} \end{aligned} \tag{2.4}$$

where k is the wave number

$$k = \sqrt{\epsilon\mu}\,\omega \tag{2.5}$$

The *phase velocity* of the wave is

$$v = \frac{\omega}{k} = \frac{1}{\sqrt{\epsilon\mu}} = \frac{c}{n} \tag{2.6}$$

The quantity n is called the *index of refraction* that can be expressed as

$$n = \sqrt{\frac{\mu}{\mu_0}\frac{\epsilon}{\epsilon_0}} = \sqrt{\mu_r \epsilon_r} \tag{2.7}$$

The wave impedance Z can be expressed as

$$Z = \frac{E_0}{H_0} = \frac{k}{\omega\epsilon} = \frac{1}{v\epsilon} = \sqrt{\frac{\mu}{\epsilon}} = \zeta Z_0 \quad \zeta = \frac{\mu_r}{\epsilon_r} \tag{2.8}$$

2.1.1 Negative Refractive Index

It can be seen from Helmholtz's Eq. (2.3) that propagating waves exist in materials whether ϵ and μ are both positive or negative. In this equation, ϵ and μ enter as a product, so it would not appear to matter whether both the signs are positive or negative. Conventionally, we always express the refractive index n as $+\sqrt{\mu_r\epsilon_r}$ for positive materials ($\epsilon > 0, \mu > 0$).

But, one needs to be careful in taking the square root for $n = \pm\sqrt{\mu_r\epsilon_r}$, that

is resolved by proper analysis. In real materials, the constitutive parameters (ϵ, μ) are complex quantities and causality requires the imaginary part to be positive since the materials are passive. For a left-handed material (LHM), the constitutive parameters satisfy

$$\begin{aligned} \epsilon_r &= e^{i\phi_\epsilon}, & \phi_\epsilon &\in (\pi/2, \pi] \\ \mu_r &= e^{i\phi_\mu}, & \phi_\mu &\in (\pi/2, \pi] \end{aligned} \tag{2.9}$$

and now the refractive index can be expressed as

$$n = \sqrt{\epsilon_r \mu_r} = e^{i\phi_\epsilon/2} e^{i\phi_\mu/2} \tag{2.10}$$

and causality requires the imaginary part of the each $\sqrt{\epsilon}$ and $\sqrt{\mu}$ be positive

$$n = (\epsilon_r^{'} + i\epsilon_r^{''})(\mu_r^{'} + i\mu_r^{''}) \tag{2.11}$$

where $\epsilon_r^{'} = \cos(\phi_\epsilon/2)$, $\epsilon_r^{''} = \sin(\phi_\epsilon/2)$, $\mu_r^{'} = \cos(\phi_\mu/2)$ and, $\mu_r^{''} = \sin(\phi_\mu/2)$.

If the real part of each of the complex quantity in equation (2.11) goes to zero, the positive imaginary values result in a real $n < 0$. Therefore,

$$n = -\sqrt{\epsilon_r \mu_r}, \quad \epsilon_r < 0, \mu_r < 0 \tag{2.12}$$

A detailed derivation of it can be found in [151, 152].

2.1.2 Propagation of Waves in Left-Handed Material

For plane monochromatic wave proportional to $\exp(ikx - i\omega t)$, the Eq. (2.1) along with $\mathbf{D} = \epsilon\mathbf{E}, \mathbf{B} = \mu\mathbf{H}$ reduce to [57] (See Appendix A.2)

$$\begin{aligned} \mathbf{k} \times \mathbf{E} &= \omega\mu\mathbf{H} \\ \mathbf{k} \times \mathbf{H} &= -\omega\epsilon\mathbf{E} \end{aligned} \tag{2.13}$$

It can be see from these equations that for materials with $\epsilon > 0$ and $\mu > 0$ they form a right-handed triplet vectors and so the term *Right-Handed Materials* (RHM), and for materials with $\epsilon < 0$ and $\mu < 0$ they form a left-handed triplet vectors and so the term *Left-Handed Materials* (LHM).

This should not be confused with the left-handed chiral optical materials which are completely different. This has prompted authors to call these *backward wave media* [153], *negative phase velocity media* [152], *double negative media* [151] or *negative refractive index materials* [67].

The energy flux carried by the wave is determined by the Poynting vector **S**, given by

$$\mathbf{S} = \mathbf{E} \times \mathbf{H} \tag{2.14}$$

and the direction of the vector is given by the right-hand rule which is the same for right-handed materials. Since Poynting's Theorem is derived by considering conservation of energy [150], we can think of a matched interface of a right-handed material with a left-handed material and the energy flow has to be in the same direction. Therefore, according to Eq. (2.14) the vector **S** is in parallel with the wave vector **k** for right-handed materials and is anti-parallel for left-handed materials.

2.1.3 Propagation of Waves in Single Negative Medium

A single negative medium has either $\epsilon < 0$ or $\mu < 0$. For this analysis, we will assume $\epsilon < 0$ and $\mu = \mu_0$. The wave number k can be expressed as

$$k = \omega\sqrt{\mu_0|\epsilon_r|}e^{i\phi_e/2} = k^{'} + ik^{''} \tag{2.15}$$

By substituting k (2.15) in a plane wave ($\mathbf{E}(x,t) = \mathbf{E}_0 e^{i(kx-\omega t)}$), it can be expanded to

$$\mathbf{E}(x,t) = e^{-k^{''}x}\mathbf{E}_0 e^{i(k^{'}x-\omega t)} \tag{2.16}$$

The analysis for $\mu < 0, \epsilon > 0$ is similar. Therefore, the propagating wave in a single negative media is a decaying wave front.

2.2 Dispersion in Nonconductors

In the previous section, it has been shown that the propagation of EM waves in nonconducting media is governed by two properties of the material, which was assumed to be constant: the permittivity ϵ, and the permeability μ. It is well known from optics that the *refractive index* ($n = c\sqrt{\epsilon\mu}$) is a function of ω. Thus a prism bends blue light more sharply that red, spreading white light into a rainbow of colors. This phenomena is called *dispersion* and whenever the speed of a wave varies with frequency, the supportive medium is called *dispersive*. Although both ϵ and μ are function of ω, in practice, μ is very close to μ_0, for most natural materials, and it's variation with ω is insignificant [154]

2.2.1 Lorentz Oscillator Model for Permitivity

The classical theory of the absorption and dispersion for nonconductors (insulators) is due mainly to Lorentz. The Drude model is applicable to free-electron metals. Although these models were based on classical *ad hoc* formulation, they have its quantum mechanical analogs are strikingly similar and to date, the Drude-Lorentz models are still very useful for developing a feel for optical properties of solids.

The Lorentz model considers an atom with electrons bound to the nucleus using a model described by a small mass tied to a large mass by spring. The motion of an electron is then described by

$$m\left[\ddot{\mathbf{x}} + \gamma\dot{\mathbf{x}} + \omega_0^2\mathbf{x}\right] = -e\mathbf{E}(\mathbf{x}, t) \tag{2.17}$$

where $m\gamma\dot{\mathbf{x}}$ is the damping force representing the energy loss mechanism which

arises due to radiation from an atom due to different scattering mechanisms. The term $m\omega_0^2\mathbf{x}$ is the Hooke's law restoring force in the *electron oscillator* model. In the context of a classical model, there are two main assumptions in Eq.(2.17). The nucleus has been assumed to have infinite mass and the small magnetic force $-e\mathbf{v}\times\mathbf{B}/c$ on the electron due to the magnetic component has been neglected.

For a sinusoid electric field with frequency ω as $e^{-i\omega t}$, the displacement vector $\mathbf{x}$ is the solution of Eq. (2.17) and the dipole moment $\mathbf{p}$ contributed by each electron is [150]

$$\mathbf{p} = -e\mathbf{x} = \left[\left(\frac{e^2}{m_e}\right)\frac{1}{(\omega_0^2-\omega^2)-i\omega\gamma}\right]\mathbf{E} = \xi(\omega)\mathbf{E} \tag{2.18}$$

where $\xi(\omega)$ is the frequency-dependent atomic polarizability, Assuming a linear relationship between $\mathbf{p}$ and $\mathbf{E}$ due to small displacements. $\xi(\omega)$ is a complex quantity because of the damping term in the oscillator model.

For N atoms per unit volume, the macroscopic polarization is [155]

$$\mathbf{P} = N\langle\mathbf{p}\rangle = N\xi(\omega)\langle\mathbf{E}\rangle = \epsilon_0\chi(\omega)\mathbf{E} \tag{2.19}$$

where $\chi(\omega) = N\xi(\omega)/\epsilon_0$ is the frequency-dependent complex susceptibility that is defined in relation to the constitutive parameters as

$$\mathbf{D} = \epsilon_0(1+\chi(\omega))\mathbf{E} = \epsilon_0\epsilon_r(\omega)\mathbf{E} \tag{2.20}$$

Using Eq.(2.18-2.20, the relative permitivity $\epsilon_r(\omega)$ is

$$\epsilon_r(\omega) = 1 + \frac{\omega_p^2}{(\omega_0^2-\omega^2)-i\omega\gamma}, \qquad \omega_p^2 = \frac{Ne^2}{m_e\epsilon_0} \tag{2.21}$$

where ω_p is the plasma frequency of the insulator which is the oscillating frequency in Drude model where the restoring force term $m_e\omega\gamma$ is zero. In other words, the Drude model for metals is obtained directly from the Lorentz

model for insulators simply by equating the restoring force to zero.

2.2.2 Anomalous Dispersion and Resonant Absorption

From the complex permitivity expression in Eq. 2.21, the real and imaginary part of $\epsilon_r = \epsilon_r^{'} + i\epsilon_r^{''}$ can be written as

$$\begin{aligned} \epsilon_r^{'}(\omega) &= 1 + \omega_p^2 \frac{\omega_0^2 - \omega^2}{(\omega_0^2 - \omega^2)^2 + \omega^2\gamma^2} \\ \epsilon_r^{''}(\omega) &= \omega_p^2 \frac{\omega\gamma}{(\omega_0^2 - \omega^2)^2 + \omega^2\gamma^2} \end{aligned} \tag{2.22}$$

where $\epsilon_r^{'} = \texttt{Re}[\epsilon_r]$ and $\epsilon_r^{''} = \texttt{Im}[\epsilon_r]$. The imaginary part is directly associated with the absorption of the incident wave and also when the real part is negative. The frequency dependence of $\epsilon_r^{'}$ and $\epsilon_r^{''}$ are plotted in Fig. 2-1. Except

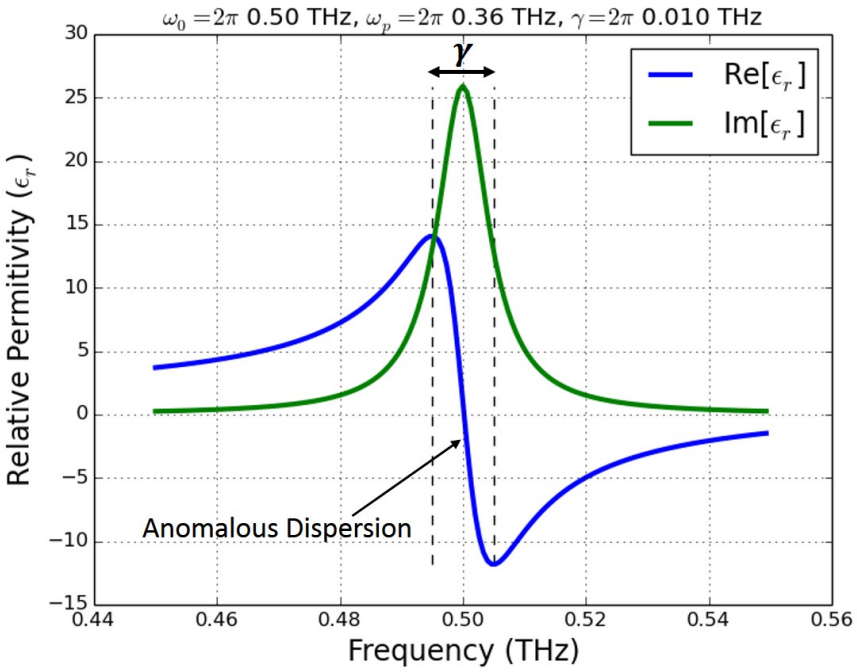

Figure 2-1: Anomalous Dispersion – Real and imaginary parts of the dielectric constant $\epsilon(\omega)/\epsilon_0$ in the immediate neighborhood of a resonance. The region of anomalous dispersion is also the frequency interval for the maximum absorption.

for a narrow region around the resonance, $\epsilon_r^{'}$ increases with frequency called the normal dispersion. In the narrow region of the resonance it decreases with

frequency called *anomalous dispersion*. This region is also the frequency interval of maximum absorption as will be shown later in this section. The width of this region is equal to the loss factor γ.

With ϵ now a complex function of ω, the dispersive medium admits x-polarized plane-wave solutions, as before,

$$\mathbf{E}(x,t) = \mathbf{E}_0 e^{i(kx-\omega t)} \tag{2.23}$$

However, the wave number $k = \omega\sqrt{\epsilon\mu}$ is complex, because ϵ is. Writing k in terms of real and imaginary parts of the refractive index

$$k = \beta + i\frac{\alpha}{2} \tag{2.24}$$

equation (2.23) becomes

$$\mathbf{E}(x,t) = \mathbf{E}_0 e^{-\alpha x/2} e^{i(\beta x-\omega t)} \tag{2.25}$$

Evidently, $\alpha/2$ measures the *attenuation* of the wave. Because the *intensity* is proportional to E^2, it falls off as $e^{-\alpha x}$, α is called the *absorption coefficient*. For non-magnetic material ($\mu = \mu_0$), the complex frequency-dependent refractive index n can be expressed as

$$n = n_R + in_I = \sqrt{\epsilon_r^{'} + i\epsilon_r^{''}} \tag{2.26}$$

where the n_R and n_I are the real and imaginary part of complex n known as the *ordinary refractive index* and *extinction coefficient* respectively.

Squaring and equating both sides of Eq. (2.26) we get

$$\epsilon_r^{'} = n_R^2 - n_I^2, \qquad \epsilon_r^{''} = 2n_R n_I \tag{2.27}$$

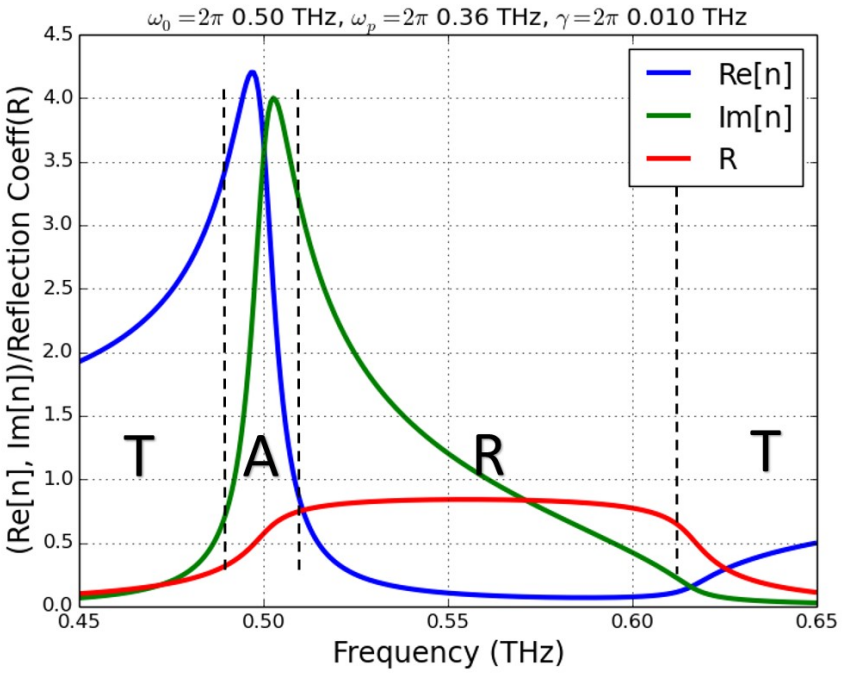

Figure 2-2: Plots of the real and imaginary part of the refractive index (Eq.2.28) and the reflection coefficient (Eq.2.31) for an example material with $\omega_0 = 2\pi 0.5$ THz, $\omega_p = 2\pi 0.36$ THz and $\gamma = 2\pi 0.01$ THz.

From Eq. 2.27, the real and imaginary part of the refractive index are

$$n_R = \left\{ \frac{1}{2} \left[\sqrt{(\epsilon_r^{'})^2 + (\epsilon_r^{''})^2} + \epsilon_r^{'} \right] \right\}^{1/2}$$
$$n_I = \left\{ \frac{1}{2} \left[\sqrt{(\epsilon_r^{'})^2 + (\epsilon_r^{''})^2} - \epsilon_r^{'} \right] \right\}^{1/2} \tag{2.28}$$

Now, the absorption coefficient α can be expressed in terms the refractive index using the relation

$$k = n\omega\sqrt{\epsilon_0\mu_0} = k_0\omega(n_R + in_I), \qquad k_0 = \sqrt{\epsilon_0\mu_0} \tag{2.29}$$

From Eq. 2.29 we can express the absorption coefficient as

$$\alpha = 2k_0\omega n_I \tag{2.30}$$

Typically, for analyzing absorption around the resonance, n_I is sufficient indi-

cator since ω does not change appreciably in that region.

Another optical parameter that provides independent information about the material in the frequency of interest is the reflection coefficient. From Eq. 2.28, the reflection coefficient at normal incidence is given by [155]

$$R = \frac{(n_R - 1)^2 + n_I^2}{(n_R + 1)^2 + n_I^2} \tag{2.31}$$

The plots for the real/imaginary part of the refractive index (Eq.2.28) and the reflection coefficient (Eq.2.31) is shown in Fig.2-2. From the plots, we can see the implications of the frequency dependence of $\epsilon_r^{'}$ and $\epsilon_r^{''}$. The plots show 4 distinct regions, transmission, absorption, reflection and transmission again. Before the onset of the resonance, the material behave as a positive refractive index transmissive material. Then, for roughly the band around resonance $(\omega_0 \pm \gamma/2)$, the material behaves as an absorber, reflective after that and for frequencies much higher than the plasma frequency, its transmissive again.

These plots give a insight on the considerations for building a metamaterial based modulator. By dynamically controlling the absorption peak, one can modulate an EM wave passing through the metamaterial around the resonance frequency.

2.3 Metamaterial as a Modulator

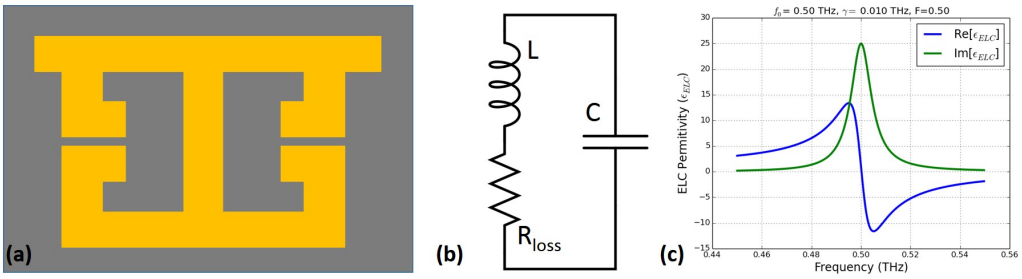

Figure 2-3: (a) A typical ELC element used in most electric metamaterial (MM) design. (b) An equivalent circuit of the MM unit cell (c) Average permittivity (real and imaginary) of the MM (Eq. 2.32) for an example design with $f_0 = 0.5$ THz, $\gamma = 0.01$ THz and F=0.5

The electrically-coupled LC resonator (ELC) based metamaterial are suitable for planar design since the incident field can be incident to the normal of the device plane. For the ELC resonator shown in Fig. 2-3(a), the average permittivity, ignoring the spatial dispersion, is of the Lorentz-like form [91, 116, 156]

$$\epsilon_{ELC} = \epsilon_a \left[1 - \frac{F f^2}{f^2 - f_0^2 + i\gamma f}\right] \tag{2.32}$$

where, ϵ_a is the permittivity of the background material , $f_0 = 1/\sqrt{LC}$ is the resonant frequency in terms of it's equivalent circuit parameters (Fig. 2-3(b)), γ is associated with the loss (R_{loss} in Fig. 2-3(b)) and F is associated with filing factor of the geometry of the unit cell. The real and imaginary part of the permittivity from Eq. 2.32 is plotted in Fig. 2-3(c) for an example design with $f_0 = 0.5$ THz, $\gamma = 0.01$ THz and F=0.5. The response is similar to the Lorentz oscillator model of non-conductors derived in Eq. 2.21. As

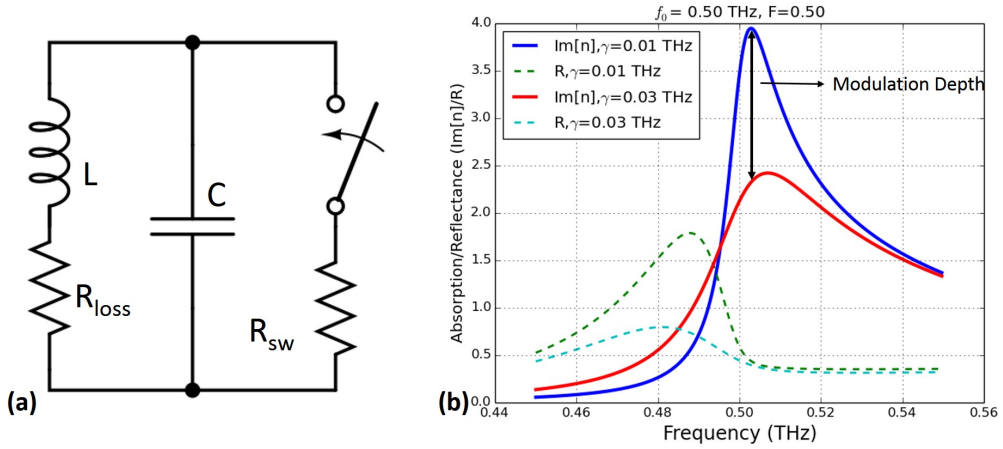

Figure 2-4: (a) A conceptual circuit equivalent of a metamaterial based modulator (b) Absorption and reflectance plot an ELC based metamaterial with and without the modulation resistance (R_{sw}).

observed in Fig. 2-2, the absorption of non-conducting materials is maximum in the vicinity of molecular resonance frequency. It follows from that observation that, in order to design a metamaterial based modulator for a desired frequency, the resonance frequency of the metamaterial should be designed for that desired frequency and a dynamic method should be devised to either

shift the resonance frequency or weaken the resonance by adding loss to the resonator.

One such method is shown conceptually in Fig. 2-4(a) where a resistive element is used to shunt the MM capacitance of the split gap to weaken the resonance. Assuming the shunt resistor changes the dissipation factor γ from 0.01 THz to 0.05 THz, the imaginary part of the complex refractive index (n in Eq. 2.28), which corresponds to the absorption coefficient, is plotted in Fig. 2-4(b). It can be seen from the plot that the absorption around the resonance frequency ($f_0 = 0.5$ THz) drops by approximately 40%. The reflectance plot shows little change around the modulation frequency. Terahertz modulators have been demonstrated based on this principle of shunting the split gap capacitance by optically pumping the substrate [83, 86] or electrically injecting carriers [84], a schematic of the basic structure shown in Fig. 1-8. This is the fundamental principle behind the metamaterial based terahertz modulator design in this work that is covered in depth in the next chapter.

Metamaterial based terahertz modulators have also been demonstrated by dynamically controlling the capacitance or the inductance of the split gap capacitance. A dynamic terahertz metamaterial was realized by dynamically controlling the capacitance of the split gap by optically pumping the substrate and experimentally demonstrated by Chen et.al. [85], a schematic of the structure shown in Fig. 1-7. The same work [85] also computationally demonstrated a dynamic terahertz metamaterial by controlling the inductance of the metamaterial unit cell as shown in Fig. 2-5.

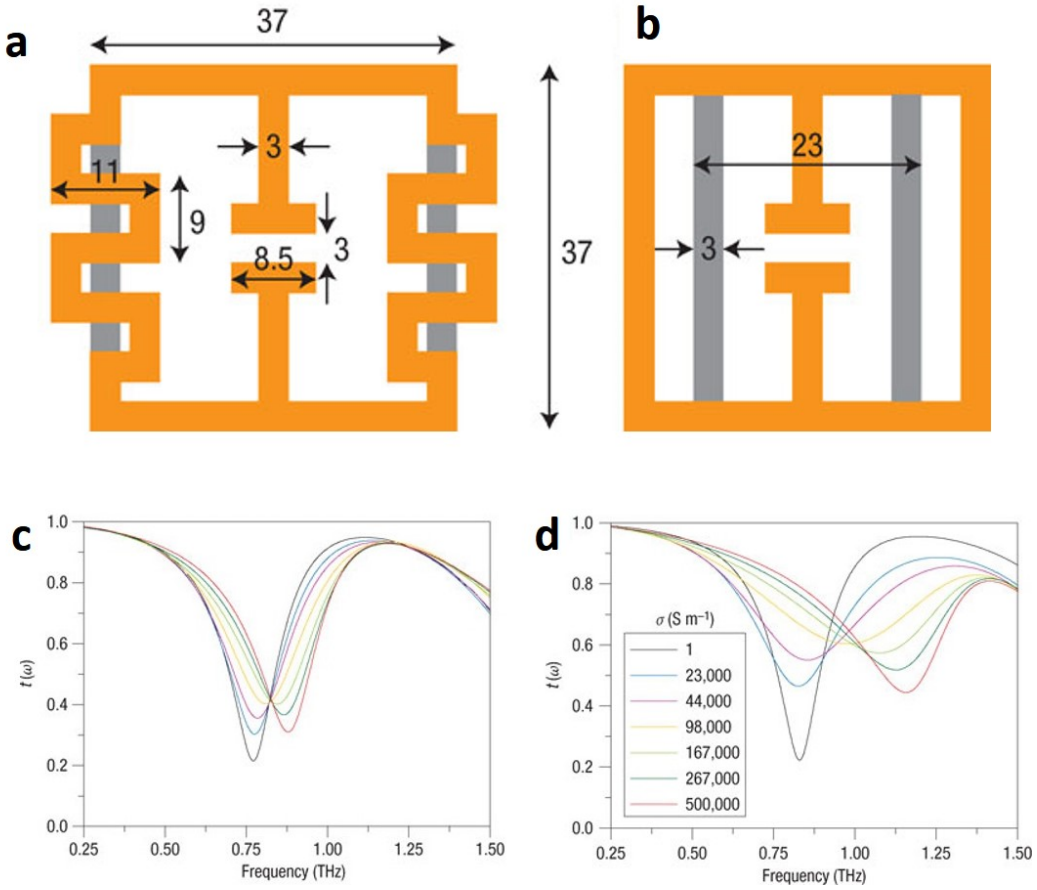

Figure 2-5: An inductance tune dynamic terahertz metamaterial [85]. (a,b) The photoexcited silicon regions form parallel current paths through the meandering loop sections (a) and across the regular loop sections (b) to effectively modify the inductance of the SRRs. The metal and silicon regions are displayed in orange and grey, respectively. The dimensions are shown in micrometres. (c,d) Simulations of the structure of (a) and the structure of (b), both using the silicon conductivity values shown in the key

Chapter 3

High Speed Terahertz Modulation from Metamaterials with embedded High Electron Mobility Transistors

Electronically controlled high speed terahertz (THz) modulation is highly desirable due to its vast potential of creating low cost consumer grade devices for applications ranging from communication to imaging. The last decade has seen significant research in creating terahertz wave modulators but there is still work left to make the devices affordable for daily consumer applications.

Various methods have been utilized to achieve amplitude and frequency modulation including photodoping [85], electronic [84] and temperature control [89]. By implementing schottky diodes other research has achieved both spatial [87, 148] and phase modulation [88]. These metamaterial devices rely on layers of n-doped gallium arsenide (GaAs) and initial studies have demonstrated the potential of these systems for high speed telecommunications [157], spectroscopy [88], and imaging [158]. To-date THz metamaterials have shown modulation at frequencies low in the MHz range, and higher speed modulation

has been hindered by large device capacitance [87].

The motivation to create high speed modulators has pushed researchers to use two-dimensional electron gases (2DEGs) in high electron mobility transistors (HEMTs) to manipulate THz waves [134]. Although HEMT devices have demonstrated advantages over alternative architecture, such as quantum well structures and liquid crystals [159], they have been limited to relatively low transmission modulation values of less than 3%, and maximum modulation frequencies of 10 kHz [160]. One of the key to high speed terahertz devices is the hybridization of semiconductor technology and metamaterials, an area of research still in its infancy.

We present in this work the monolithic integration of standard pseudomorphic HEMTs (pHEMTs), at the unit cell level, in a terahertz metamaterial using a commercial grade galium arsenide (GaAs) process. Using this device we demonstrate for the first time, modulation of terahertz frequencies (0.45 THz) up to speeds of 10 MHz [101], which can fundamentally be designed for much higher speeds.

3.1 Design principle of the HEMT controlled metamaterial modulator

The basic principle of our THz SLM is based on a electronically controlled absorption coefficient in a metamaterial using embedded pHEMT devices as described below. For a metamaterial designed with electric-LC (ELC) resonators[113, 114] shown in Fig.3-1(a), the average permittivity, without factoring spatial dispersion, can be expressed in a Drude-Lorentz form[91, 116]

$$\bar{\epsilon}(f) = \epsilon_a \left[1 - \frac{F f^2}{f^2 - f_0^2 + i\gamma f}\right] \tag{3.1}$$

where, ϵ_a is the permittivity of the background material (silicon nitride), $f_0 = 1/2\pi\sqrt{L_{MM}C_{MM}}$ is the resonant frequency in terms of it's equivalent circuit

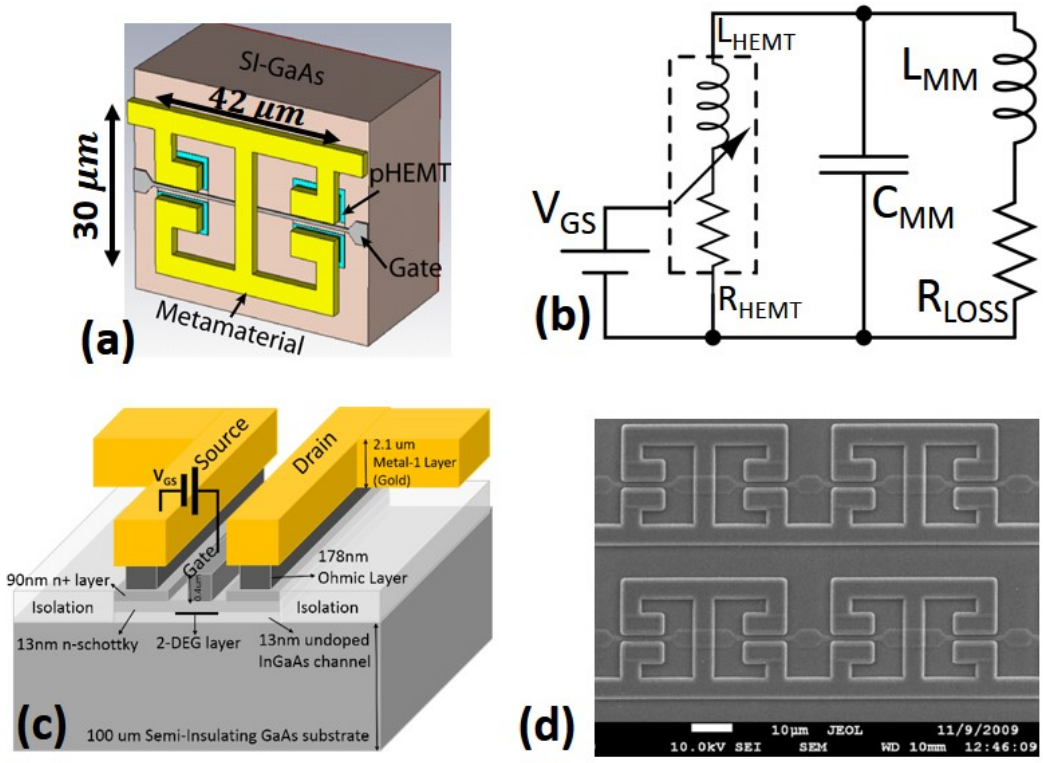

Figure 3-1: Design and fabrication details. (a) Each metamaterial element is based on the electric-LC (ELC) resonator, patterned using the top 2.1μm thick gold metal. A pseudomorphic high-electron mobility transistor (pHEMT) is placed underneath each split gap with their source and drain connected to each side of the split gap. The gate-to-source/drain (V_{GS}) controls the channel charge (2-DEG) between the split gap, thus electronically controlling the resonance. (b) An equivalent circuit of the HEMT-embedded metamaterial element, where the resistor-inductor (inside the dashed box) represents the Drude model of the HEMT switch at the operating frequency of 0.45 THz when $V_{GS} = 0V$. When the 2-DEG channel is depleted ($V_{GS} = -1V$) then L_{HEMT} and R_{HEMT} are removed from the equivalent circuit. (c) Close-up diagram of the split-gap shows the placement of the HEMT device with it's drain and source connected to both ends of the split gap. (d) SEM picture of MM/HEMT elements.

parameters [Fig. 3-1(b)], γ is associated with the loss [R_{LOSS} in Fig. 3-1(b)] and F is associated with filing factor of the geometry of the unit cell. The ELC resonator is equivalent to two split-ring resonators (SRRs) put together with a fundamental mode that couples strongly to a uniform electric field linearly polarized perpendicular to the split gap, and negligibly to a uniform magnetic field making it suitable for applications with incident THz wave normal the the planar structure. Therefore, the ELC usually does not exhibit a strongly dispersive permeability ($\bar{\mu}(f) \approx \mu_a$). Since the dispersion relation is complex, $\bar{\epsilon}(f) = \epsilon^{'}(f) + i\epsilon^{''}(f)$, the wave number $k = \omega\sqrt{\bar{\epsilon}(f)\mu_0}$ is also a complex number that is written as $\kappa = \beta + i\alpha/2$ [Eq.2.24] where, α is the attenuation constant or the absorption coefficient. The absorption coefficient is expressed in terms of the imaginary part of the refractive index n_I was shown in Eq.2.30. The attenuation of the incident THz electric field is directly related to the absorption coefficient α, which is maximum at the resonant frequency f_0 known as the *anomalous dispersion* [See Sec.2.2.2].

In section (2.3) we showed in principle, the method to achieve modulation using a dynamic metamaterial (MM). In this work, we use a pseudomorphic high electron mobility transistor (pHEMT) to shunt the split-gap capacitor of each ELC element [101](Fig-3-1(c)), which increases the loss of the resonator (higher γ) resulting in a lower absorption at the resonant frequency. Thus by electrically controlling the 2-D electron "gas" (2DEG) density across the split gap, we are able to modulate a terahertz (THz) wave using voltage control.

The pHEMT is a standard device offered in the process, that is constructed using pseudomorphic undoped InGaAs and a lightly doped schottky layer, 12.7 nm and 22.5 nm thick respectively, creating a heterojunction. An equivalent heterojunction is shown in Fig.3-2(a) from [161][1]. A very high-mobility 2DEG ($\sim$ 3000 cm$^2/V \cdot s$) is formed at room temperature in the *undoped* In-GaAs channel layer as predicted by the band diagram at the interface[161], enabling

[1]Due to reasons of confidentiality with the manufacturing vendor, the proprietary heterostructure could not be published.

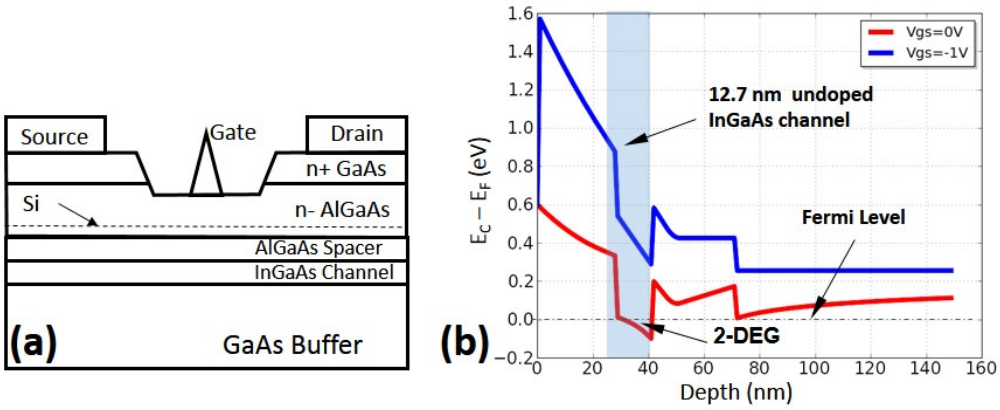

Figure 3-2: pHEMT heterostructure and energy band diagram. (a) Cross-section of a gate-length planar pHEMT from [161] which similar to the structure used in this work.(b) Computed energy-band diagram of the planar doped AlGaAs/InGaAs/AlGaAs quantum well heterostructure of the pHEMT that is used in this work. The band diagram is computed for V_{GS} of 0V and -1V. The conduction band discontinuity can be seen in the undoped InGaAs channel. For $V_{GS} = 0V$ the conduction band falls below the fermi level resulting in a high-mobility ($\sim 3000\ cm^2/V \cdot s$) channel with a computed charge density of $N_S = 7.37 \times 10^{12} cm^{-2}$.

fast conduction even at THz frequencies. The gate voltage with respect to the source (or drain), V_{GS}, controls the charge density in the 2-DEG layer between the split-gap. Using the basic layer information provided by the manufacturer, a 1-D Poisson solver [162] was used to compute the band diagrams for $V_{GS} = 0V$ and $V_{GS} = -1V$ and the results are shown in Fig.3-2(b). The conduction band discontinuity can be seen in the undoped InGaAs channel which is responsible for creating a high-mobility channel for fast conduction. For $V_{GS} = -1V$, the charge carriers in the 2-DEG is completely depleted or the *metamaterial is "on"*. For $V_{GS} = 0V$, the conduction band falls below the fermi level [Fig.3-2(b)] resulting in a high-mobility ($\sim 3000\ cm^2/V \cdot s$) channel with a computed charge density of $N_S = 7.37 \times 10^{12} cm^{-2}$ or the *metamaterial is "off"*.

When $V_{GS} = 0V$, the 2-DEG channel can be described by the Drude conductivity[163, 164]

$$\sigma_{2D}(\omega) = \frac{\sigma_0}{1 + i\omega\tau} \tag{3.2}$$

where σ_0 is the DC conductivity [Siemens/sq] given by the expression $\sigma_0 = e^2 N_S \tau / m^*$. Here, e is the electron charge, N_S is the two-dimensional carrier density of the 2-DEG, τ is the scattering or relaxation time, m^* is the effective electron mass and ω the angular frequency of the incident time-varying field. The equivalent circuit for the 2-DEG can be represented as a series R-L structure [164] shown in Fig.3-1(b) where

$$R_{HEMT} = \frac{1}{\sigma_0}, \qquad L_{HEMT} = \frac{\tau}{\sigma_0} \tag{3.3}$$

Since the R-L impedance is parallel to the split gap capacitor (C_{MM}), the new resonant frequency of the metamaterial can be written as

$$f_0' = \frac{1}{2\pi \left[C_{MM} \cdot L_{MM} || L_{HEMT}(1 + 1/Q_{2D}^2)\right]^{1/2}} \tag{3.4}$$

where Q_{2D} is the quality factor of L_{HEMT} due to it's loss R_{HEMT}. The total loss of the ELC is now dominated by R_{HEMT} since $R_{MM} \ll R_{HEMT}$. The relation between $\alpha(f = f_0)$ for $V_{GS} = 0V$ $[\alpha_{0V}(f_0)]$ and $\alpha(f = f_0)$ for $V_{GS} = -1V$ $[\alpha_{-1V}(f_0)]$ can be written as $\alpha_{-1V}(f_0) > \alpha_{0V}(f_0)$. In other words, for an incident THz wave with a time varying electric field of frequency f_0, the transmitted electric field strength will be higher for $V_{GS} = 0V$ than when the 2-DEG channel is completely depleted ($V_{GS} = -1V$). However, R_{HEMT} is the dominant factor in our modulator by weakening the resonance. This is the operating principle for the all solid-state electronically controlled THz modulator.

The consequence of this phenomena results in amplitude modulation of a transmissive terahertz wave at the resonant frequency due to the shift in anomalous dispersion behavior at that frequency[84]. Because of the localized pHEMT in the split-gap, the device has also been demonstrated for fast modulation[101]($\sim 10\ MHz$) that is capable of much higher speed with proper design. Compared to other electrically controlled metamaterial[84, 88], where

the whole substrate is used to control the resonance, this device offers element-level control that offers higher switching speed and offers future opportunity of creating more exotic devices. One such exotic device platform is to populate such amplitude modulator in an array to implement a terahertz spatial light modulator (SLM) without any moving parts. A metamaterial based SLM also offers the advantage of creating hyper-spectral imaging by creating arrays with different frequencies[165].

3.2 Design and fabrication

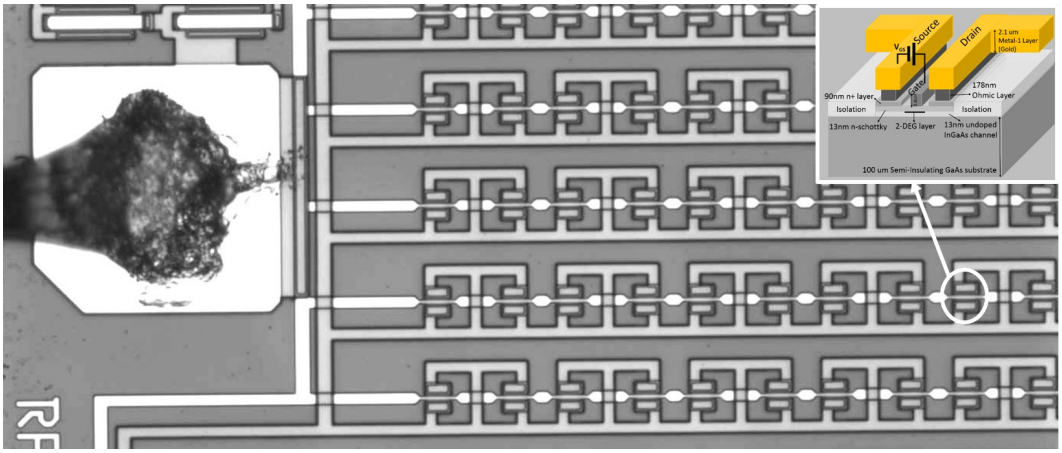

Figure 3-3: A close-up microscope photograph of the metamaterial array near the pad. All the gates of the HEMTs can be seen to be connected together to the pad shown in the picture. Similarly the drain and sources are connected together to another pad (not in the picture). The inset shows a 3-D drawing of the cross-section of one of the split gaps with HEMT connected to the metamaterial split gap.

The sample was constructed using a commercial GaAs technology which consisted of three metal layers, an enhanced mode pseudomorphic HEMT, and a silicon nitride encapsulating dielectric, see Fig. 3-1(a). The technology utilized for this study is primarily used for mobile phone applications and to our knowledge this is the first time this has been used for THz metamaterial applications. The top metal layer, $2.1\mu m$ thick gold, is patterned to form the metamaterial layer. A different metal layer forms the gate of the device and

is also used for connecting all the gates within the same row as shown in Fig. 3-3. A 0.176 μm thick ohmic layer, which is also utilized as a routing layer, was primarily used for connecting the source and drain of the HEMT to the metamaterial. The source and drain are shorted through the metamaterial as a direct consequence of the metamaterial structure we have selected.

The metamaterial geometry used in this work is based on the electric-LC resonator (ELC) [113, 114], and a detail of the unit cell is shown in Fig.3-1(a). Each unit cell consists of two single rings butted together with their split gaps at the outside to accommodate design rules specific to the implemented technology. The line width of the metamaterial is 4μm and the split gap is 3 μm. The metamaterial had the dimensions of 42 μm wide by 30 μm in height. A periodic array of these unit cells as shown in Fig.3-3 was fabricated, with period of 55 μm $\times$ 40μm, and a total size of 2.0 $\times$ 2.6 mm^2 with 2200 elements total. Metamaterial elements are fabricated on a 100μm thick semi-insulating (SI) GaAs substrate.

A pHEMT lies underneath each of the split gaps of the metamaterial element, (two per unit cell), as shown in cross-section in Fig.3-1(c). The gate length is 0.5μm and has a width 5μm for each device. The HEMT is constructed using pseudomorphic undoped In-GaAs and a lightly doped Schottky layer, each 12.7 nm thick, creating a heterojunction. A 2DEG is formed in the undoped In-GaAs channel layer as predicted by the band diagram at the interface (Fig.3-2(b)) [161]. Unlike traditional FETs, this channel is formed in an intrinsic (undoped) crystal, resulting in very high mobility ($\sim$ 3000 cm$^2/V \cdot s$) and charge density (7.37×10^{12}cm^{-2}) at room temperature, thus enabling fast conduction even at THz frequencies.

We simulated the DC behavior of the device using Agilent's Advanced Design System (ADS) software. The dependence of the current between the source and drain terminal (I_{DS}) on the gate bias voltage (V_{GS}), and on the drain to source electric field (E_{DS}) is shown in Fig. 3-4 (a) and (b), respectively.

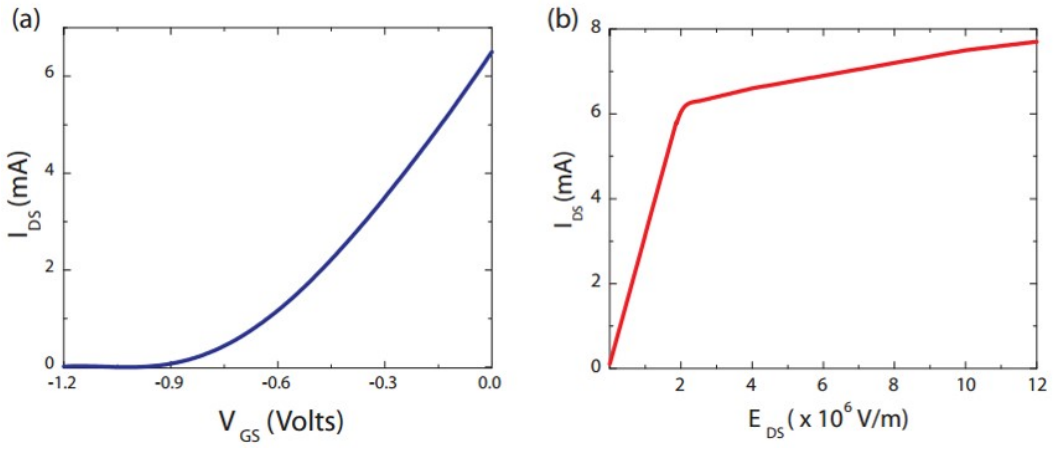

Figure 3-4: The simulated I-V characteristics of the pHEMT (a) Drain-to-source current (I_{DS}) as a function of gate-to-source (V_{GS}) voltage. (b) Drain-to-source current (I_{DS}) as a function of drain-to-source electric field (E_{DS}), operating in the linear region.

The same metal layer which is used to form each metamaterial is also used to connect each element together within the same row as shown in Fig. 3-3. These wires run perpendicular to the split gaps, and we polarize the electric field of incident radiation perpendicular to the connecting wires which avoids the Drude-like response documented in prior works [84]. At the perimeter of the device each row is connected vertically using the ohmic layer and all elements are connected to a single bond pad to provide DC bias voltage for the drain and source of the HEMT. The gates for all HEMTs are connected in a similar fashion to a single bond pad which provides the DC bias voltage for the gate.

The entire unit cell was modeled using a commercial finite difference time domain (FDTD) solver, CST's Microwave Studio, in which the metamaterial was designed to be resonant at 0.46 THz. The physical dimensions of the material layers in the device were modeled as shown in Fig.3-1(c). The gold and ohmic layers were modeled as lossy metals based on their respective DC conductivity values. For both the n+ and Schottky semiconductor layers, we utilize a frequency dependent Drude model for the conductivity. The 2DEG was simulated as a 2nm thick Drude layer, which enables an accurate modeling

of the HEMT device in both the conductive and the depleted (non-conducting) states. This is representative of what occurs in experiment by applying gate to source voltage (V_{GS}) of 0V (conductive) and -1V (depleted). This method allowed us to simulate the THz transmission of the device for various DC biases.

3.3 Experimental Methods

3.3.1 Homogenous Parameter Extraction

Extracting effective parameters ($\epsilon_{eff}, \mu_{eff}$) for metamaterials is a powerful tool to characterize the frequency dependence constitutive parameters.

For a homogeneous and istropic material, the refractive index (n) and the wave impedance (z) can be expressed in terms of its scattering parameters (S_{11}, S_{21}) as [166–168]

$$n = \frac{1}{kd}\cos^{-1}\left[\frac{1}{2S_{21}}\right] \tag{3.5}$$

$$z = \sqrt{\frac{(1+S_{11})^2 - S_{21}^2}{1-S_{11})^2 - S_{21}^2}} \tag{3.6}$$

where the wavenumber of the incident wave os $k = 2\pi/\lambda$ and d is the unit cell dimension. And the relationship between n and z to ϵ_{eff} and μ_{eff} is

$$n = \sqrt{\epsilon_{eff}\mu_{eff}}, \qquad z = \sqrt{\frac{\epsilon_{eff}}{\mu_{eff}}} \tag{3.7}$$

It is difficult from experiments to measure the scattering parameters but, it is easily calculated from simulations and the full material response can be calculated using Eqn. 3.5-3.7.

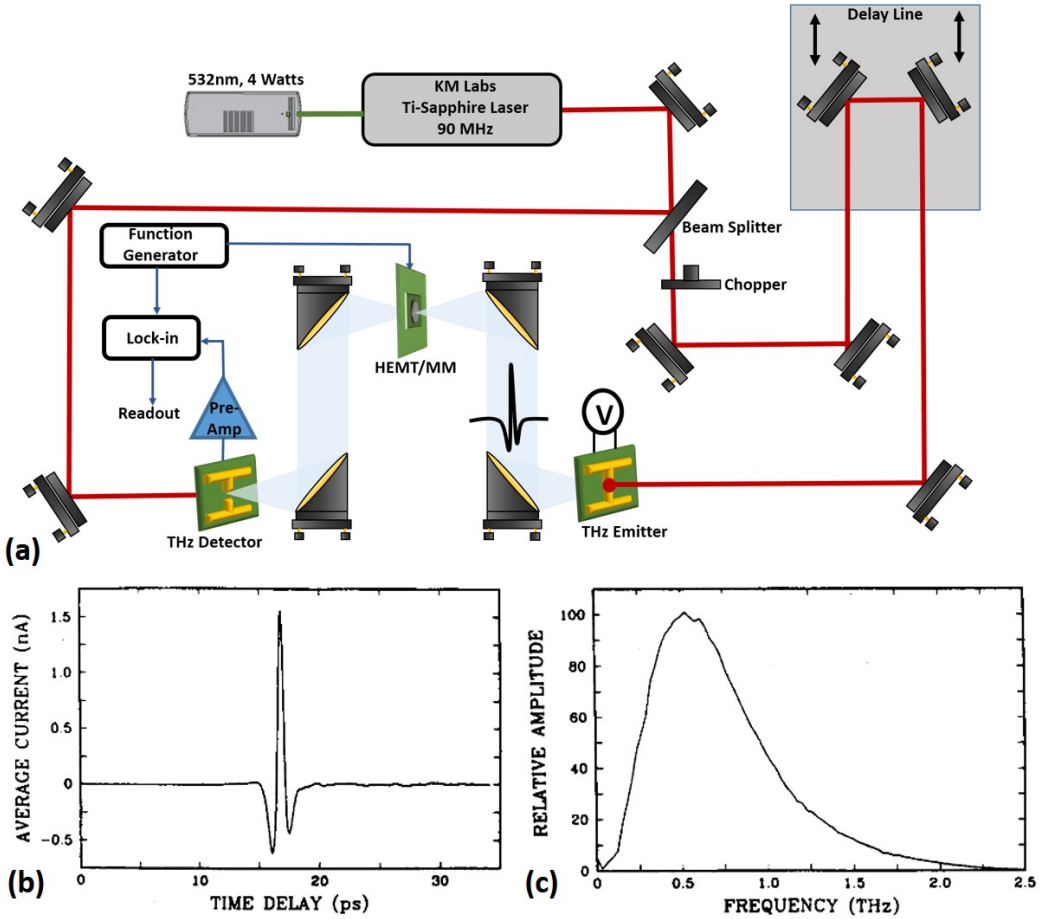

Figure 3-5: (a) Schematic of terahertz time domain spectroscopy (THz-TDS) setup used for demonstration and characterization of high speed modulation of our HEMT embedded metamaterial-based terahertz modulator. (b-c) An example THz-TDS measurement [11]. (b) THz pulse measured by scanning the time delay between the optical gating pulses and the incident THz pulses, while measuring the current in the THz detector. (c) The amplitude spectrum calculated by taking the Fourier transform of the time-domain pulse data shown in (b).

3.3.2 Terahertz Time Domain Spectroscopy

We use a terahertz time domain spectroscopy (THz-TDS), shown in Fig. 3-5(a), to demonstrate and characterize our HEMT embedded metamaterial (MM) based terahertz (THz) modulator. From their initial development in the late 1980's, THz-TDS quickly matured to become the method of choice for THz spectroscopy offering room temperature systems with signal-to-noise ratio (SNR) performance in the excess of 80 dB [11, 169].

A typical THz-TDS system using photoconductive antennas is shown in Fig. 3-5(a) where an optical chopper is substituted with a THz metamaterial modulator that is described in the previous section. A 532 nm wavelength 4 W neodymium-doped yttrium aluminum garnet (YAG) laser beam is used to pump the titanium sapphire (Ti-sapphire) ultrafast laser that typically outputs a train of optical pulses centered about 800 nm wavelength ($\sim$ 100 fs in duration), at a repetition rate that varies from 70 to 100 MHz.

This ultrafast pulsed laser is split into two different paths using a beam splitter. One of the path is focused onto the photoconductive substrate gap between the two antenna arms fabricated on a GaAs substrate (Band gap of 1.42 eV = 874 nm). This fast (70-100 MHz) periodic excitation causes generation of carriers which are accelerated towards the antenna due to DC electric fields (typically DC bias voltage of 16 V). The transit time of these carriers in high electric field causes picosecond transient currents. These currents are made to radiate through antenna like structure on either side of electrode, which radiates THz electromagnetic radiation where the central emission frequency can be controlled by virtue of the antenna arms spacing ($\sim$ 0.3 THz for 80 μm spacing), and $E_{THz}(t)$ is proportional to the time derivative of the current density generated. This radiated broadband THz wave is collimated, to be carried over a long distance, and focused through the sample, recollimated and focused on to the detector.

The second path of the split pulsed laser is focused onto the photocon-

ductive substrate gap of the detector through a controllable delay stage. The detector is sensitive to the incident THz electric field $E_{THz}(t)$ for time increments that are much less the then 1 ps, thus by scanning the delay line a measure the of the $E_{THz}(t)$ as a function of time can be accomplished. An example of the measured time waveform is shown in Fig. 3-5(b) where the Fourier transform of the time signal calculates the frequency dependent complex electric field spectrum $E_{THz}(f)$ (magnitude shown in Fig.3-5(c)) [11]. The spectral resolution is inversely proportional to the length of the temporal scan.

On the detector side, a dipole antenna is used on top of a substrate material with optical generated carriers that boast very short carrier lifetimes, such as low temperature grown LT-GaAs, Er:GaAs nanoislands, or ion-implanted silicon-on-sapphire (SOS) [170]. The antenna is unbiased and a current is generated by combination of the photogenerated carriers which are accelerated by local THz electric field vector. Due to the short carrier lifetime, the photocurrent can be written as [169]

$$I(t) = \frac{1}{T}\int_0^T E_{THz}(\tau)\sigma(t+\tau)d\tau \tag{3.8}$$

where T is the repetition rate of the laser source, $\sigma(t)$ is the time dependent conductivity relating the free carriers optically excited in the substrate. If $\sigma(t)$ is a delta function the photocurrent will represent directly E_{THz}. This current is passed to a preamplifier and lock-in amplifier and outputs a measured DC voltage proportional to $E_{THz}(t)$.

3.4 Results and Discussion

3.4.1 THz Transmission with DC Biased HEMT

The device was characterized using a THz-TDS as discussed in the previous section (Sec. 3.3.2). The incident time-domain THz electric field ($\vec{E}_i(t)$) was polarized along the split gap to drive the metamaterial elements into resonance.

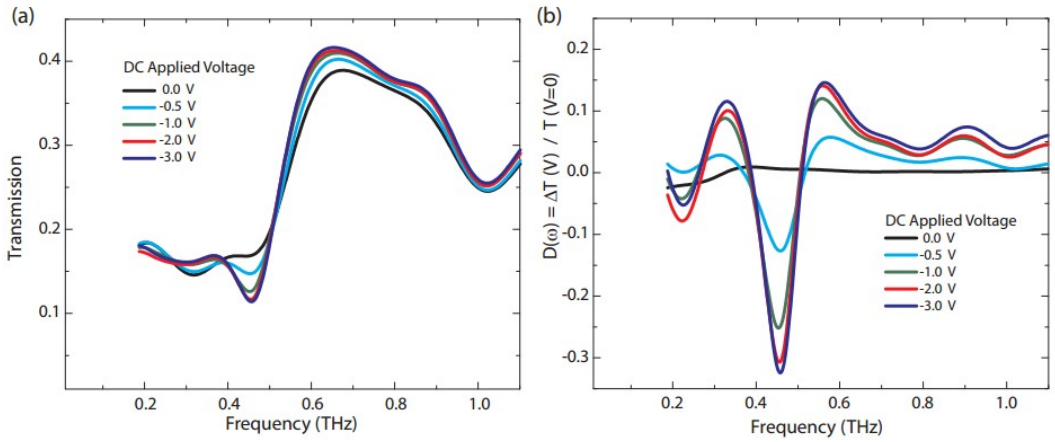

Figure 3-6: (a) Frequency dependent transmitted electric field for the HEMT / metamaterial device as a function of bias. (b) Voltage dependence of the differential transmission as defined in the text.

At the resonant frequency of the metamaterial, (0.46 THz), the electric field is concentrated within the split gaps of the metamaterial and is within the linear regime of the device owing to the low incident power used in experiments. The reference signal was measured with the sample removed from the beam path in order to normalize the data and calculate the absolute transmission. In Fig. 3-6(a) we show the transmitted electric field as a function of frequency for different V_{GS} values. For V_{GS} less than $-1.0V$, the channel is completely depleted, (see Fig. 3-4), and transmission shows a resonance at 0.46 THz. When the gate-to-source voltage is increased above $-1.0V$, the channel starts forming between the split gaps, and the metamaterial resonance begins to diminish. At $V_{GS} = 0V$, when the channel is completely formed, a low-impedance path at the split gap is created which effectively weakens the metamaterial resonant response. It can be seen in the transmission data (Fig.3-6(a)) that the frequency response shows no resonance at $V_{GS} = 0V$.

In order to elucidate the switching ability of the terahertz metamaterial, we plot the differential transmission in Fig. 3-6(b), defined as

$$D(\omega)_{V_{GS}} = \frac{T(\omega)_{V_{GS}}}{T(\omega)_{V_{GS}=0V}} \tag{3.9}$$

The black curve of Fig. 3-6 is a so-called 100% line, and is two successive transmission measurements divided by each other, both at V_{GS}=0. For a differential transmission of V_{GS}=-0.5V, cyan curve of Fig. 3-6(b), $D(\omega)_{-0.5V}$ is relatively flat with deviations from 100% of about 5% or less, except at a frequency of 0.46 THz, where a value of 87% is observed. This minimum in differential transmission is seen to increase for increasing V_{GS}, until at V_{GS}=-3.0 were a value of $D(\omega)$=67% is observed, again at 0.46 THz.

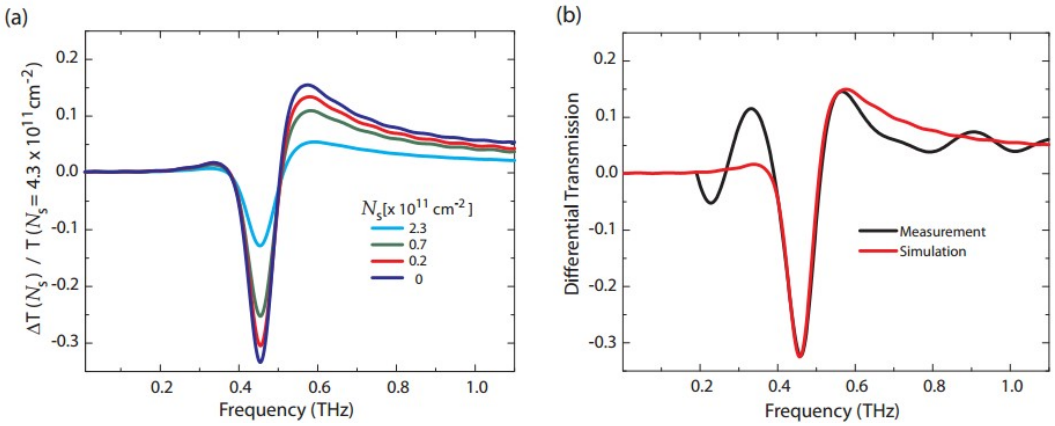

Figure 3-7: (a) Simulated differential transmission for various 2D carrier concentrations N_s. (b) A comparison of simulated (red) and experimental (black) differential transmission.

We computationally investigated the combined HEMT / metamaterial system. In recent years there has been considerable interest in 2DEG formation in HEMTs as a potential candidate for far-field THz wave interaction [134, 159, 171–174]. A majority of these applications revolve around utilizing the 2DEG instability in the HEMT channel. In our device the plasmon resonance resulting from the 2DEG instability does not play a roll. As such the parameter of interest for us is the near-field frequency dependent conductivity $\sigma(\omega)$. The dynamic response of the channel carriers can in many cases be described by the two-dimensional Drude conductivity as was shown in Eqn. 3.2 [163, 164]. It was also showin Eqn. 3.3 that the real and imaginary part of the conductivity can be represented as a series inductor and resistor in a equivalent circuit model as shown in Fig. 3-1(b). It can be observed from Eqn. 3.2 that

for low frequencies, the conductivity is purely real and hence the current is in phase with the electric field in the split gap, for frequencies near the scattering time-constant both the real and imaginary part is half the DC conductivity and the phase is 45 degrees. For much higher frequencies the conductivity asymptotically approaches zero.

Modification of charge density in a true 2DEG has no implications on the capacitance of a metamaterial owing to its infinitesimal thickness. However, the nature of our FDTD is inherently three-dimensional. Thus, if we simply change the carrier density this would falsely modify the capacitance of the metamaterial. In order to approximate the two-dimensional charge density we restrict the real part of the permittivity to be equal to epsilon infinity (12.9 ϵ_0 for GaAs) and allow the imaginary part to be modeled by the Drude model. The resulting complex permittivity can be expressed analytically as,

$$\epsilon(\omega) = \epsilon_\infty + i\omega_p^2 \frac{\omega_c/\omega}{\omega^2 + \omega_c^2} \tag{3.10}$$

where ω_c is the collision frequency and ω_p is the plasma frequency. The collision frequency $\omega_c = 2\pi \times 0.7$ THz is calculated with the relation $\omega_c = e \,/\, m^*\mu$ where μ the mobility of the channel along with both e and m^* the electron charge and effective mass in GaAs. The plasma frequency relation is $\omega_p^2 = e^2 N_s \,/\, \epsilon_0 m^* d$ where N_s is the two-dimensional carrier concentration and d is the simulated model thickness of the channel layer. We sweep the carrier concentration (See Fig.3-7(a)) in simulation observing a full resonant metamaterial response with a completely depleted channel ($N_s = 0\ cm^{-2}$) and a shorted response as the carrier concentration increased to (N_s = 7.3 x $10^{12} cm^{-2}$). Comparing this simulation with the experimental data shows excellent agreement (See Fig.3-7(b)).

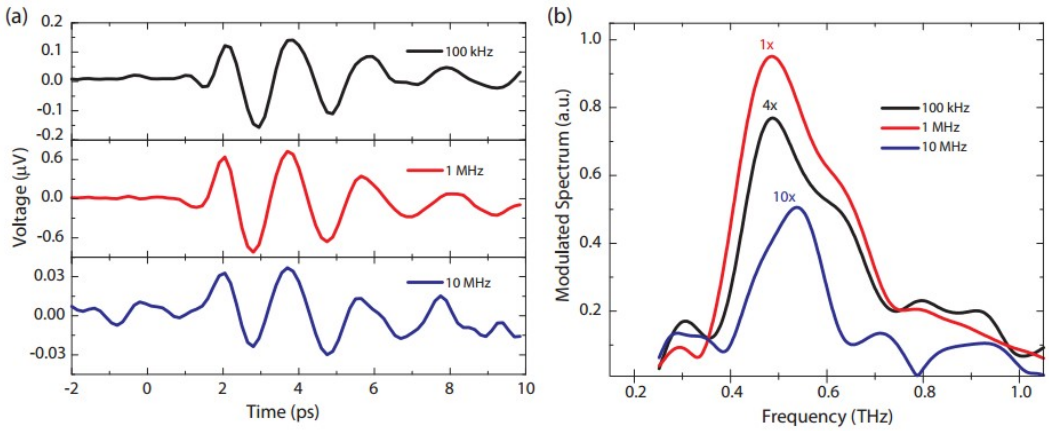

Figure 3-8: (a) Time domain data for modulation at frequencies of 100 Hz, 1 MHz and 10 MHz. (b) Spectra calculated from the time domain data.

3.4.2 High Frequency THz Modulation

In section 3.4.1 we demonstrated the ability to switch the THz waveform by adjusting the gate bias voltage of the HEMT with respect to the drain and source (V_{GS}). We now turn toward demonstration of high speed dynamic modulation and utilize a THz-TDS using a Photoconductive Antenna (PCA) emitter and detector. The standard mechanical chopper often utilized in a TDS system was replaced with our HEMT / metamaterial modulator which serves the same function as the mechanical chopper with the important distinction that now only a narrow band of frequencies about the metamaterial resonance is modulated. Therefore, the data has to be interpreted differently than the static case. A square-wave bias, alternating between -1.1 V and 0 V, was applied to the gate of the HEMT with respect to the source and drain. The same square wave signal was applied to the reference input of the lock-in amplifier. After collecting the entire time-domain THz signal we have a sampled signal which can be expressed as,

$$V_{out}(t) = \alpha|\vec{E}_{t0}(t) - \vec{E}_{t1}(t)| \tag{3.11}$$

where $\vec{E}_{t0}(t)$ and $\vec{E}_{t1}(t)$ are the time-domain electric-field of the transmitted THz signal when $V_{GS} = 0V$ and $V_{GS} = -1.1V$ respectively, and α is a pro-

portionality constant related to the particulars of the THz-TDS setup, such as the gain of pre-amplifier and averaging time-constant of the lock-in amplifier.

The time-domain signal $V_{out}(t)$ is plotted in Fig. 3-8(a) for three different modulation frequencies, 100 kHz, 1 MHz and 10 MHz. In Fig. 3-8(b) we plot the spectrum as obtained from Fourier transforming the time-domain data plotted in Fig. 3-8(a). It can be seen that the peak of the spectrum lies at 0.46 THz indicating modulation of the metamaterial resonance. Bandwidth of the spectrum remains relatively unchanged between 100 kHz and 100 MHz, and the amplitude of the spectrum increases. At a modulation rate of 10 MHz the bandwidth is observed to decrease a bit and the amplitude falls of from values observed at 1 MHz. The spectrum amplitude has a non-monotonic dependence as a function of frequency that can largely be attributed to the THz-TDS setup itself. PCA detection has known limitations in THz-TDS at high frequency modulation as documented in past work[175]. Contributions to the degradation of the spectrum amplitude from the HEMT / metamaterial device should remain small as there is several orders of magnitude separation between the gate-to-source modulated voltage and the input noise voltage as reported in HEMT performance studies[176]. In both the time-domain signal and the spectrum, the modulation amplitude falls off at higher frequencies and, for this device, the limit is in the neighborhood of 10 MHz. We attribute this as being primarily due to the parasitic capacitance and inductance in the chip assembly and, importantly, not a limitation of either the HEMT or metamaterial device.

3.5 Summary

We have demonstrated a HEMT / metamaterial device capable of modulation of THz radiation at frequencies up to 10 MHz, and modulation depths of up to 33% at 0.46 THz with all electronic control. A commercial GaAs process was utilized for implementation of the HEMT technology, as well as for fabrication

of the metamaterials. We achieved monolithic integration of a total of 2×10^4 active transistors at the metamaterial unit cell level. This work demonstrates a new path for construction of high speed terahertz electronic devices.

The cut-off frequency (f_T) of the pHEMT used is more than 50 GHz. So the switching limitation is primarily due to the parasitic capacitance associated with the chip design and the printed circuit board design. Now that the concept has been proven, the near term work would be to try and design it for much higher modulation speeds. Excess of 100 MHz should be achievable with careful design. The time-constant associated with the THz-TDS is probably in the 10 MHz range. So a new test methodology needs to be developed to test at much higher speed.

The immediate urgency of requiring high speed wireless communication with high spectral efficiency has researchers working hard to get that extra speed and efficiency. One way to achieve that in our present modulator is add multi-resonant frequency metamaterial elements in the modulator to simultaneously achieve multi-frequency modulation.

Chapter 4

Low-voltage High-speed Terahertz Spatial Light Modulator using Active Metamaterial

In recent years, terahertz (THz) imaging has captured significant interest because of it's potential for wide range of applications such as bio-detection[17], security screening[18], illicit drug detection[19] and skin cancer detection[20], to name a few. In spite of the intense research activity, simple and low-cost THz imaging systems are still not a reality. Unlike optical imaging, applying an isomorphic mapping of the object on to a THz focal plane array is still a complex and expensive problem. The primary reason for the difficulty is the lack of suitable materials for construction of imaging devices in the terahertz regime (0.1 - 10 THz, $\lambda = 3mm - 30\mu m$), so called the 'THz Gap'[2]. Although real-time terahertz imaging has been demonstrated using focal-plane arrays[45, 177], they tend to have higher complexity and operational cost. A different approach is becoming more practical for THz imagers where, a single-pixel detector is used instead and the incident THz wave is spatially modulated

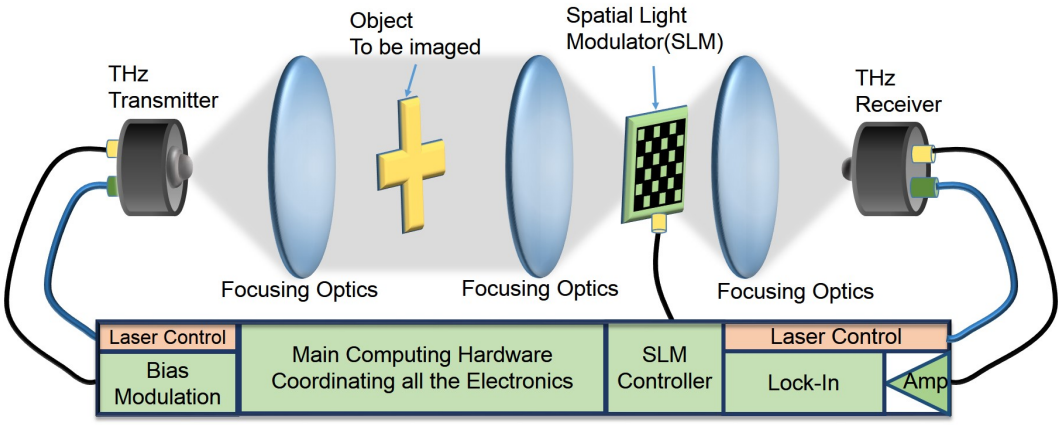

Figure 4-1: A compact and low-cost single-pixel THz imaging system. A fiber-coupled photoconductive antenna generates terahertz (THz) frequency based on the incident laser beat frequency. The THz wave is collimated using focusing optics which illuminates an object that is focused on to a metamaterial based Spatial Light Modulator (SLM). Using compressed sensing (CS) techniques, optimum number of masks or coded apertures are generated using the electronically controlled SLM. The partially transmitted THz wave is then focused on to a fiber coupled THz receiver antenna which measures the aggregate power of the incident THz wave. Computational imaging approach is employed to reconstruct the image from coded aperture measurements.

at the image plane through a coded aperture based on an advanced signal processing theory called compressed sensing (CS)[126, 178]. Such a system, which is relatively compact and low-cost, is schematically illustrated and explained in Fig. 4-1.

The key to single-pixel imaging is to come up with a smallest set of coded masks at the SLM plane, where the image is reconstructed from those encoded single-pixel measurements[125, 126, 178] (For details see section 4.1). The electronically controlled SLM avoids any mechanical movements as in raster scan thus further improving the speed of acquisition. Although the CS techniques dramatically reduces the number of scans, it is still multiple scans for each image reconstruction. Therefore, it is critical for the SLM to have a high switching speed with low-voltage operation that can preferably be integrated within a system-on-chip (SoC) to achieve the speed, power and cost objective for such a system. Significant amount of research effort has been focused in the area of spatial light modulators (SLM) including SLMs based

on digital micromirror devices (DMD)[179], micro-electromechanical systems (MEMS)[180], liquid crystal on silicon (LCOS)[181] and graphene-metal plasmonic antennas[182]. These devices perform well for frequencies in the infrared (IR) to visible range and are lossy and incompatible for THz frequencies. These devices can be used in THz SLM applications by creating optical patterns on THz transmissive devices by a reflection geometry[125]. The disadvantage of such a setup is higher complexity and cost.

Recent research has demonstrated THz SLMs using all-electronic dynamic metamaterials used in single-pixel THz imaging systems[124, 125, 158]. These dynamic metamaterial SLMs are electronically controlled by injecting charges or depleting them in the bulk semiconductor substrate, which is an inherently slow process due to the intrinsically large capacitance of what is essentially a large bulk diode structure[84, 140, 158]. This results in a slow switching speed and large dynamic power consumption. Moreover, in typical integrated circuit (IC) processes, this large diode needs 15V-50V to completely deplete the charges. Finally, in such bulk-bias system, on-chip circuits cannot be used making it incompatible with IC integration.

We demonstrate an all solid-state terahertz SLM fabricated using a matured commercial GaAs technology used for high-volume mobile phone applications that operates at room temperature using a 1V supply, and consuming less than 1 mW of power making it an ideal candidate for consumer grade applications. The SLM is built from the metamaterial described in chapter-3, electrically controlled using pseudomorphic high-electron mobility transistor (pHEMT) that is embedded in the split gap of each unit cell [101]. Using a high speed transistor instead of a bulk semiconductor for active electronic control, we achieve much higher speed of modulation ($\sim$ 10 MHz) and consume much lower power.

4.1 Introduction to Single Pixel Imaging

4.1.1 A Brief Historical Perspective

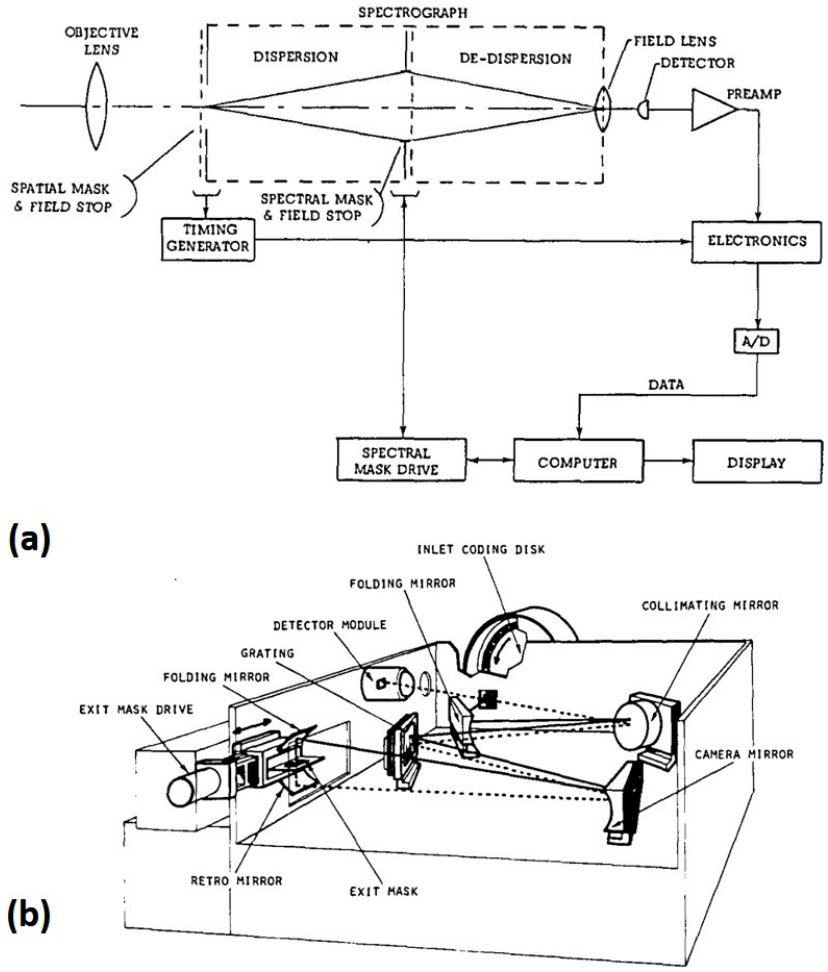

Figure 4-2: One of the first single-pixel imaging instrument to use binary optical masks based on Hadamard transforms [183]. (a) Block diagram of the Hadamard transform imaging spectrometer system. (b) Drawing of the interior of the spectrometer.

The principle behind a single-pixel imager was first demonstrated by Golay in 1949 [184], as a method to achieve faster acquisition rate and higher signal-to-noise ratio (SNR) for infrared (IR) spectrometry. In this remarkable work, he demonstrated the use of modulating mask pattern to measure the spectral information in a dispersive IR spectrometer. His work was way ahead of time when he realized the importance of orthogonal binary digital codes more than

two decades before digital computers were to become standard equipment in many laboratories.

Some twenty years after Golay's work, there was revival of his instrumentation techniques but it was not until 1976, until the development of modern computer, that the work by Swift *et. al.* demonstrated the first single-pixel imager using binary optical masks based on Hadamard transform [185], what is known today as compressed sensing [126, 178]. The block diagram and the interior construction of that spectrometer is shown in Fig. 4-2. As shown in the block diagram, this is a spatial spectrometer which captures both spatial and spectral information. Therefore, there two sets of Hadamard masks used in this spectrometer: first set at the entry of the spectrograph to decode the spatial information and the second set at the dispersed plane where the spectral information is dispersed on to a spatial plane. A detail principle of the imaging theory will be explained next.

4.1.2 Imaging Theory

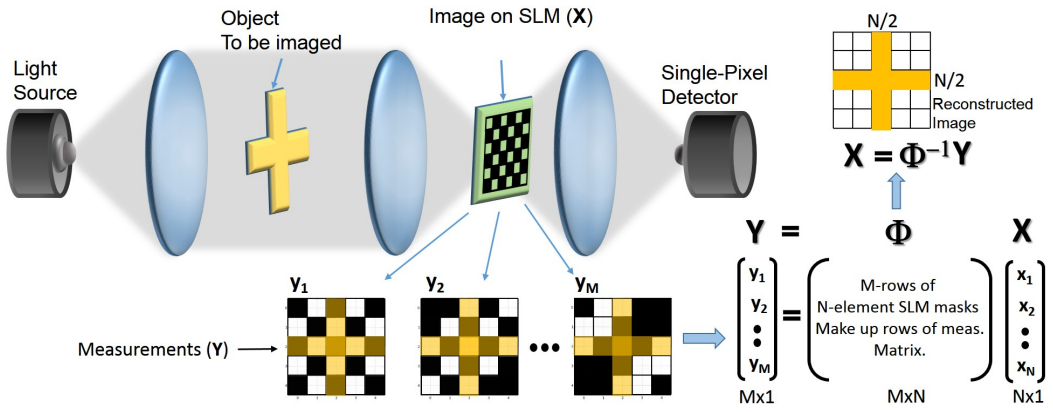

Figure 4-3: Schematic depiction of the single-pixel multiplex imaging process where the SLM is used to spatial modulate N-pixel image with M-set of known masks and reconstruct the image from the M single-pixel measurements.

Typical single-pixel imaging setup involves a light source, imaging optics, a single-pixel detector and a spatial light modulator (SLM) as illustrated in Fig. 4-3. Light from a illuminated object is focused on to a SLM which,

for binary encoding, selectively passes light on to the single-pixel detector. A sequence (M) of known patterns are displayed on the SLM and single measurements are taken using the detector for each mask or coded aperture resulting in M sets of *single-valued* measurements. Prior knowledge of these masks allows for the reconstruction of a N-pixel image from M measurements. Significant research has been done since the late 1970s in the field of signal processing and information theory to compress the amount of measurements such that $M \ll N$.

The choice of the type of SLM is usually dependent on the type of the single-pixel detector. For an imaging system with intensity based single-pixel detector, binary masks that modulate the intensity are well suited. The field of compressed sensing/imaging is mostly dominated by random and Hadamard based masks [126, 178, 183]. Random binary masks are comprised of 1's and 0's determined by standard random distributions such as Gaussian and Bernoulli. Typically, Hadamard masks are square matrices comprised of (1, -1) where each row is orthogonal to all other rows, but Hadamard matrices comprised of (-1, 0, 1) and (0, 1) are also used and it is proven in [183] that the average mean square error for the best mask of (0, 1) is about four times that for the best mask of (-1, 0, 1). Binary masks have also been created using S-matrix, created by omitting the first row and column of the corresponding normalized Hadamard matrix, substituting (-1, 1) with (1, 0). Using of S-matrix was demonstrated in a terahertz single-pixel imaging experiment in [125].

If we define a one- or two-dimensional image by a vector $\mathbf{X}$ with N-pixels, we do a single measurement y_j for each set of mask with N-elements, the measurements can be expressed in a matrix form

$$\mathbf{Y} = \mathbf{\Phi X} \tag{4.1}$$

where $\mathbf{Y}$ the column vector with M-elements representing the M measurements and $\mathbf{\Phi}$ is the $M \times N$ matrix representing the M N-element masks used

to make the measurements. For the trivial case of raster scanning the entire image, $\mathbf{\Phi}$ is a $N \times N$ identity matrix. For a well-conditioned measurement matrix $\mathbf{\Phi}$, the reconstructed image $\mathbf{X}$ can simply be expressed in the matrix form

$$\mathbf{X} = \mathbf{\Phi}^{-1}\mathbf{Y} \tag{4.2}$$

Thus, utilizing this new sampling paradigm of compressed sensing (CS), an image is reconstructed, with a bounded error, using fewer measurements than typically needed for a given given resolution determined by the Nyquist theorem (N) i.e., $M < N$ [186]. The underlying premise which makes CS possible is that most images of interest are sparse in nature.

Even after decades of research, two major problems which still plaque single-pixel compressive imaging: first, it is computationally very intensive due to it's inherent nature of being a NP-hard optimization problem; second, although the number of measurements are greatly reduced, it is still a serial process making video rate imaging a great technical challenge. Next we look at few research works using spatial light modulators for single-pixel terahertz imaging.

4.1.3 A Review of THz Spatial Light Modulators

Since the first demonstration of compressive imaging with single-pixel system, there has been significant interest in extending the technology to larger wavelength in the terahertz (THz) regime due to lack THz focal plane arrays. However, due to lack of commercial solid-state spatial light modulators (SLM), early research on THz single-pixel imaging had to resort to mechanically scanned apertures [18, 19, 187]. More recently, metamaterial based SLMs are showing promise in single-pixel imaging [84, 86, 124, 125, 158, 165].

A single-pixel terahertz imaging setup using CW pumped high-resitivity silicon (ρ-Si) as a spatial light modulator was demonstrated in [125], a schematic of the setup shown in Fig. 4-4. As shown in the schematic, a collimated LED

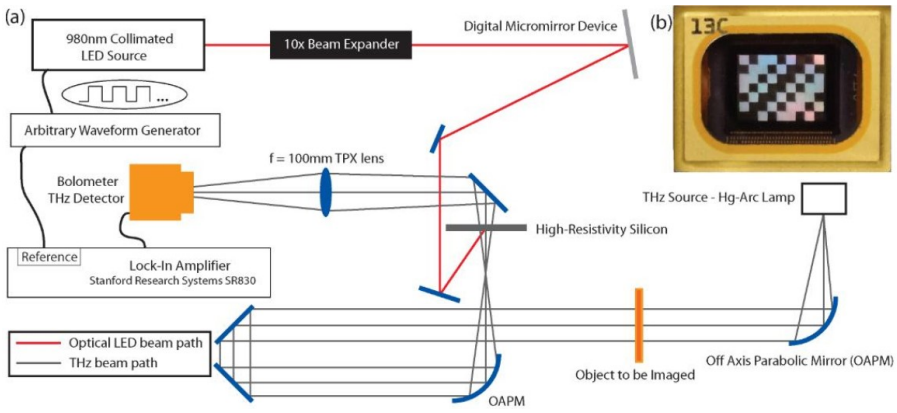

Figure 4-4: Schematic of a single-pixel terahertz imaging setup using CW pumped high-resitivity silicon as a spatial light modulator [125].

source is spatially modulated with the desired coded masks using a commercial digital micro-mirror device (DMD) and focused on to the ρ-Si to create the THz SLM. The principle of operation lies in the fact that CW pumped ρ-Si behaves as THz modulator due free carrier generation and linear recombination in the semiconductor changing the complex dielectric constant that can be described by the Drude model [188]

$$\epsilon(\omega) = \epsilon_\infty - \frac{\omega_p^2}{\omega(\omega + i\Gamma)} \tag{4.3}$$

A fundamental limitation of this technique is the carrier lifetime of ρ-Si of $\tau = 25\ \mu s$ limits the switching speed to about 10 kHz. Moreover, the LED source, DMD and the optics to create the spatial CW pumping, makes the system complex and expensive.

Figure 4-5(a,b) shows the SLM based on multi-resonant, electronically controlled metamaterial absorber [165]. The overall SLM system architecture is shown schematically in Fig. 4-5(b) and consists of metamaterial absorber pixels flip chip bonded to a Silicon chip carrier with routing to bond pads which are wire-bonded to a leadless chip carrier (LCC). The metamaterial absorber consists of two metallic layers with a dielectric spacer lying in-between. The top metal layer is patterned in order to respond resonantly to the electric component of an incident electromagnetic wave. A bottom ground plane layer

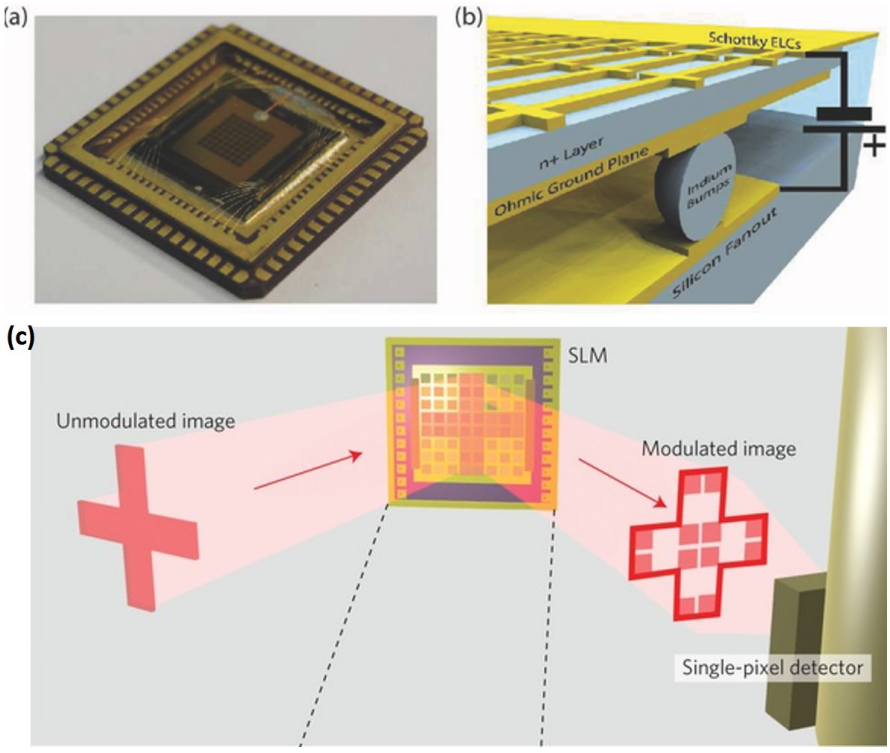

Figure 4-5: (a,b) Design and structure detail of the electronically controlled THz metamaterial absorber based spatial light modulator (MMA-SLM) [165]. (a) Image of MMA-SLM as assembled in chip carrier package. (b) Cross-sectional schematic view of a single pixel. (c) Schematic of a THz compressive imaging setup using the SLM in (a,b) [124].

is spaced relatively close to the top layer, thus allowing the external magnetic field to couple, as shown in Fig. 4-5(b). The SLM was demonstrated in a single-pixel compressive imaging experiment using a reflection geometry [124], a schematic of the setup shown in Fig. 4-5(c). The same SLM has also been used in recent works involving single pixel quadrature imaging [189] and frequency-division-multiplexed single-pixel imaging [190]. This electrically controlled SLM is a great improvement over the optically pumped SLM allowing for simpler and cheaper THz imagers. However, having to use a certain height of dielectric to design for a desired resonant frequency for the absorber makes the design very rigid and precludes the use of commercial foundry process where the vertical dimensions are fixed. Additionally, reflection geometry imaging setups add to the complexity and hence the cost.

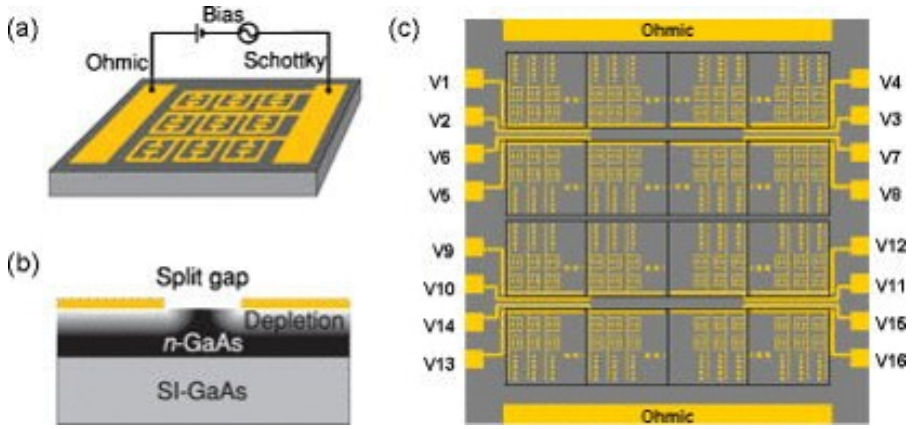

Figure 4-6: A solid-state spatial light modulator for terahertz frequencies (0.36 THz)[158]. Schematic showing (a) each single pixel on the metamaterial based terahertz SLM. A voltage bias controls the substrate charge carrier density near the split gaps, tuning the strength of the resonance, (b) the substrate and the depletion region near the split gap of a single SRR, where the gray scale indicates the free charge carrier density, (c) the terahertz SLM (not drawn to scale) is a 4×4 array of individual pixels in (a). Each pixel is independently controlled by an external voltage (16 V) between the 1×1 mm^2 Schottky electric pad and the ohmic contact.

One of the first electronically-controlled, all solid-state terahertz SLM was demonstrated by Chan *et. al.* [158] in 2009 using an active metamaterial design demonstrated earlier by Chen *et. al.* [84] in 2006. As shown in Fig. 4-6(a,b), the modulator is based on the principle of shunting the metamaterial

split gap by injecting carrier in the substrate using an external bias voltage between the metamaterial and the substrate. Fig. 4-6(c) shows the SLM assembly of 4×4 array of individual pixels. Each pixel is independently controlled by an external voltage between the 1×1 mm^2 Schottky electric pad and the ohmic contact. The SLM was characterized in a transmissive geometry at 0.36 THz with modulating voltage of 16 V at switching speed of kilo-hertz. Although this work marked the beginning of solid-state THz SLMs, there are few drawbacks associated with the bias voltage being applied across the entire substrate. Biasing the entire substrate precludes it from being used on systems-on-chip (SoC) applications, a main attraction of solid-state SLMs. The switching speeds are slow due to the large associated capacitance of the substrate and the switching voltage is high related to the breakdown voltage of the substrate.

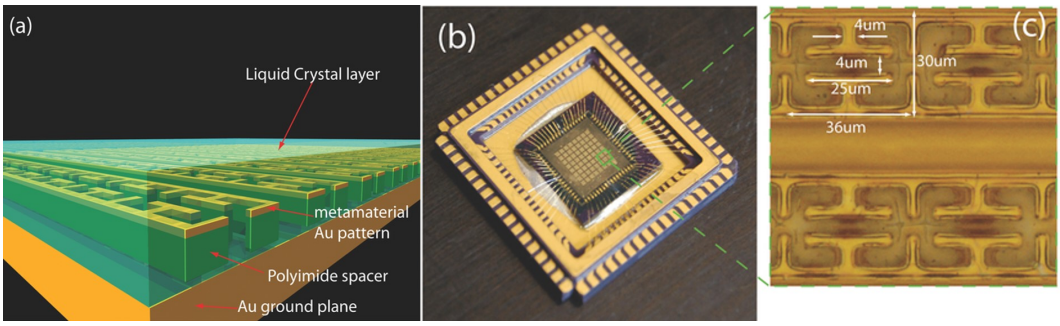

Figure 4-7: Liquid Crystal (LC) Metamaterial Absorber (MMA) Spatial Light Modulator (SLM) for THz Applications [191]. (a) 3D cross section schematic of the MMA array covered with LC. (b) Picture of the MMA SLM device coated with LC. (c) Close up of MMA unit cells.

Although advances have been made in liquid crystal on silicon (LCOS) spatial light modulator technology [181], there applications in terahertz has been limited. More recently, metamaterial absorbers embedded in liquid crystals were demonstrated in reflection geometry as terahertz spatial light modulators [191], Fig. 4-7. As shown in Fig. 4-7(a), the liquid crystal (LC) forms the dielectric in the split gap of the resonator. By applying a bias voltage and thus electric field across the LC, the polarization of the LC is changed which in turn changes the resonant frequency of the absorber, resulting in voltage controlled

modulation. This work showed the viability of using a liquid crystal with metamaterial absorbers with results of 75% modulation depth at 3.76 THz. Although promising, the use of 15V switching voltage, modulation speeds of only 1 kHz and ~70% signal absorbtion are significant drawbacks of the technology to make it a serious contender for THz SLM.

In the next sections we detail the design and characterization of a terahertz SLM that aims to solve some the major problems stated in the previous works.

4.2 Spatial Light Modulator Design and Assembly

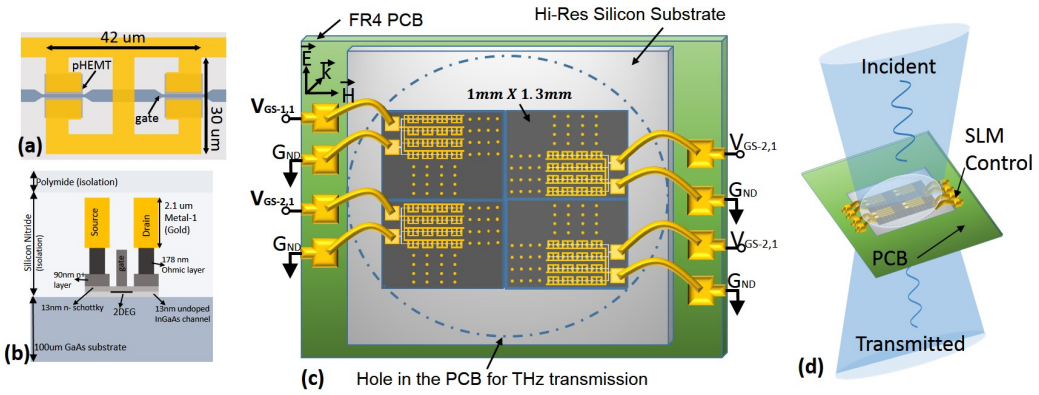

Figure 4-8: SLM design and assembly details. (a) Each metamaterial element is based on the electric-LC (ELC) resonator, patterned using the top 2.1μm thick gold metal. A pseudomorphic high-electron mobility transistor (pHEMT) is placed underneath each split gap with their source and drain connected to each side of the split gap (See chapter 3 for details). (b) Close-up diagram of the split-gap shows the placement of the HEMT device with it's drain and source connected to both ends of the split gap. (c) The 4-pixel THz SLM is arranged as an 2x2 array. Each pixel is controlled by its respective row and column voltage source (0-1V) to control the transmission of the incident THz wave. Each pixel is 1.0 X 1.3 mm^2 with 551 metamaterials elements with an active area of 0.88 X 1.12 mm^2. The gates of the embedded HEMTs are connected together to a 100 X 100 μm bond pad using first-level metal. Similarly, the source/drains of the HEMT, through the metamaterial, are connected to another bond pad. (d) Experimental configuration for THz transmission measurements through the SLM device. The electric field is polarized perpendicular to the split gap as shown in (c).

The basic principle of our THz SLM is based on an electronically controlled resonant frequency in a metamaterial using embedded pseudomorphic high electron mobility transistor (pHEMT) devices as described in detail in section 3.1. The pHEMT is used to shunt the split-gap capacitor of each ELC element [101](Fig-4-8(a-b)), which increases the loss of the resonator resulting in a lower absorption at the resonant frequency. Thus by electrically controlling the 2-D electron "gas" (2DEG) density across the split gap, we are able to modulate a terahertz (THz) wave using voltage control. Because of the localized pHEMT in the split-gap, the device has been demonstrated for fast modulation ($\sim 10\ MHz$)[101](See chapter 3) that is capable of much higher speed with proper design. Compared to other electrically controlled metamaterial[84, 88], where the whole substrate is used to control the resonance, this device offers element-level control that offers higher switching speed and offers future opportunity of creating more exotic devices.

The metamaterial design was fabricated using a commercial GaAs process with an active device that is a planar-doped pseudomorphic HEMT (pHEMT) based on AlGaAs-InGaAs-AlGaAs quantum well heterostructure[161]. Based on the design principle explained in the previous section, the metamaterial device is constructed of a planar array of subwavelength-sized ELC resonators using the top metal layer, $2.1\mu m$ thick gold (Fig.4-8(a)). Qualitatively, the two rings provide a equivalent inductance of L_{MM} and the two split gaps with a total capacitance of C_{MM} as shown in the equivalent circuit in Fig-3-2(b). R_{MM} is the total equivalent loss of the resonator. Dimension of each element is 42 μm wide by 30 μm in height and they are repeated with a period of 55 μm $\times$ 40μm. The line width of the metamaterial is 4μm and the split gap is 3 μm. The entire unit cell was modeled using a commercial finite difference time domain (FDTD) solver, CST's Microwave Studio, in which the metamaterial was designed to be resonant at 0.45 THz. The resonant frequency is electrically controlled using an enhanced mode pHEMT that is embedded in the split gap of each ELC element[101](Fig-4-8(b)). Magnified pictures of the SLM is shown

in Fig. 4-9(c-d).

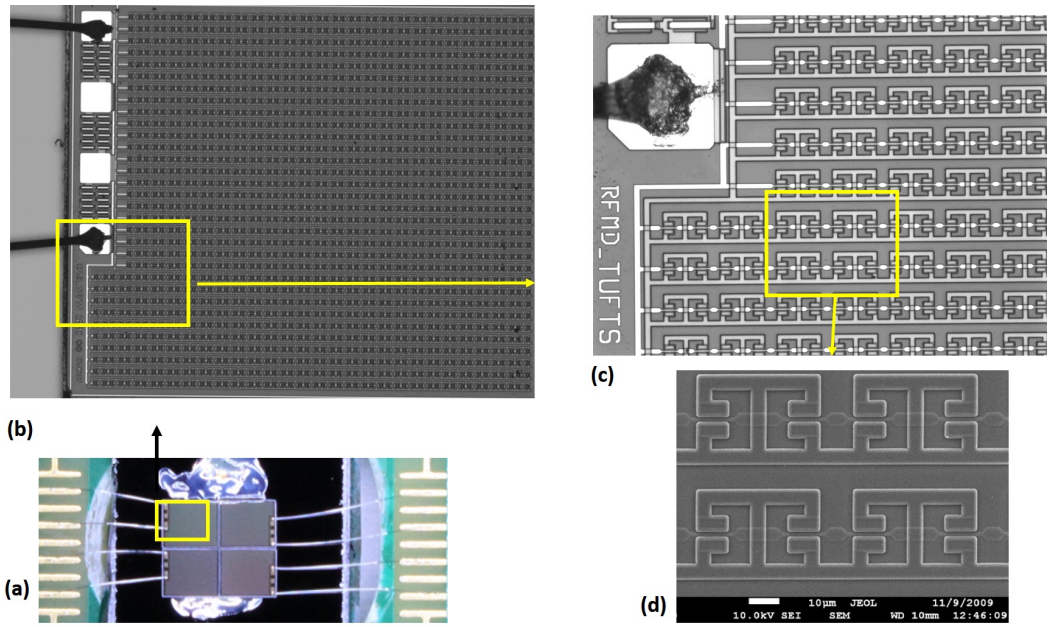

Figure 4-9: Magnified pictures of the SLM and the metamaterial. (a) Close-up picture of the SLM assembly on a Hi-res silicon that is mounted on PCB and wire bonded to copper traces on the PCB. (b) Magnified picture of one the dies in the region shown in the yellow box in (a) below (c) Magnified picture of the die near a pad showing all the drain/source connection and all the gates connected to the pad. (d) A SEM picture of the metamaterial structure.

To demonstrate our terahertz SLM, we constructed a 2x2 pixel device, where each pixel is $1.0 \times 1.3mm^2$ with 551 elements with an active area of $0.88 \times 1.12mm^2$ for each pixel as schematically shown in Fig.4-8(c) and picture of the assembly in Fig. 4-9(a). The 2x2 array is die-attached (only at the corners) to a high-resistive silicon ($\rho - Si$) substrate that is mounted on a FR-4 based PCB with a hole underneath the $\rho - Si$ to allow THz transmission. All the gates of the HEMTs for each pixel are connected to a 100 μm X 100 μm bond pad and all the metamaterials for each pixel are connected to a separate bond pad which provides the DC bias for the drain/source connection. These bond pads are bonded out to the test circuit board such that each pixel can be biased (V_{GS}) independently thus enabling a 2x2 electrically controlled terahertz SLM.

4.3 Circuit Design for Electronic Control of the SLM

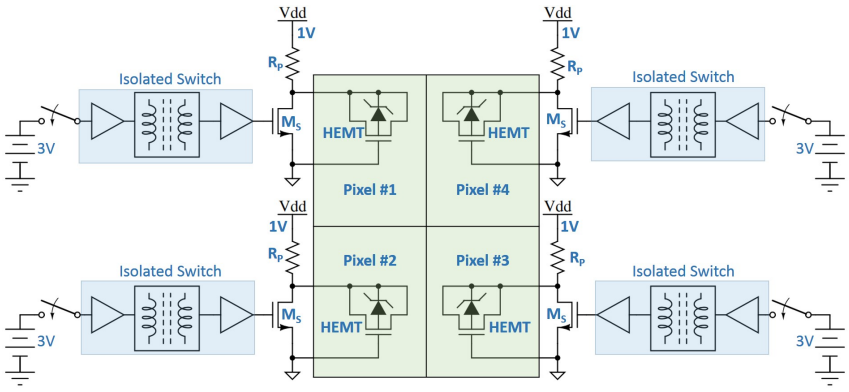

Figure 4-10: A top level view of the circuit architecture to control the SLM.

Figure 4-10 shows the top level architecture of the circuit to electronically control the SLM. The VGS of all the embedded HEMTs in a pixel is controlled by an identical circuit. The VGS of all the HEMTs are represented by one device in the figure essentially all schottky diodes in parallel. The VGS is switched between 0V and -1V using the MOSFET M_S and the pull-up resistor R_P. In order to switch "on" a pixel ($V_{GS} = -1V$), the MOSFET M_S for that particular pixel is switched off which pulls drain/source of the HEMTs to Vdd (1V) and to switch "off" the pixel ($V_{GS} = 0V$), the MOSFET is turned on and the drain/source of the HEMTs are pulled down to ground. The gate of the MOSFETS are driven by an isolated switch to eliminate any ground noise from the switching side since that is controlled by the computer through long wires creating lot of ground bounce. The details of the control circuit is shown in the next figure.

Figure 4-11 shows the details of the circuit, including the part numbers and the values, used to control one of the SLM's pixel. All the HEMTs of a pixel are represented by the schottky diode DGS. The zener diode Z1 and capacitor C1 are used to filter any large transients during the switching to avoid damaging the HEMTs. M1 and R1 are used to switch the VGS of the

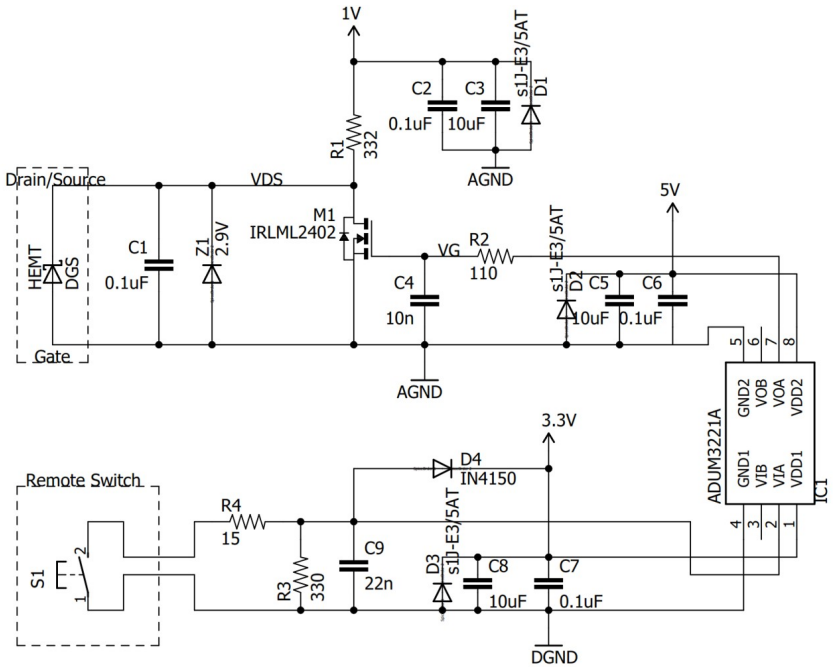

Figure 4-11: Details of the circuit, including the part numbers and the values, used to control one of the SLM's pixel.

HEMTs as explained in the previous figure. Capacitor C1 and C2 are used to filter any noise on the 1V supply. D1 is for protection against wrong polarity. R2 and C4 are used to filter large transients at the gate of the MOSFET. C5, C6 and D2 are used to filter and protect the 5V supply on the board. IC1 (Analog Devices ADUM3221A) is transformer based isolated switch that blocks any noise in the switch (S1) side since typically that is a noisy domain. Switch S1 is connected to the PCB board via a long wire since this is remote to where the metamaterial SLM is placed. Therefore, R3, R4, C9 and D4 are used to eliminate the large transients and smooth the transitions. C7, C8 and D4 are used to filter the noise and protect the 3V supply used to power the switching side of the isolator.

Figure 4-12 shows the PCB design for the electronic control of the SLM. Fig. 4-12(a) shows the mounted PCB with all electronics (except for the switches) for controlling the SLM pixels. In the middle of the PCB is the daughter card with the SLM pixels which is mounted on a high-resistivity (Hi-res) silicon substrate with a hole in the PCB for THz transmission tests.

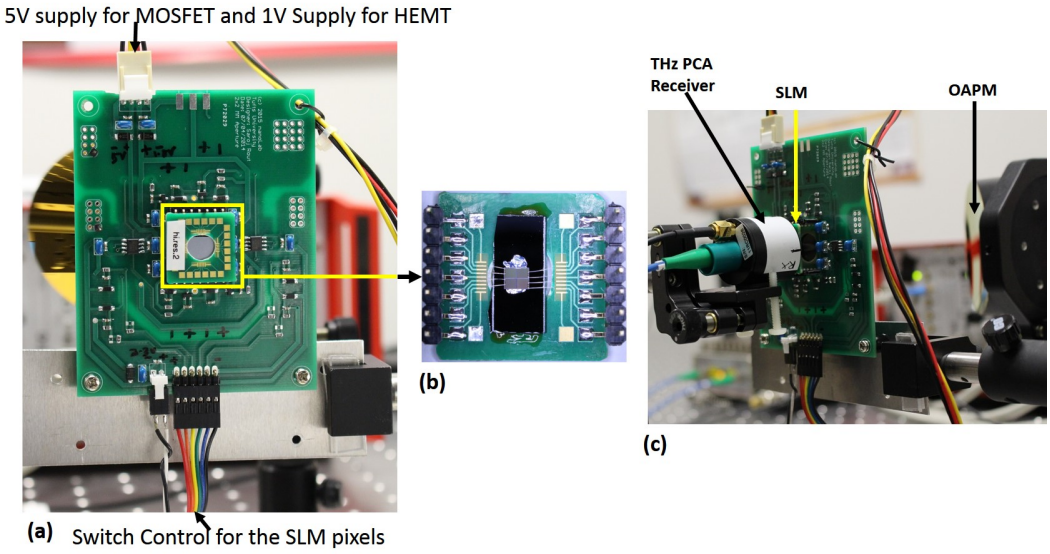

Figure 4-12: Printed circuit board (PCB) for electronic control of the SLM.

The power supplies are well grounded and shielded for noise immunity. Fig. 4-12(b) shows the back side of the daughter card showing the SLM assembly on a Hi-res silicon. The four metamaterial dies are attached using a high-viscosity die attach to avoid any material in between the metamaterial and the Hi-Res silicon. The drain/source and the gate connections for the bond pads are wire bonded to the PCB which is electrically connected to the right-angle pins that is use to insert the daughter card in the main PCB. Fig. 4-12(c) shows the picture of the setup near the THz receiver. It can be seen front he picture that the receiver is placed right behind the SLM as single-pixel detector.

4.4 Experimental Setup for Terahertz Characterization and Imaging

A schematic of the THz imaging and characterization system is shown in Fig. 4-13. Our terahertz SLM is characterized in transmission mode using a commercial continuous-wave (cw) THz spectroscopy system, TeraScan 1550 by Toptica Photonics[192]. The CW terahertz spectrometer generates linearly polarized THz frequency from 60 GHz to 1.2 THz using a pair of tuned

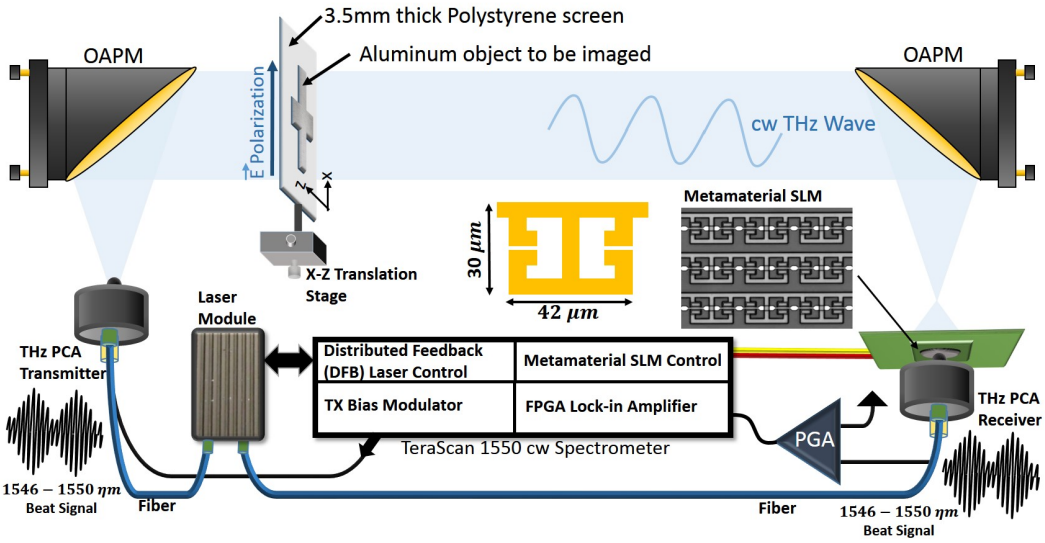

Figure 4-13: Experimental setup for terahertz characterization and imaging. Schematic diagram of the continuous-wave (cw) terahertz setup for characterizing the metamaterial SLM. The magnified picture of the metamaterial is shown in the inset and the yellow overlay shows the geometry of each unit cell. A fiber-coupled photo-conductive antenna generates the THz wave from laser beat signal that is collimated and focused by a pair of Off-Axis Parabolic Mirrors (OAPMs). The object, an aluminum metal cross on a 3.5mm thick polystyrene screen is placed in the path of the collimated beam. The metamaterial SLM is placed 15mm away from the focal point and the single-pixel THz detector is placed right behind the SLM. The receiver photocurrent is first amplified by a programmable gain amplifier (PGA) and then lock-in detected by a custom FPGA

lasers (1546 and 1550nm). The temperature controlled beat frequency is fiber-coupled to a InGaAs photo-diode with a bow-tie antenna which is bias modulated ($\pm 1.2V$) at 7.629 kHz. The THz imaging optics consist of two 76.2 mm diameter 90^o off-axis parabolic mirrors (OAPMs) each with an effective focal length of $f_L = 152.2\ mm$. The source-side OAPM is f_L from the source and back-illuminates the object a distance 200 mm away. The second OAPM, a distance 800 mm from the object, focuses the radiation and forms a conjugate image on the SLM 167.2 mm away. The system has an overall magnification of 0.24, mapping a 35 mm diameter object to 8.4 mm. Please note, the correct image plane is 184 mm away from the second OAPM with a overall magnification ratio of approximately 0.5. Given limited Signal-to-Noise Ratio (SNR), acquiring image with adequate fidelity at the image plane was challenging.

The choice of our SLM location was based on the optimum SNR vs. resolution. The THz detector (fiber-coupled InGaAs photo-mixer) is placed right behind the SLM to measure the aggregate THz radiation power passing through the SLM. Since the diameter of receiver's semi-hemispherical silicon lens is approximately the size of the SLM, we avoid the second set of optics to give us better fidelity i.e. SNR. The SLM orientated such that, the linearly polarized electric field of the THz wave is across the split gaps of the metamaterial elements. The detected photo-current is pre-amplified using a programmable gain amplifier (PGA) and then lock-in detected ($\tau = 620\ ms$) using Toptica's proprietary FPGA module. The detected photocurrent I_{ph} can be expressed as $I_{ph} \propto E_{THz} cos(\Delta\phi)$ [193] where, E_{THz} is the amplitude of the terahertz electric field and $\Delta\phi$ is the phase difference between the terahertz wave and the laser beat signal at the detector. Therefore, the detected photocurrent I_{ph} oscillates with the THz frequency with the period set by the length of the terahertz beam. The frequency response of a sample is calculated by measuring the envelope of the oscillating I_{ph}. The oscillating period limits the frequency resolution, which was ≈ 0.2 GHz for our setup.

For proof of concept, we imaged an object that is 15 mm wide aluminum

cross placed on a 3.5mm thick polystyrene screen which is opaque to visible light but transparent to 0.45 THz. The object was raster scanned 3x3 with a step size of 15 mm and for each raster position the SLM scans a 2x2 image resulting in 6x6 image size with 7.5 mm physical resolution. Raster scanning would not have been necessary if we had implemented an 6x6 array of SLM.

4.5 Results and Discussions

4.5.1 Terahertz Characterization of the Spatial Light Modulator

We characterized our SLM and performed our single pixel THz imaging in a transmission geometry using the experimental apparatus shown in Fig. 4-13. All the characterization was done without the object, with the SLM and the detector placed at the focal point of the OAPM for maximum Signal-to-Noise Ratio (SNR). Fig-4-14(a) shows the transmission spectra using the envelope of the detected current as each of the four pixels are turned "on"($V_{GS-i,j} = -1V$) and "off"($V_{GS-i,j} = 0V$) sequentially in a clockwise or anti-clockwise direction where i and j correspond to the row and column respectively. The spectra for each SLM configuration is result of a frequency scan from 447 GHz to 455 GHz with a step size of 0.005 GHz and lock-in time-constant of 620 ms. Fig-4-14(b) shows the extracted photocurrent from the transmission spectra at f=450.2 GHz. Between all 4 pixels "on" and "off", an amplitude modulation depth of 36% is measured and an average of 9% modulation depth for each pixel at the designed resonant frequency of 0.45 THz. In order to emphasize the spatial modulation near the resonant frequency, the modulation spectra for each pixel is plotted relative to a reference. Fig-4-14(c) shows the differential transmission spectra extracted from the data in Fig-4-14(a). The reference for the differential spectra is when the SLM transmission is maximum i.e. all the metamaterials are "off" ($I_{ph_ref}(f) = I_{ph}(f)[V_{GS} = 0V$ for all MM]). Then for

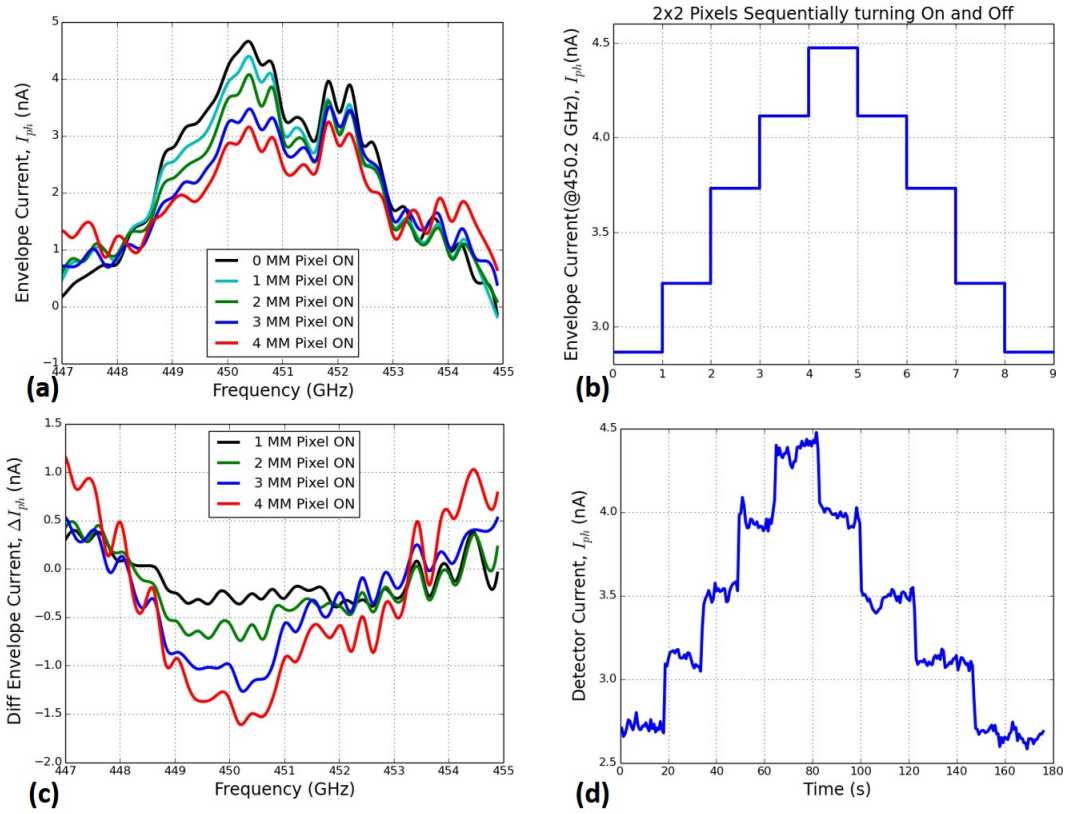

Figure 4-14: Terahertz Characterization of the Spatial Light Modulator. Characterization of the 4-pixel(2x2) SLM as the pixels are turned "on" and "off" sequentially in clockwise and anti-clockwise direction. (a) Transmission spectra using the envelope of the detected photocurrent, I_{ph}. (b) The envelope photocurrent from the transmission spectra at 450.2 GHz. (c) The differential transmission spectra (ΔI_{ph}) with reference spectra of maximum transmission i.e. all the metamaterials are "off" ($I_{ph}(V_{GS} = 0V$ for all MM)). (d) Real time detected photocurrent at 450.2 GHz.

each SLM configuration the differential spectra is expressed as $\Delta I_{phN}(f) = I_{phN}(f) - I_{ph_ref}(f)$ where, N denotes one of the 4 pixels. Fig-4-14(d) shows the real time SLM response to a continuous THz wave of 0.45 THz.

4.5.2 Single-Pixel Terahertz Imaging

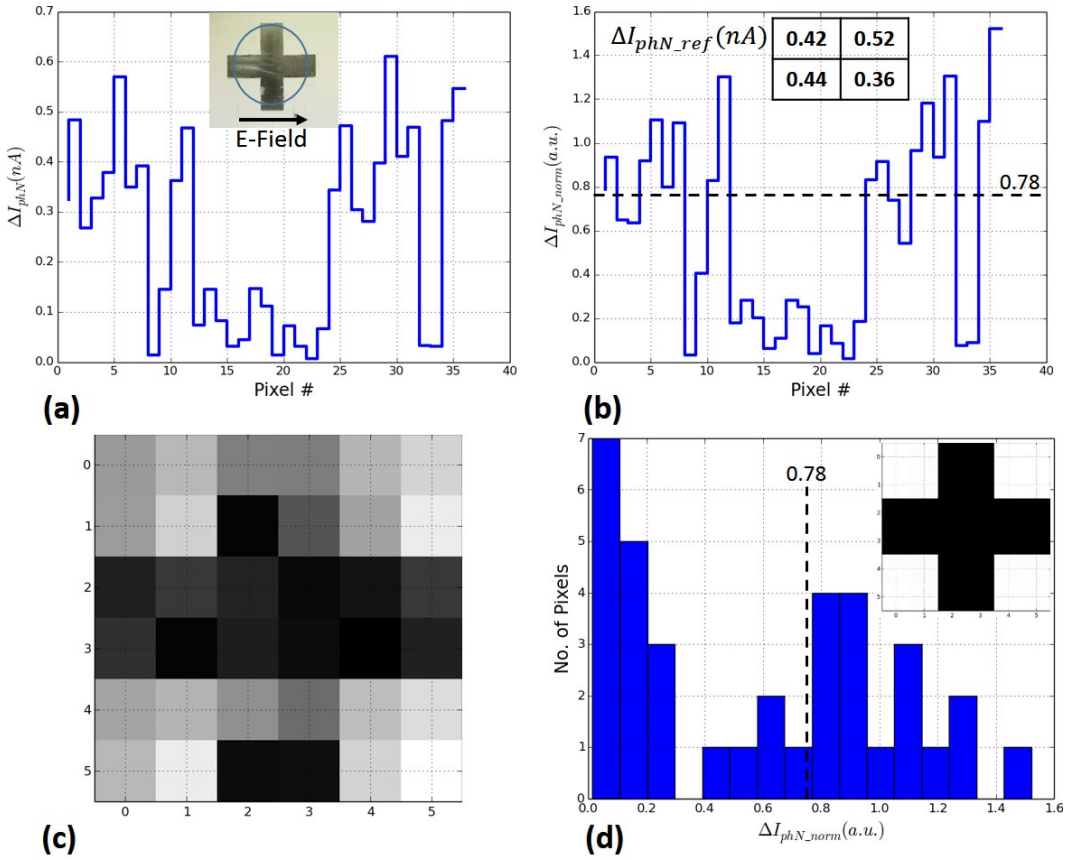

Figure 4-15: Single-pixel terahertz imaging. (a) Differential lock-in current (ΔI_{phN}) as each pixel is turned "on" and "off" for all 36 pixels. Inset of the scanned object: aluminum metal cross of width 15mm on a 3.5 mm thick polystyrene screen. The linearly polarized field of the THz transmitter is shown with respect to the object. (b) Normalized differential lock-in current (ΔI_{phN_norm}) where each pixel is normalized to it's reference differential lock-in current ΔI_{phN_ref}. Inset shows ΔI_{phN_ref} for each of the four pixels. (c) ΔI_{phN_norm} is displayed as 6x6 gray scale image with a physical resolution of 7.5 mm. (d) Histogram of ΔI_{phN_norm}. 20 pixels (object) with $\Delta I_{phN_norm} < 0.78$ shown with the vertical dashed line. Inset: A binary image is created using the histogram data with a threshold value of $\Delta I_{phN_norm} = 0.78$.

Our single pixel imaging experiments were performed using the experimen-

tal setup described in the methods section (Fig.4-13). Fig-4-15(a) displays the differential lock-in current ΔI_{phN} for each pixel that can be expressed as $\Delta I_{phN} = I_{phN_OFF} - I_{phN_ON}$ where, $I_{phN_ON} = I_{phN}(V_{GS} = -1V)$ and $I_{phN_OFF} = I_{phN}(V_{GS} = 0V)$ for the N^{th} pixel. For each measurement, the frequency was scanned from 450.025 GHz to 450.25 GHz and the peak-to-peak value of the lock-in current was recorded. This was done to remove any phase information in the measurement. The inset in Fig-4-15(a) shows the 15mm wide aluminum cross placed on a 3.5 mm thick polystyrene screen which is almost transparent at 0.45 THz but opaque to visible light. And the polarization direction of the incident electric field is also shown in the inset. Due to imperfection in our SLM assembly, the reference differential lock-in current for each of the SLM pixel is different. The reference differential current can be defined as $\Delta I_{phN_ref} = I_{phN_ref}(V_{GS} = 0V) - I_{phN_ref}(V_{GS} = -1V)$ where the lock-in current is measured with only the polystyrene screen without the metal cross. Because of the difference in the reference current, differential lock-in current in Fig-4-15(a) is normalized with respect to ΔI_{phN_ref} for each of the corresponding SLM pixel. The normalized differential current is plotted in Fig-4-15(b) which can be expressed as $\Delta I_{phN_norm} = (I_{phN_OFF} - I_{phN_ON})/\Delta I_{phN_ref}$. The inset in Fig-4-15(b) shows the ΔI_{phN_ref} for each of the four pixels in the SLM. Note, the maximum value of the normalized differential current is greater than one due to drifts in measurements from one scan to scan to another, a source of noise as well.

In order to get a spatial view of the normalized differential current ΔI_{phN_norm}, it is displayed as a gray scale image in Fig-4-15(c). The low fidelity in the image quality is primarily due to the noise in the system. As mentioned in the previous section, the SLM and the detector are placed closer to the focal point for measurable signal-to-noise ratio (SNR) at the expense of lower resolution further lowering the fidelity of the image. One way to remove the noise in bi-modal distributed pixels is to create a binary image based on a threshold that is mid way between the two modes of distribution. The histogram of

ΔI_{phN_norm} is shown in Fig-4-15(c). Since the two distributions (for the object and the polystyrene screen) are very close to each other due to higher noise in the system, the threshold was chosen based on the a priori knowledge of the object.

Since the object (aluminum cross) should be composed of 20 pixels, the threshold was chosen at the 20^{th} "darkest" pixel, $\Delta I_{phN_norm} = 0.78$. Based on this threshold value, a binary image was created as shown in inset of Fig-4-15(d). From the binary image, it can be seen that the aluminum cross placed behind the thick polystyrene screen, which is opaque for visible light, is identified using our single pixel THz imaging setup, demonstrating the viability for security screening, one of many potential applications of THz imaging.

4.6 Summary

In conclusion, we have implemented a terahertz (0.45 THz) spatial light modulator (SLM) based on active metamaterial with embedded HEMT device in a low-cost consumer-grade GaAs process. Our first generation design, a 2x2 pixel array, demonstrates spatial modulation at very low-voltage (1V) consuming very low power ($< 1mW$), making it the first solid-state THz SLM that is integrable on a system-on-chip (SoC).

It is also the first to operate at switching voltage of 1 V, the lowest reported to-date is 14 V[158]. Unlike current solid-state THz SLMs, the embedded HEMT device in every split-gap allows very high speed operation[101]($\sim$ 10 MHz), even GHz operation if designed appropriately. We would like to emphasize that since the imaging is effectively done at a single frequency, a commercial THz imaging system can be designed with a more sensitive single-pixel detector and cheaper source, such as a schottky diode and diode multipliers, which will be much lower power and cost compared to the cw THz spectrometer used in this work.

For being able to design in a mature commercial process will allow fu-

ture implementation to include complex circuitry in the same die for control and image processing. Our transmissive design also allows for simpler optics compared to reflective SLMs. Designing THz SLMs using metamaterial offers numerous advantages such as hyper-spectral imaging by creating pixels with multiple resonance frequencies and polarization sensitive SLMs.

After successfully demonstrating the modulator as a THz SLM, the next step is to design a multi-pixel array in a single die with high-speed control embedded on chip to facilitate faster modulation rate. One of the key nature of the metamaterial is it's narrow band nature. A multi-pixel SLM with multi-resonant metamaterial element will be most desired for hyper-spectral imaging.

As mentioned previously, one of the drawbacks of single-pixel imaging is it's serial nature of scanning the image. In most of the earlier compressed imaging works, the coded masks were all intensity masks with (0, 1) elements because the mechanical masks. With metamaterial based SLMs we have the ability to control the modulation depth and phase as well, adding a whole new dimension to compressed imaging. Effect of signal-to-noise ratio (SNR) and acquisition rate based on coded masks that have real values instead of just (0, $\pm$1), may break the logjam in single-pixel imaging and become a real mainstream THz imaging contender. Recent single-pixel imaging work reported in [190] and [189] show promise in that direction.

Chapter 5

A Wireless Multi-level Terahertz Amplitude Modulator using Active Metamaterial-based Spatial Light Modulation

5.1 Introduction

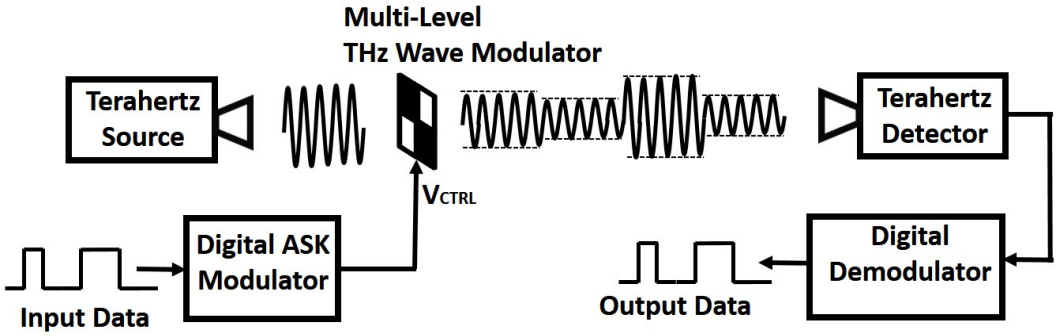

Figure 5-1: Block diagram of a terahertz wireless communication system using multi-level amplitude shift keying (ASK) modulation

The demand for high speed wireless access is increasing due to large amounts of data needed for new emerging applications such as the consumer market that is already demanding 20, 40 and 100 Gbit/s wireless technologies for Super Hi-Vision (SHV) and Ultra High-Def (UHD) TV data[23]. Terahertz (THz) carrier frequencies will offer the advantage of higher data speed, sub-millimeter antenna size and short range security especially suitable for portable devices. Although they are susceptible to atmospheric loss, THz digital communication systems have been demonstrated near certain windows, especially around the 300-400 GHz range that has shown promise for high bit-rate data transmission [23–25]. In addition to THz sources and detectors, one of the key components of a THz communication system is a modulator that is used to modulate the carrier waves with data streams. Designing high-speed modulators for the frequency regime (0.3 - 10 THz, $\lambda = 1mm - 30\mu m$), so called 'terahertz gap'[2], has been a difficult primarily due to lack of suitable materials for constructing electronic or quasi-optical devices. In recent years, the research in metamaterial[194] has slowly narrowed this gap by showing promise in applications ranging from bio-detection to security screening [17–20]. But most metamaterial based terahertz modulators have been limited to high voltage and low speed devices[84, 88] that makes it unsuitable for the applications that are demanding high-speed and low-voltage operations. We use a metamaterial based THz modulator with embedded HEMT that has been demonstrated to operate at high speed ($\sim 10MHz$) and operating at as low as 1V makes it suitable for high-speed and low-power communication systems[101]. With a crowded RF spectrum, high data rate and spectral efficiency are top priority in wireless communication systems[195]. The next step towards that goal is to create spectral efficient multi-level amplitude shift keying (ASK) modulators for terahertz frequencies. A simple block diagram of a terahertz communication system based on multi-level ASK is shown in Fig. 5-1. In this system, voltage controlled terahertz modulators [84, 101] can be used for multi-level terahertz modulation by applying different control

voltages for their respective transmit symbols. In addition to poor terahertz sources and detectors, noisy modulator electronics result in low SNR which inherently limits the number of levels for amplitude modulation.

In this work, we present a novel modulation technique that breaks this barrier from low SNR by using a spatial light modulator consisting of electronically controlled metamaterial tiles in array, where each tile is controlled by an equivalent binary signal, 'high' or 'low', and the multi-level ASK modulation is effectively and indirectly achieved by choosing the number of tiles based on the transmit symbol. In principle, this converts a multi-level voltage domain to multi-element spatial domain making it immune to voltage noise in the transmit control circuitry since there is no such thing as 'spatial noise'. This results in a higher spectrally efficient terahertz modulator since you can transmit more symbols for a given voltage noise in the transmit circuitry when using a spatial light modulation compared to voltage controlled modulation. The idea is extensible to visible light communication and RF communication as well. Using an active metamaterial based terahertz modulator, we demonstrate two orders of magnitude improvement in symbol error rate (SER) for 20 dB degradation in signal-to-noise ratio (SNR) in the transmit circuitry. In the next section we detail the principle behind the terahertz modulator and it's design fabrication techniques. We then show the terahertz characterization result for both voltage and spatial modulation. Finally, from the characterization results we develop a terahertz communication model and compare the SER from analysis and simulation for both the modulation schemes.

5.2 Results

5.2.1 Device Design and Experimental Setup

In order to demonstrate our modulation technique, we characterized a metamaterial based modulator at terahertz (THz) frequencies (0.45 THz) using

continuous wave terahertz spectroscopy. The metamaterial is based on a electric-LC (ELC) resonator as shown in Fig. 4-8(a,b) and explained in detail in section 4.2. The modulator is assembled as 2x2 tile device as shown in Fig. 4-8(c) that is characterized both as spatial light modulator and voltage controlled modulator. For voltage control mode, the gate-to-source voltage (V_{GS}) of all the four tiles are modulated simultaneously.

The continuous-wave terahertz spectroscopy setup to characterize the THz modulator is shown in Fig. 4-13 and detailed in section 4.4 except, the object is removed from the collimated path. This setup was used to characterize both the voltage and spatial modulation and the measured data is used to model the THz communication system described in a later section.

5.2.2 Voltage Modulation Characterization

We characterized the voltage controlled modulation and spatial modulation in a transmission geometry using the experimental apparatus shown in Fig. 4.4. The transmission spectra for each modulation configuration is result of a frequency scan from 447 GHz to 455 GHz with a step size of 0.005 GHz and lock-in time-constant of 620 ms. For voltage controlled modulation, the gate-to-source voltage (V_{GS}) of all the embedded HEMTs was swept from 0V to -1V with a step size -0.125V and the transmission spectra for each V_{GS} ($I_{ph,V_{GS0}}(f) = I_{ph}(f)[V_{GS0}]$) was measured as shown in Fig. 5-2(a). In order to emphasize the modulation depth near the modulation frequency, the differential transmission spectra for each V_{GS} ($\Delta I_{ph,V_{GS0}}(f)$) was calculated using the data from Fig. 5-2(a) as shown in Fig. 5-2(b) which can be expressed as $\Delta I_{ph,V_{GS0}}(f) = I_{ph,V_{GS0}}(f) - I_{ph_ref}(f)$ where, $I_{ph_ref}(f) = I_{ph,0V}(f)$ i.e. the transmission spectra when all the metamaterial is "off". A total of 36% modulation is observed at 450.2 GHz. In order to demonstrate the 4-level ASK THz communication system, V_{GS} values were calculated for equal discrete steps of $|\Delta I_{ph}| \approx 0.4nA$ using the function $\Delta I_{ph}(V_{GS})$ as shown in Fig. 5-2(c). $\Delta I_{ph}(V_{GS})$ is expressed by fitting data points of $I_{ph,V_{GS0}}(f_0)$ at 450.2 GHz in

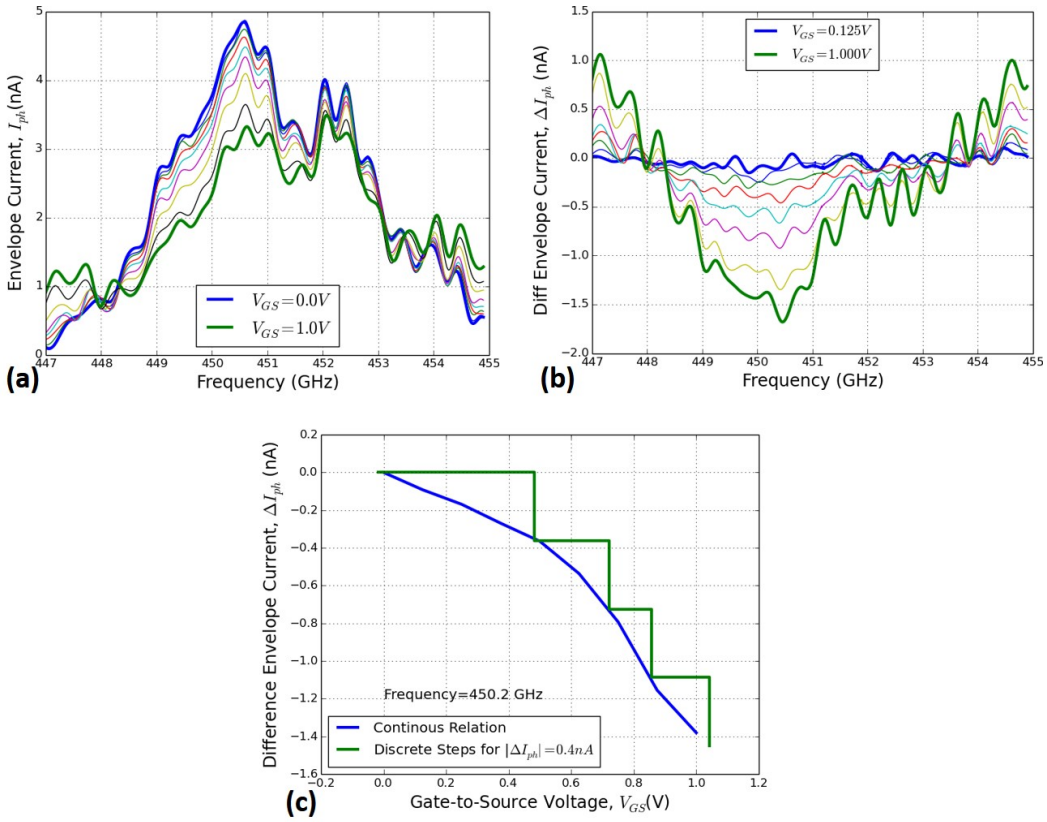

Figure 5-2: Characterization of the metamaterial for voltage controlled modulation. (a) Family of transmission spectra from 447-455 GHz using the envelope of the detected photocurrent $I_{ph,V_{GS0}}(f)$, as the gate-to-source voltage (V_{GS}) of all the embedded HEMTS is varied from 0V to -1V in steps of $-0.25V$. (b) Family of differential transmission spectra ($\Delta I_{ph,V_{GS0}}(f)$) for V_{GS} swept from -0.125V to -1V with respect to the reference spectra of maximum transmission i.e. all the metamaterials are "off" ($I_{ph,0V}(f)$). (c) From the envelope photocurrent of the differential transmission spectra at 450.2 GHz in (b), a continuous relation between V_{GS} and ΔI_{ph} is extracted using a 3^{rd}-order polynomial. Using this relation, V_{GS} values are derived for discrete steps of $|\Delta I_{ph}| \approx 0.4nA$. These V_{GS} values are used to simulate the 4-level ASK digital communication system.

Fig. 5-2(b) using a $3^{rd} - order$ polynomial fitting function. This enables us to achieve uniform spacing of modulated THz wave in spite of the inherent nonlinearity in our modulator. Let $\Phi_I(V)$ denote the function $\Delta I_{ph}(V_{GS})$ that can be expressed as

$$\Phi_I(V) = -0.02 - 0.41V - 0.4V^2 - 0.6V^3 \tag{5.1}$$

5.2.3 Spatial Modulation Characterization

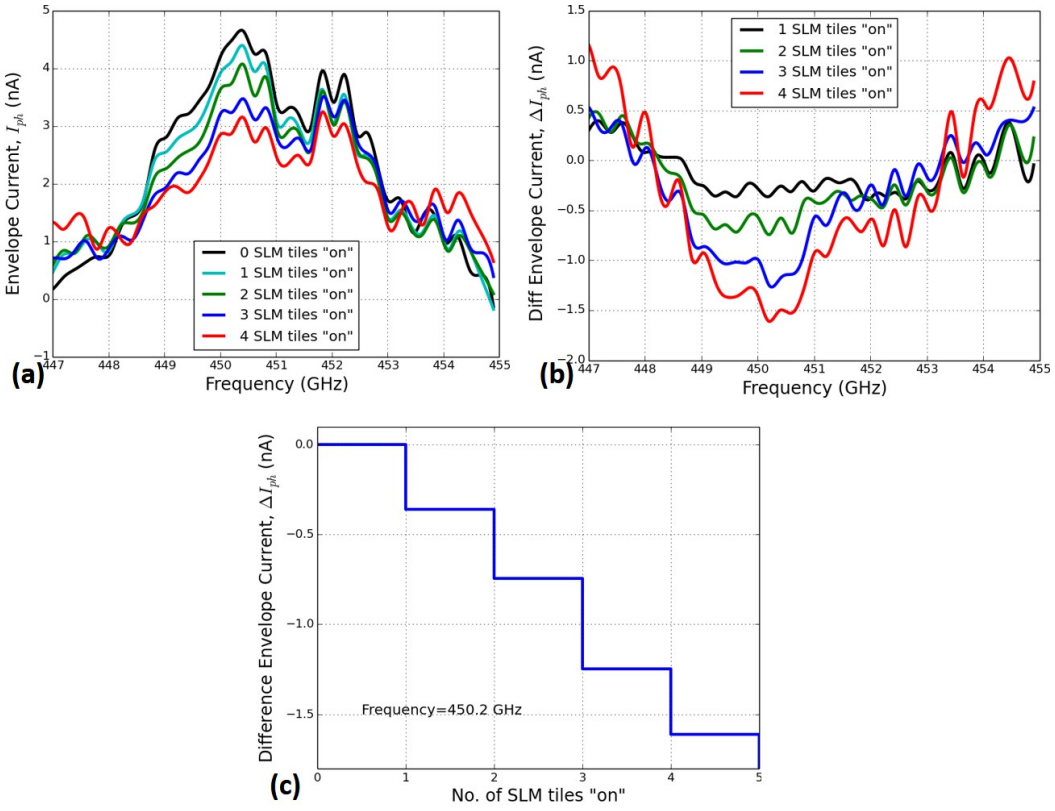

Figure 5-3: Characterization of the 4-tile (2x2) SLM. (a) Family of transmission spectra from 447-455 GHz using the envelope of the detected photocurrent, $I_{phN}(f)$, as the elements are turned "on" and "off" sequentially in clockwise and anti-clockwise direction. (b) Family of the differential transmission spectra ($\Delta I_{phN}(f)$) with reference spectra, $I_{ph0}(f)$, i.e. the condition for maximum transmission when all the metamaterials are "off" ($I_{ph0}(f) = I_{ph}[V_{GS} = 0V$ for all elements]). (c) From the envelope photocurrent of the differential transmission spectra at 450.2 GHz in (b), $\Delta I_{phN}(f_0)$ is plotted as function of number of spatial elements "on". These ΔI_{phN} are used in the system simulation model.

For characterizing spatial modulation, each of the four spatial tiles were turned "on"($V_{GS} = -1V$) and "off"($V_{GS} = 0V$) sequentially in a clockwise or anti-clockwise direction while the transmission spectra using the envelope of the detected current was measured as shown in Fig. 5-3(a). As in the case of voltage modulation, in order to emphasize the modulation depth near the resonant frequency, the differential transmission spectra for each incremental element ($\Delta I_{phN}(f)$) was calculated using the data from Fig. 5-3(a) as shown in Fig. 5-3(b) which can be expressed as $\Delta I_{phN}(f) = I_{phN}(f) - I_{phN_ref}(f)$ where, $I_{phN_ref}(f) = I_{ph,0V}(f)$ i.e. the transmission spectra when all the elements are "off". A total of 36% modulation is observed at 450.2 GHz with an average of 9% modulation for each element. Fig. 5-3(c) shows the envelope photocurrent of the differential transmission spectra at 450.2 GHz in Fig. 5-3(b), $\Delta I_{phN}(f_0)$ is plotted as function of number of spatial elements "on". As evident from these plots, binary switching the tiles on and off has an equivalent effect of modulating the terahertz wave. These ΔI_{phN} values are used in the system simulation model where we lay the foundation for multi-level THz amplitude modulation using effective spatial light modulation.

5.2.4 Analysis and Simulation of symbol error rate for a multilevel amplitude modulation THz communication system

An important performance metric almost universally used for a digital communication system that is corrupted by noise, is the probability of error in the output signal commonly measured as bit error rate (BER) for a binary signaling system. For a multilevel signaling system like ours, the same metric is measured as symbol error rate (SER). For a binary signaling system (voltage levels $\pm V_P$) with zero mean additive white Gaussian noise (AWGN) and mid-point threshold for signal detection, the BER ($\mathbf{P}(error) = \mathbf{P}_e$) can be

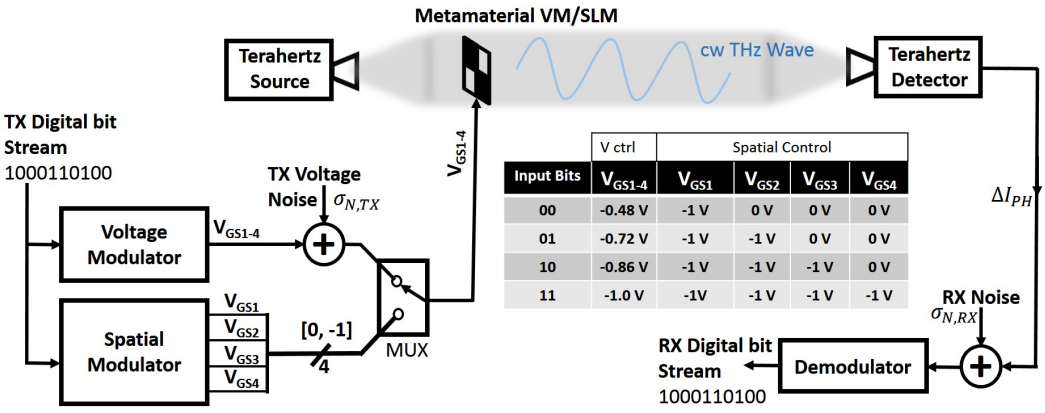

	V ctrl	Spatial Control			
Input Bits	V_{GS1-4}	V_{GS1}	V_{GS2}	V_{GS3}	V_{GS4}
00	-0.48 V	-1 V	0 V	0 V	0 V
01	-0.72 V	-1 V	-1 V	0 V	0 V
10	-0.86 V	-1 V	-1 V	-1 V	0 V
11	-1.0 V	-1V	-1 V	-1 V	-1 V

Figure 5-4: System model for analysis and simulation of symbol error rate (SER) for a multilevel amplitude modulation THz communication system. The Voltage Modulator maps 2-bits from the input bit stream to a gate-to-source voltage (V_{GS}) for the terahertz modulator based on the inset table that is derived from the characterization data in Fig. 5-2. Similarly, the spatial light modulator maps 2-bits from the input bit stream to a spatial map for the terahertz modulator based on the inset table that is derived from the characterization data in Fig. 5-3. Transmit voltage noise ($\sigma_{N,TX}$) represents the accumulative electronic noise in the transmit circuitry referred at the output of the Voltage Modulator. Receive noise ($\sigma_{N,RX}$) represents the accumulative noise in the terahertz channel and the electronic noise in the demodulator referred at the input of the demodulator. Both the noise sources are modeled as Additive White Gaussian Noise (AWGN).

expressed as[196]

$$BER = \mathbf{P}_e = \frac{1}{2} erfc\left(\frac{V_P}{\sigma_0\sqrt{2}}\right) \tag{5.2}$$

where, $erfc(z) \equiv 2/\sqrt{\pi}\int_z^\infty \exp(-\lambda^2)d\lambda$ and σ_0^2 is the variance of the AWGN.

The system model used for our analysis and simulation of symbol error rate (SER) is shown in Fig. 5-4. For the purpose of demonstration, a 2x2 spatial light modulator was characterized (Fig. 5-3) and is modeled in this system as a 4-level terahertz amplitude modulator that can transmit 2-bit ($\log_2(4)$) symbols. In order to create a platform for comparison, the voltage modulator was characterized (Fig. 5-2) and 4-level modulation model was extracted from it which is also implemented in the system as shown in Fig. 5-4.

For voltage modulation, the bit stream is converted to 2-bit symbols that is a gate-to-source voltage (V_{GS}) chosen from 4 values within the range (0,-1V) as shown in the inset table in Fig. 5-4. *Additive white Gaussian noise (AWGN)* is added to this V_{GS} symbol ($\sigma_{N,TX}$ in Fig. 5-4) and applied to the terahertz modulator model which represents all the electronic noise referred at the output of the V_{GS} control circuitry. The output of the terahertz modulator model is a differential photocurrent (ΔI_{Ph}) based on the $V_{GS} - \Delta I_{Ph}$ relation derived from voltage modulation characterization as shown in Fig. 5-2(c). Noise (AWGN) is added to this detected differential photocurrent ($\sigma_{N,RX}$ in Fig. 5-4) which represents noise in the terahertz channel and the electronic noise in the demodulator referred at the input of the demodulator. The resultant differential photocurrent is demodulated using corresponding thresholds to slice the input into one of the four symbols and the transmitted bit stream is reproduced from it.

For spatial modulation, the bit stream is also converted to 2-bit symbols that represents the number of spatial tiles that are "on" based on the inset table in Fig. 5-4. Since this mapping from bit stream to the spatial modulation inherently remains binary in nature, the voltage noise in the transmit circuitry does not affect the noise performance of the spatial modulation system.

SNR	Voltage Modulation		Spatial Modulation	
(dB)	(Sim SER)	(Calc. SER)	(Sim SER)	(Calc. SER)
-3.4	0.284	0.252	5.2e-05	3.16e-05
0.8	0.137	0.148	6e-05	3.16e-05
5.0	0.0463	0.0601	5.3e-05	3.16e-05
9.2	0.0139	0.0175	5.3e-05	3.16e-05
13.5	0.00519	0.00527	5.4e-05	3.16e-05
17.7	0.00284	0.00239	5.6e-05	3.16e-05
21.9	0.00205	0.00162	4.5e-05	3.16e-05
26.1	0.00181	0.00137	5.9e-05	3.16e-05
30.3	0.00168	0.00128	6.2e-05	3.16e-05
34.5	0.00161	0.00125	6.4e-05	3.16e-05

Table 5.1: Symbol error rate (SER) results from analysis and Monte Carlo simulation. Tabulated data of Fig. 5-5(a).

The rest of the model is exactly same as described in the voltage modulation system. The additive noise after the terahertz detector affects the spatial modulation the same way as the voltage modulation case.

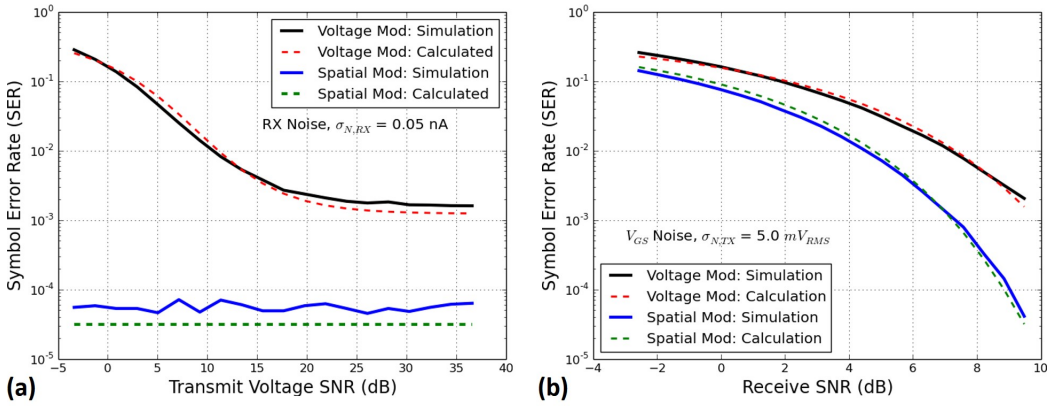

Figure 5-5: Symbol error rate (SER) simulation results. (a) The calculated and simulated SER for voltage and spatial light modulation as function of the transmit SNR (Data is tabulated in table 5.1). (b) The calculated and simulated SER for voltage and spatial light modulation as function of the receive SNR.

In order to demonstrate the noise advantage of spatial modulation over voltage modulation, we analyze the SER of the system for a zero mean AWGN and a variance of $\sigma^2_{N,TX}$ and $\sigma^2_{N,RX}$ for the transmit and receive noise respectively. Based on the same principle of derivation as for BER in Eq. (5.2), we

can express the symbol error rate (SER = $\mathbf{P}(error) = \mathbf{P}_e$) of our system as

$$SER = \mathbf{P}_e \simeq \frac{1}{2} erfc \left(\frac{\gamma \frac{1}{K} \sum_{k=1}^{K} |\Phi_I(V_{GSk}) - \Delta I_{phk,th}|}{\sqrt{2(\Phi_I^2(\sigma_{N,TX}) + \sigma_{N,RX}^2)}} \right) \tag{5.3}$$

where, $|\Phi_I(V_{GSk}) - \Delta I_{phk,th}|$ is the signal strength of the K^{th} symbol with respect it's threshold, $\Phi_I(V_{GSk})$ expresses K^{th} the symbol voltage referred at the input of the demodulator using the function $\Phi_I(V)$ in Eqn. 5.1 with reference to their corresponding threshold current ($\Delta I_{phk,th}$) that is used to slice a received signal for detecting the transmitted symbol. Similarly, the transmit voltage noise is referred at the input of the demodulator using the function in Eqn. 5.1 as $\Phi_I^2(\sigma_{N,TX})$ which is added to the receive noise power $\sigma_{N,RX}^2$ to account for the total noise power in the system. γ is the fitting co-efficient to account for the non-linear function $\Phi_I(V)$ and the unequal magnitude of the V_{GSk} symbols.

In order to verify our analysis, the digital communication system was simulated using a common computer-aided technique know as the Monte Carlo method[197]. It is in essence a time-domain technique that sequentially simulates a deterministic or random bit-stream with added noise. If N symbols are processed through the system, out of which n are observed to be in error, the SER can be expressed as the sample mean: $\hat{p} = n/N$. In the limit $N \to \infty$ the estimate $\hat{p}$ will converge to the true value p. For finite N, it has been shown that N should be in the order of $10/\mathbf{P}_e$[197]. We simulated with $N = 10^6$ bits for a high certainty SER output from our simulation. The simulation was done for each value of the signal-to-noise ratio (SNR) for both the voltage and spatial modulation.

Fig. 5-5(a) shows the calculated and simulated SER for voltage and spatial modulation as function of the transmit SNR which can be expressed as $\langle V_{GSk} - V_{GSk,th} \rangle / \sqrt{2}\sigma_{N,TX}$ where, the numerator is average of the V_{GS} symbols with reference to the their corresponding thresholds and the denominator is standard deviation of the added transmit noise. The plots show a good match

of the simulated SER with the calculated values, for $\gamma = 0.75$. It can be clearly observed from the voltage modulation plot, the SER increases by almost two orders of magnitude with a 20 dB decrease in SNR, where as the SER for the spatial light modulation remains unchanged. This confirms our design objective which is predicted by our analysis that spatial light modulation provides immunity to voltage noise in the transmit electronics compared to voltage controlled modulation. The SER for voltage modulation is asymptotic at $\approx 10^{-3}$ due to the constant receive noise of $\sigma_{N,RX} = 0.05$ nA. It is also observed that the SER of the spatial light modulation is better even at higher SNR due to higher modulation depth than the voltage modulation as seen in Fig. 5-2(c) and Fig. 5-3(c).

Fig. 5-5(b) shows the calculated and simulated SER for voltage and spatial light modulation as function of the receive SNR which can be expressed as $\langle \Phi_I(V_{GSk}) - \Delta I_{phk,th} \rangle / \sqrt{2}\sigma_{N,RX}$ where, the numerator is average of the receive symbols with reference to the their corresponding thresholds and the denominator is standard deviation of the added receive noise. The plots show a good match of the simulated SER with the calculated, for $\gamma = 1.0$. It can be observed that both modulation schemes have decreasing SER with decreasing SNR. This is expected from analysis as the added receive noise affects both the schemes equally. The spatial light modulation still shows better SER due to higher modulation depth than the voltage modulation as seen in Fig. 5-2(c) and Fig. 5-3(c).

5.3 Summary

In conclusion, we have demonstrated a terahertz communication system based on active metamaterial-based spatial light modulators that is immune to voltage noise in the transmit electronics compared to voltage controlled modulation. This enables multi-level amplitude modulation which otherwise would not have been possible due to low SNR. We show experimental results on both

voltage and spatial light modulation. And using models created from such experimental measurements, we show excellent immunity to transmit electronic noise as predicted by our analysis. Monte Carlo simulations confer with our analysis showing two orders of magnitude improvement in symbol error rate (SER) for 20 dB SNR degradation due to transmit voltage noise. The result of this work is a very important step towards realizing higher spectral efficient modulation technique eg. multi-level ASK, for high speed wireless terahertz digital communication systems.

Having computationally proven the noise fidelity advantage of spatial modulation, the next logical step is to experimentally demonstrate the concept in a THz wireless communication system.

Chapter 6

Pictorial Modulation for High-Speed Wireless Communication

In chapter 5 we showed the ever increasing demand for high speed wireless for handling large amounts of data for emerging applications [23] and how the terahertz regime, even with issues of loss and lack of devices, has shown promise for high bit-rate data transmission [23–25]. We also demonstrated in chapter 5 the advantage in higher spectral efficiency when modulating the terahertz wave spatially.

One of the challenges of THz communication is achieving high speed modulation. Our HEMT controlled metamaterial modulator [101], is still the highest speed solid-state modulator ($\sim$ 10 MHz) using standard semiconductor process and that's far from reaching the capacity of the carrier. In this chapter we introduce a spatial modulation technique, termed as *pictorial modulation*, which will improve the channel bandwidth by orders of magnitude depending on the signal-to-noise ratio (SNR) of the channel, compared to a standard spatial or voltage modulation as described in chapter 5.

6.1 Basic Principle of Pictorial Modulation

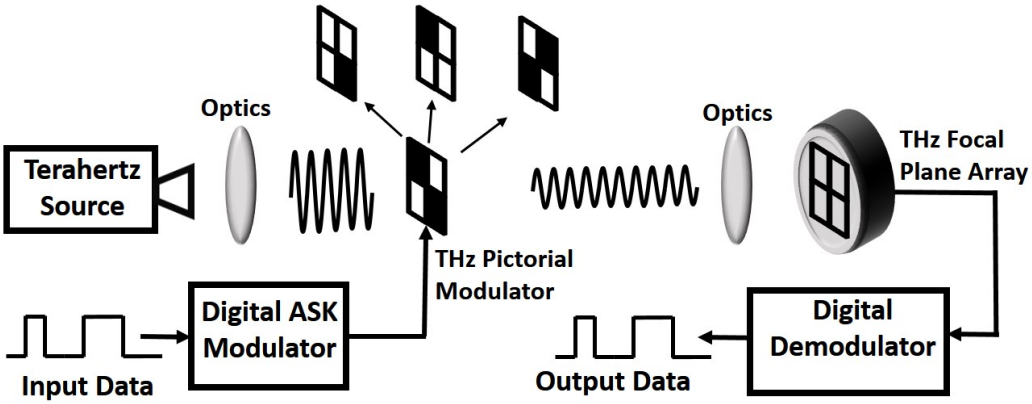

Figure 6-1: Schematic of a basic pictorial modulation setup. A terahertz source is collimated on to a spatial light modulator which modulates the THz wave as pictorial symbols created from the digital input data. This modulated wave is focused on to a THz focal plane array detector and the *picture* symbol is converted back to bit stream.

A basic schematic of a THz communication system based on pictorial modulation is shown in Fig. 6-1. The terahertz wave from a source is collimated with appropriate optics. A THz spatial light modulator is placed in the collimated path for pictorial modulation. A digital amplitude shift keying (ASK) modulator converts a input bit stream to it's equivalent pictorial symbol. Another set of optics focuses the modulated THz wave on to a THz focal plane array imager which decodes the pictorial symbol to it's equivalent bit stream.

In chapter 5, a single-pixel detector was used to detect the spatially modulated wave because of which you could only detect the aggregate power and no spatial information. By using a focal plane imager instead, we can pack more information in the channel since we can decode the spatial information as well.

An example is shown in Fig. 6-2 where, 16 pictorial symbols are created from a 2x2 spatial tile compares to only 4 symbols when using spatial modulation with a single-pixel detector, a 4X bandwidth improvement. Next we derive analytically the total number of symbols for an arbitrary N number of spatial tiles.

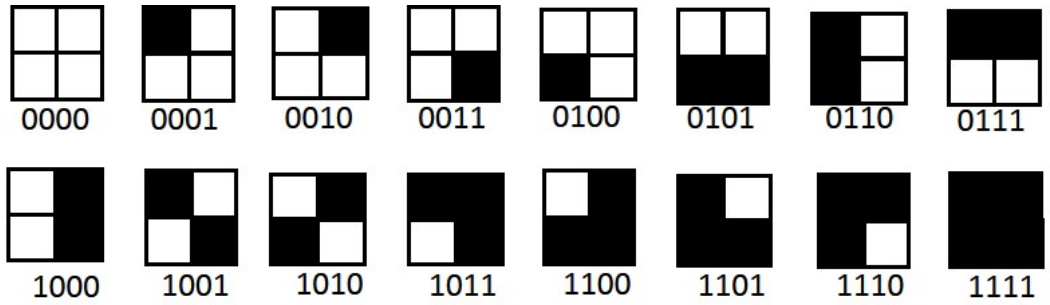

Figure 6-2: An example of pictorial symbols for a 2x2 spatial tile. A total of 16 symbols created for a 2x2 tile compared to only 4 symbols when using spatial modulation with a single-pixel detector, a 4X bandwidth improvement.

6.2 Bandwidth improvement for a N-tile Pictorial Modulator

From the previous example we noticed a 4X bandwidth improvement for a 4-tile(2x2) spatial modulator for pictorial modulation compared to standard spatial modulation. The general relation between the number of spatial tiles N and the number of symbols for pictorial modulation can be shown to be simple exercise in binary math.

Since there are only two possibilities for each tile, "on" or "off", the total number of symbols $\mathbf{S}$ for a N-tile spatial modulator is

$$\mathbf{S}_N = 2^N \tag{6.1}$$

For the example case in Fig. 6-2 where $N = 4$, it can be easily verified with Eqn. 6.1 that total number of symbols $\mathbf{S}_N = 16$. The bandwidth improvement over binary modulation is

$$kBW_{pic-bin}(N) = \log_2(\mathbf{S}_N) = N \tag{6.2}$$

Since the bandwidth improvement of standard SLM modulation w.r.t. binary modulation is $\log_2(N)$, the bandwidth improvement of pictorial modulation

over standard modulation is

$$kBW_{pic-slm}(N) = \frac{N}{\log_2(N)} \tag{6.3}$$

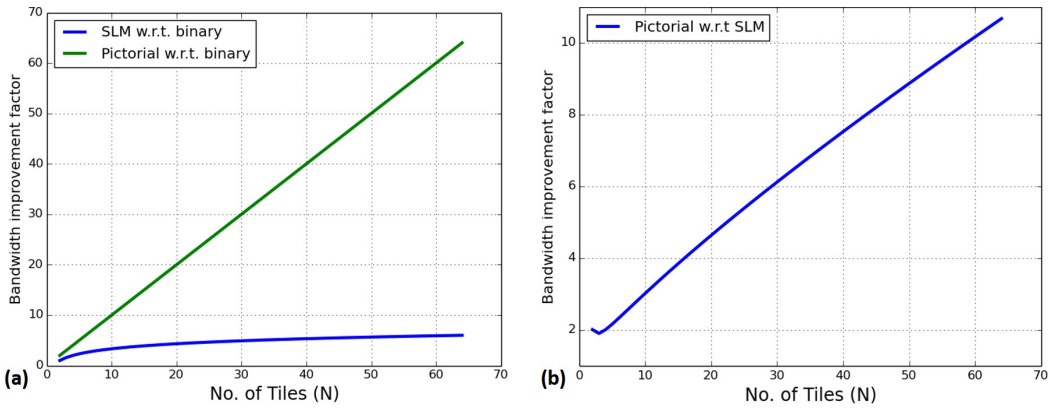

Figure 6-3: (a) Bandwidth improvement comparison of SLM and pictorial modulation over binary modulation. (b) The bandwidth improvement of pictorial modulation over standard spatial modulation.

The bandwidth improvement over binary modulation is plotted in Fig. 6-3(a) for pictorial and SLM modulation. It can be seen from the plots that the bandwidth improves linearly with the number of tiles for pictorial modulation whereas the improvement in SLM modulation is much slower since it is a logarithmic function.

The bandwidth improvement of pictorial modulation over SLM is plotted in Fig. 6-3(b) (Eqn. 6.3). For N=64, the improvement is better than 10X.

6.3 Symbol Error Rate Comparison with Standard Spatial Modulation

Given the significant bandwidth improvement over standard spatial modulation, we next look at symbol error rate (SER) for both modulation techniques with zero-mean additive white Gaussian noise (AWGN). The SER result for standard spatial modulation was shown both analytically and using Monte Carlo simulation in section 5.2.4.

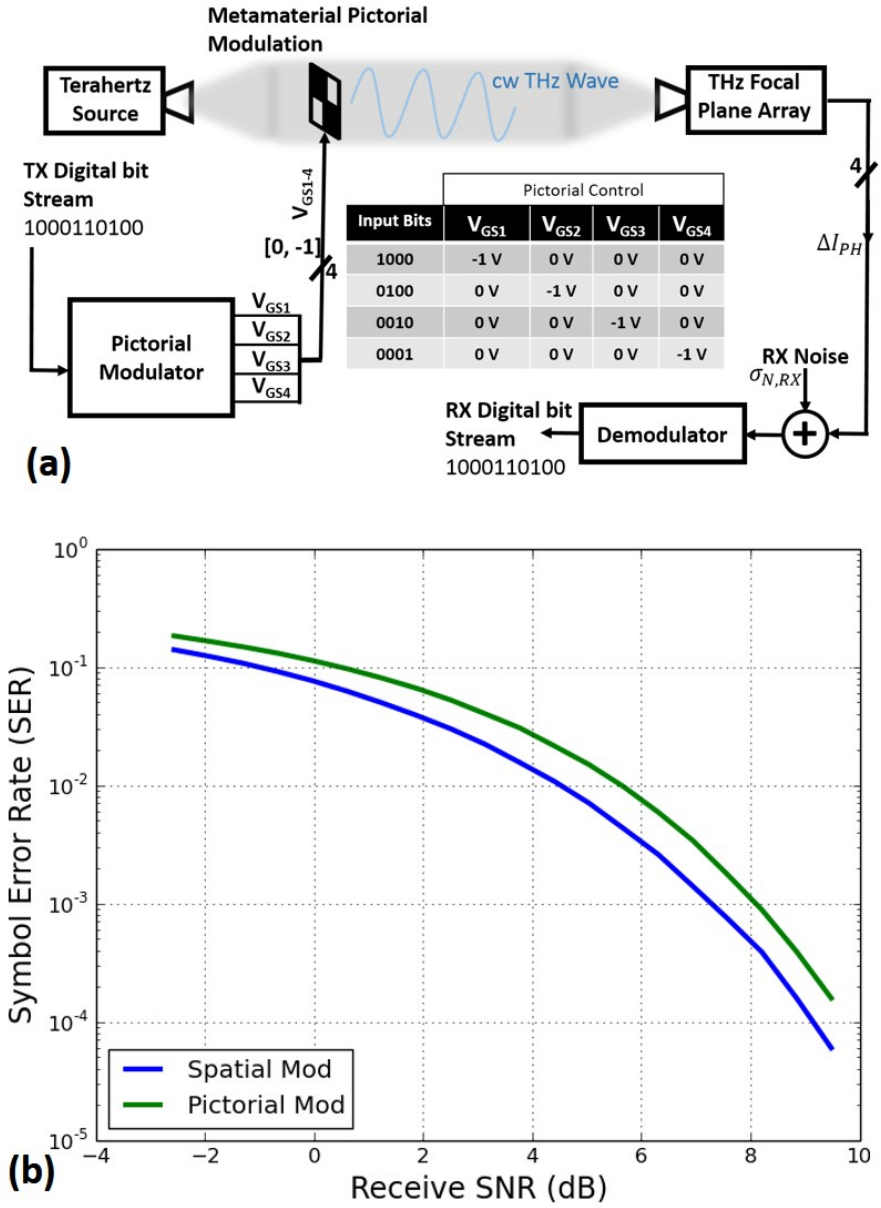

Figure 6-4: Symbol error rate comparison with standard spatial modulation.(a) The system model used for Monte Carlo simualation. (b) It can be seen from the plots that the effect of noise is similar in both types of modulation and therefore there is no noise disadvantage of pictorial modulation compared to standard spatial modulation.

We use Monte Carlo method to simulate the SER for pictorial modulation using a system model as shown in Fig. 6-4(a). For the purpose of comparison with spatial modulation, we use a 2x2 spatial light modulator using the THz characterization data from Fig.5-3. The simplest way to modulate the bit stream is to encode a group of four bits into a symbol where each of the bits controls one of the spatial tile in the 2x2 spatial modulator. 4 out of the 16 possible symbols are shown in the inset table in Fig. 6-4(a).

The output of the terahertz modulator model is a differential photocurrent (ΔI_{Ph}) based on the $V_{GS} - \Delta I_{Ph}$ relation derived from voltage modulation characterization as shown in Fig. 5-2(c). Noise (AWGN) is added to this detected differential photocurrent ($\sigma_{N,RX}$ in Fig. 6-4(a)) which represents noise in the terahertz channel and the electronic noise in the demodulator referred at the input of the demodulator. The resultant differential photocurrent is demodulated using a threshold for each spatial tile and creating the bit stream from it.

The simulated SER for pictorial and spatial modulation is shown in Fig. 6-4(b). It can be seen from the plots that both the modulation techniques have the same SER for a given signal-to-noise ratio (SNR) in the receive path.

6.4 Summary

We have demonstrated a novel modulation technique using an array of THz spatial modulators that modulates the THz wave pictorially and the modulated wave is demodulated using a THz focal plane array. The improvement in bandwidth over a N-tile array using spatial modulation with a single-pixel detector is shown to be a factor of $N/\log_2(N)$. For example, for a 64-tile array, the improvement is more than 10X. It is also shown through Monte Carlo simulations that there is no degradation in noise performance compared to spatial modulation with single-pixel detector. This is an important step towards high speed THz communication.

Having computationally demonstrated this novel modulation technique, the next step is to experimentally demonstrate the modulation technique in THz wireless communication system. One of the key element in this experimental setup is a THz focal plane array (FPA) and the THz FPA described in the next chapter, when available, will be a significant contribution to THz wireless systems.

Chapter 7

A Terahertz Metamaterial Detector Focal Plane Array using CMOS Process

As mentioned in chapter 4, there has been a significant interest in terahertz (THz) imaging because of it's potential for wide range of applications [17–20]. Due to the difficulty in building THz focal-plane-array (FPA) detectors, a single-pixel imaging method was demonstrated in chapter 4. Although compressed sensing (CS) [126, 178] techniques can be employed to speed up the frame rate, it is still a slow process due to calorimetric detection that are thermal-time-constant limited. Moreover, incoherent THz power detectors have primarily relied on specialized process technologies for the fabrication of Schottky diodes [198], or bolometers [199], making it difficult to mass produce them at lower manufacturing cost.

Complementary metal-oxide semiconductor (CMOS) process technologies are still the choice for low cost high volume applications. They also provide the option to build highly integrable supporting circuits that allow complex electronics systems to be build on the same substrate as the sensor. Therefore it is a natural desire to implement terahertz technologies in CMOS to commercialize this emerging technology and make it available to the masses. But

THz detection using CMOS has been limited to below 300 GHz due to lack of suitable low-noise amplifiers [200]. BiCMOS technologies have been developed with integration of silicon Schottky diodes with cut-off frequencies higher than 1 THz [198, 201].

Visible light digital cameras have been implemented in conventional CMOS process technologies with excellent performance [202], resulting in a massive commercialization of such cameras with 5+ Mega-pixel cameras as a standard feature even in low-cost mobile phones. However, long wavelength terahertz EM waves lack the energy for band-gap transition in CMOS technologies. Power detectors using field-effect transistors (FETs) as square law devices, has been used for many years [203, 204], but have been limited to lower microwave frequencies because of low electron mobility and channel resistance, especially in CMOS technologies. In recent years, FETs have been used as terahertz detectors [205, 206], explained as non-resonant response to plasma-wave excitation of a 2D electron gas [174], but their room temperature sensitivity is still questionable for commercial application.

The first fully integrated CMOS focal plane array operating at 600 GHz was demonstrated using the principle of distributive resistive self-mixing [207, 208]. This principle allows FET power detection of frequencies well above the device cutoff frequency (f_T). The authors demonstrated the principle by implementing a 3x5 pixel CMOS FPA in a 0.25 μm NMOS technology using an on-chip patch antenna as broadband receive antenna for each pixel.

In this work, we use the same principle to detect THz waves and create a FPA using metamaterials as the receive antenna. The use of metamaterials allows for frequency selective pixels and since the unit cells are sub-wavelength in size, multiple resonant frequency metamaterials can be packed into each pixel allowing for pseudo-color THz imaging providing spectral information of the imaged objects.

7.1 A 0.18 um CMOS Foundry Process Technology

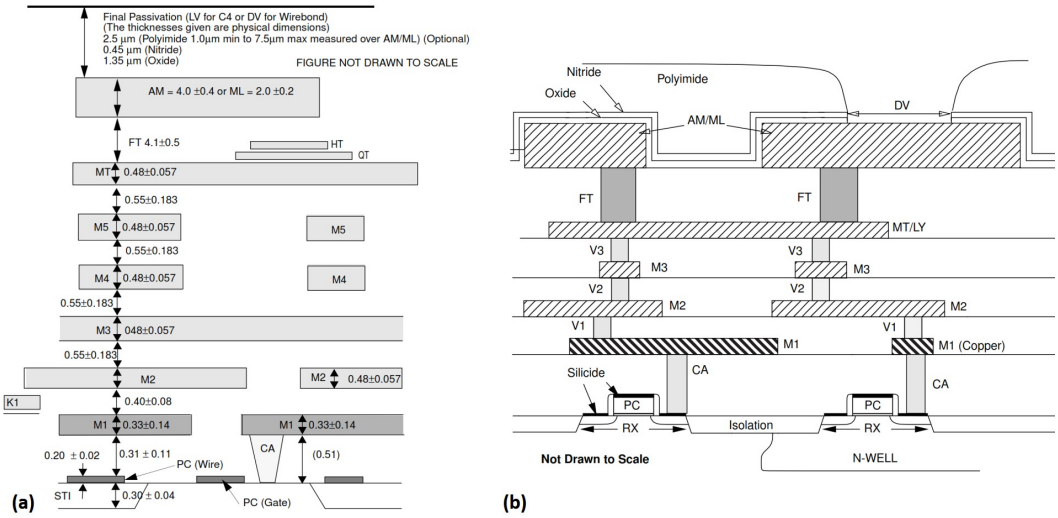

Figure 7-1: (a) Conductive film and inter-layer dielectric thickness for the used 0.18 μm CMOS foundry process. Please note, Metal-5 was not used in our option for fabrication. (b) Cross section view of the layers with FET

The decision to use a certain CMOS technology is primarily related to performance and cost. The newer and finer technologies offer significant performance advantage at higher cost. We decided to design our FPA in the range of 230-360 GHz for it is a good range of frequencies for THz imaging. Since THz detection at 650 GHz had been demonstrated with 0.25 μm CMOS technology using distributive self-mixing principle [208], we decided to use a 0.18 μm CMOS foundry process which is a very low cost process due to it's age and maturity.

The conductive layer and inter-layer dielectric thickness are shown in Fig. 7-1(a) for our chosen technology. It has 6 Metal layers for connectivity with metal-1 as copper and aluminum for the rest of the layers. Please note, there is no metal-5 for our chosen option of the technology. The top metal layer is a 2 μm thick layer which is used to design our metamaterials for smaller loss and it's the first layer after the passivation. Fig. 7-1(b) shows the cross

Material	Unit	Value
$p-Si$ substrate conductivity	S/m	7.41
$p-Si$ substrate relative permitivity		11.9
$Si0_2$ Conductivity	S/m	0.00
$Si0_2$ relative permitivity		4.10
$Si0_2$ Dielectric loss tangent		0.00-0.001
Polymide relative permitivity		3.4
Polymide loss tangent		0.00-0.001
All dielectrics relative permeability		1.00

Table 7.1: Properties of the CMOS materials used for electromagnetic simulations.

section of the FET devices along with the metal layers. At the very bottom is a 500 μm thick p-type silicon substrate which is opaque to the terahertz frequencies of operation. Therefore, this technology cannot be used for any terahertz transmissive designs.

NFETs are formed in the p-type substrate within a p-well. For isolating active devices, shallow trench isolation (STI) is used everywhere except the active areas (RX in Fig. 7-1(b)). This process has six flavors of NFETs. For the terahertz detection we use a minimum length and width standard NFET device. The standard NFET device operates at 1.8V, has an effective gate thickness of 3.5 nm ($C_{ox} = 7.9\ fF/\mu m^2$), minimum drawn length of 0.18 μm, threshold voltage $V_{th} = 355\ mV$ and mobility $\mu_n \approx 400\ cm^2/V \cdot s$. Similarly, there are six flavors of PFETs as well and we use the standard PFETs for all our circuit design.

The electromagnetic properties of the CMOS materials for simulating the metamaterials is tabulated in Table 7.1. In a foundry process, all the vertical dimensions are fixed in a given process and design rules are set for minimum width and spacing for metal and active layers, among numerous other design rules. Most foundry process, including ours, use chemo-mechanical polishing (CMP) to flatten uneven oxide layer after each metal and oxide deposition. This is imposes design rules on having minimum density for each metal layers. In our process its about 27% for all the metal layers. This introduces challenges

in metamaterial designs since we cannot have empty areas underneath the metamaterials.

7.2 Principle of Resistive Self-mixing Detection

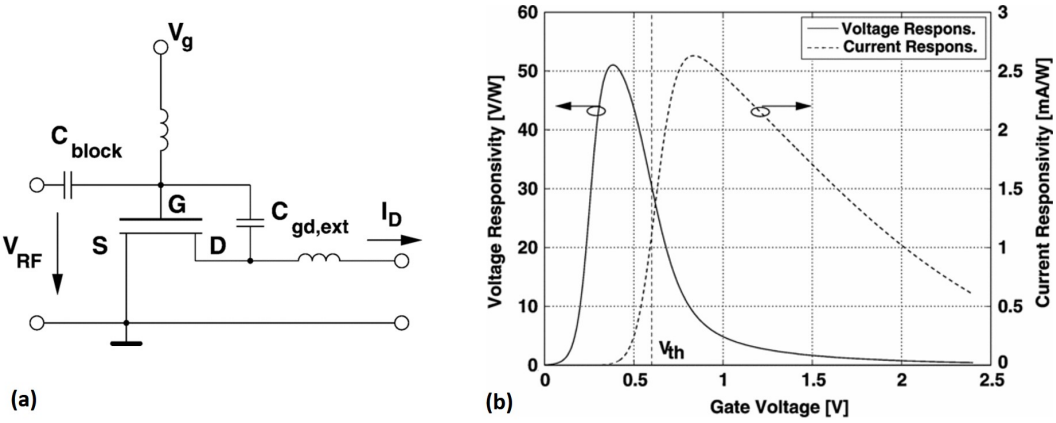

Figure 7-2: Quasi-static analysis of self-mixing. (a) FET resistive mixer configured for RF power detection (quasi-static self-mixing). (b) Simulation with the BSIM3 model of current mode (dashed line) and voltage mode (solid line) responsivity dependence on gate bias V_g. The threshold voltage V_{th} of the device is indicated with a dashed line. [208]

We first illustrate the low-frequency (quasi-static) analysis of a square-law power detection using a FET circuit shown in Fig. 7-2(a). Since our frequency of operation is beyond the cutoff frequency (f_T) of the FET, we follow with the non quasi-static (NQS) analysis that uses the distributed RC model of the FET.

The quasi-static configuration shown in Fig. 7-2(a) generates a DC current I_D proportional to the input RF power (V_{RF}^2) based on the following analysis. For a time-dependent input voltage $v_{RF}(t)$ the voltage at the drain is

$$v_{\rm gs}(t) = v_{\rm RF}(t) + V_{\rm g} \tag{7.1}$$

and due the large coupling capacitor $C_{gd,ext}$, the drain-to-source voltage v_{ds}

is

$$v_{\mathrm{ds}} = v_{\mathrm{RF}}(t) \tag{7.2}$$

As the device is operated in the triode region, the drain current $i_{\mathrm{ds}}(t)$ is obtained as

$$i_{\mathrm{ds}}(t) = v_{\mathrm{ds}}(t) g_{\mathrm{ds}}(t) = v_{\mathrm{RF}}(t) g_{\mathrm{ds}}(t) \tag{7.3}$$

with the time-varying channel conductance $g_{\mathrm{ds}}(t)$. For strong inversion, the channel conductance can be approximated as [209]

$$\begin{aligned} g_{\mathrm{ds}}(t) &= \frac{W}{L}\mu C_{\mathrm{ox}}(v_{\mathrm{gs}}(t) - V_{\mathrm{th}} - v_{\mathrm{ds}}/2) \\ &= \frac{W}{L}\mu C_{\mathrm{ox}}(v_{\mathrm{RF}}(t)/2 + V_g - V_{\mathrm{th}}) \end{aligned} \tag{7.4}$$

where W and L correspond to the width and length of the channel, C_{ox} to the oxide capacitance per unit area, μ to the carrier mobility, and V_{th} to the threshold voltage. The combination of Eq. 7.3 and Eq. 7.4 leads to the following square law relation:

$$i_{\mathrm{ds}}(t) = \frac{W}{L}\mu C_{\mathrm{ox}}(v_{\mathrm{RF}}(t)^2/2 + v_{\mathrm{RF}}(t)(V_g - V_{\mathrm{th}})) \tag{7.5}$$

The dc current response I_{ds} can be calculated for a time-harmonic ac input signal $v_{\mathrm{RF}}(t) = V_{\mathrm{RF}} \sin(\omega t)$, after discarding the RF and it's harmonic terms, as

$$I_{\mathrm{ds}} = \frac{W}{L}\mu C_{\mathrm{ox}} V_{\mathrm{RF}}^2/4 \tag{7.6}$$

This dc current can be extracted from the drain terminal in a short circuit output mode as in a transimpedance amplifier followed by a low-pass filter.

With a detector power input P_{in}, the current responsivity I_{v} can be expressed as

$$I_v = \frac{I_{\mathrm{ds}}}{P_{\mathrm{in}}} = I_{\mathrm{ds}}\frac{R_{\mathrm{in}}}{V_{\mathrm{RF}}^2} = \frac{W}{L}\mu C_{\mathrm{ox}} R_{\mathrm{in}}/4 \tag{7.7}$$

where R_{in} is the real part of the detector RF input impedance. Simulation

results for $I_{\rm v}$ versus gate-bias are plotted in Fig. 7-2(b) (dashed line) for constant input power. A 0.25-μm-long and 0.72-μm-wide NMOS transistor with a threshold voltage of 0.61 V was used in this simulation as reported in [208]. Maximum short-circuit current responsivity is obtained above the threshold voltage. The slow roll-off of $I_{\rm v}$ with respect to high gate bias ($V_{\rm g} \gg V_{\rm th}$) is caused by internal current shunting.

The input power can also be detected as voltage by open circuit mode by a voltage amplifier followed by a low-pass filter. The detected voltage $V_{\rm ds}$ at the drain is generated by the current $I_{\rm ds}$ and the dc conductance $G_{\rm ds}$ of the channel. For strong inversion and the quasi-static analysis this is given by

$$V_{\rm ds} = \frac{I_{\rm ds}}{G_{\rm ds}} = \frac{V_{\rm RF}}{4(V_g - V_{\rm th})} \tag{7.8}$$

as long as the $V_{\rm ds}$ is small enough for the transistor to remain in the triode region. Hence, the voltage responsivity $R_{\rm v}$ can be written as [208]

$$R_v = \frac{V_{\rm ds}}{P_{\rm in}} = \frac{\frac{V_{\rm RF}^2}{4(V_g - V_{\rm th})}}{V_{\rm RF}^2/R_{\rm in}} = \frac{R_{\rm in}}{4(V_g - V_{\rm th})} \tag{7.9}$$

The simulated voltage responsivity is plotted also in Fig. 7-2(b) (solid line) as predicted in Eq. 7.9. For strong inversion, the responsivity rolls off faster with increased bias than in the case of current readout. Maximum responsivity is obtained in the subthreshold region since the detection current is generated across a larger internal dc resistance.

For input frequencies well above the transit frequency, we will consider the non quasi-static (NQS) analysis with a distributed RC model of the FET channel as shown in Fig. 7-3(a,b). Each segment resembles a quasi-static self-mixing detector as of Fig. 7-2(a), where the transistor is replaced by the segment conductance $g_{n-1}(v)$ and the external $C_{gd,ext}$ is provided by C_n. Kir-

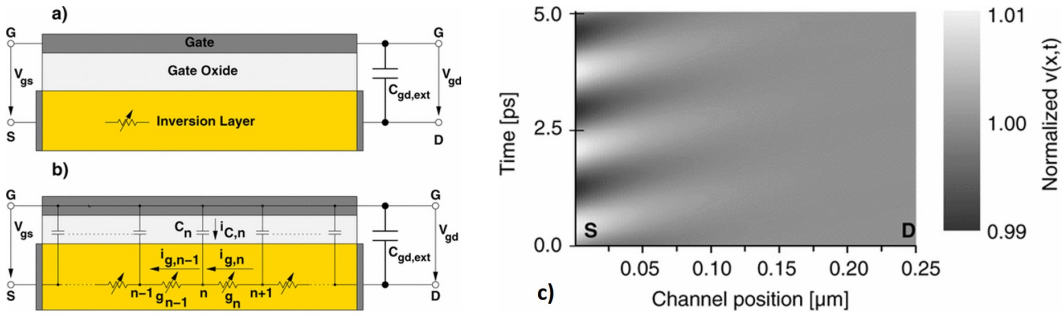

Figure 7-3: Non Quasi-static (NQS) analysis of self-mixing. (a) Resistive self-mixing with a lumped transistor and external $C_{gd,ext}$ and, (b) the NQS model with distributed gate-channel capacitance C_n. (c) Numerical solution of the time and position dependent gate-to-channel voltage $v(x,t)$ described by Eq. 7.14 for a 0.25 μm device excited at the source-gate junction (left) with a small 600 GHz signal. [208]

choff's junction rule at node n yields

$$i_{g,n-1} - i_{g,n} = i_{C,n} \tag{7.10}$$

This equation is equivalent to

$$g_{n-1}(v_{n-1} - v_n) - g_n(v_n - v_{n+1}) = C_n \frac{d}{dt}(v_n) \tag{7.11}$$

where each conductance g_n can be further expressed by a conductivity per unit length $G(v(x,t))$, which depends on the local gate-to-channel voltage $v(x,t)$ and the segment length Δx as follows:

$$g_n = \frac{G(v(n\Delta x, t))}{\Delta x} \tag{7.12}$$

Similarly, the individual segment capacitors can be expressed as

$$C_n = C_{\text{ox}} W \Delta x \tag{7.13}$$

where C_{ox} is the gate capacitance per unit area and W is the width of the device. After combining equations 7.11, 7.12, 7.13, and reducing the difference equation to a partial differential equation, for strong inversion it can be shown

as [208]

$$\frac{\partial}{\partial x}\left[\mu\left(v(x,t)-V_{\mathrm{th}}\right)\frac{\partial v(x,t)}{\partial x}\right]=\frac{\partial}{\partial t}v(x,t) \tag{7.14}$$

IT can be seen from Eq. 7.14, the NQS response is only dependent on the carrier mobility μ and the bias voltage $V_g - V_{\mathrm{th}}$. The NQS self-mixing response can be obtained by solving Eq. 7.14 with the following boundary conditions:

$$v(0,t) = V_{\mathrm{RF}} \sin \omega t + V_g \tag{7.15}$$

$$v(L,t) = V_g \tag{7.16}$$

Fig. 7-3(c) shows a 600 GHz numerical solution of Eq. 7.14 for the normalized gate-to-channel voltage $v(x,t)$ in a 0.25μm NMOS device as reported in [208]. The initially applied voltage propagates through the channel from the source (left) towards the drain (right) while it exhibits an exponential damping. After 0.1 μm, the signal is heavily attenuated, and the channel has essentially reached the drain potential. Hence, efficient resistive mixing takes place close to the source while the rest of the device acts as distributed capacitance C_{gd} and parasitic series resistance. This allows a long-channel device to be used for direct power detection even at terahertz frequencies. Distributed resistive self-mixing confines the mixing action to a much smaller section of the transistor and charges do not need to propagate through the entire length of the device. However, it is expected that the use of a shorter device will improve the detection performance as the thermal noise contribution from the non-modulated part of the channel is reduced. A shorter device implemented in a more advanced process technology is also likely to have smaller parasitic substrate capacitances, thus increasing the responsivity.

7.3 Metamaterial based Terahertz CMOS Detector Design

7.3.1 Terahertz Detection using Source-Driven Self-Mixing Architecture

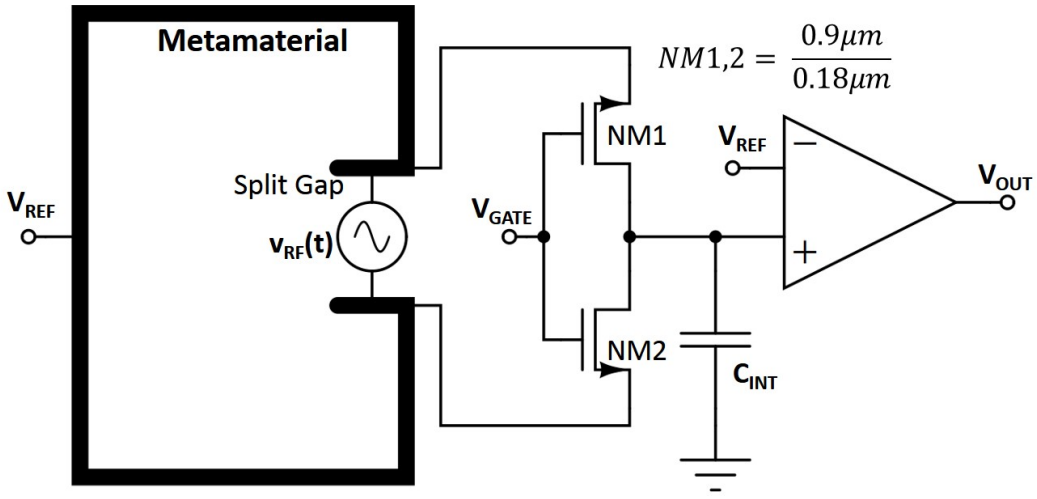

Figure 7-4: Schematic diagram of the differentially configured source-driven distributed-mixing terahertz square-law power detector.

In the previous section we described the terahertz detection principle using a gate and drain driven circuit topology. The same result can be achieved by driving the source end, with the gate and drain as virtual ground. The advantage of this method is it's broadband nature and architecturally suits well for terahertz detection with metamaterials.

Fig. 7-4 shows a simplified circuit schematic of the implemented terahertz detector using source-driven distributive self-mixing. In contrast to the gate-drain coupling approach used in the previous section, the RF power from the metamaterial is provided to the source terminals of the two NMOS transistors NM1 and NM2 in the present design. The gate and drain terminals of the transistors are connected to DC bias voltages, thus creating virtual grounds for the RF voltage. In a balanced configuration, half of the RF signal generated by the metamaterial split gap appears as a V_{gs} voltage across the gate-source

Transistor	W(μm)/L(μm)
NM1-4	0.9/0.18
NM5	10/1.2
NM6,7	10/2
NM8,9	10/4
NM10	30/0.18
PM1,2	10/0.18
PM3,4	5/2
PM5,6	20/0.25
PM7	10/0.25
PM8	60/0.18

Table 7.2: Transistor sizes for the terahertz detector circuit in Fig. 7-5

junctions of each transistor and contributes to the distributed self-mixing process in the channel. The rectified output current is extracted from the shared drain node and integrated on a on-chip capacitor which is compared with a reference using an operational amplifier to indicate terahertz detection. This configuration eliminates the need for quarter-wave stubs and coupling capacitors, which are necessary in the gate-driven detector design [208] in order to tie the RF potential of the gate and drain together and to provide isolation of the output port from the antenna. Hence, a wider operating bandwidth can be obtained with the source-driven detector than with the gate-driven one.

7.3.2 Circuit Architecture for Terahertz Detection

The architecture for terahertz detection of each pixel is based on the source-driven self-mixing principle as describe in the previous section (7.3.1). Fig. 7-5 shows a simplified schematic of the implemented architecture in 0.18 μm CMOS technology. The core of the THz detector circuit is a series connected NMOS pair, NM1 and NM2, with their sources connected to the split gap of a metamaterial unit cell in each pixel.

During the *reset phase* (ϕ is high), the integration cap C_{int} and the gate of PM1 and PM2 are connected to the bias voltage V_{ref}. Similarly, the gate of

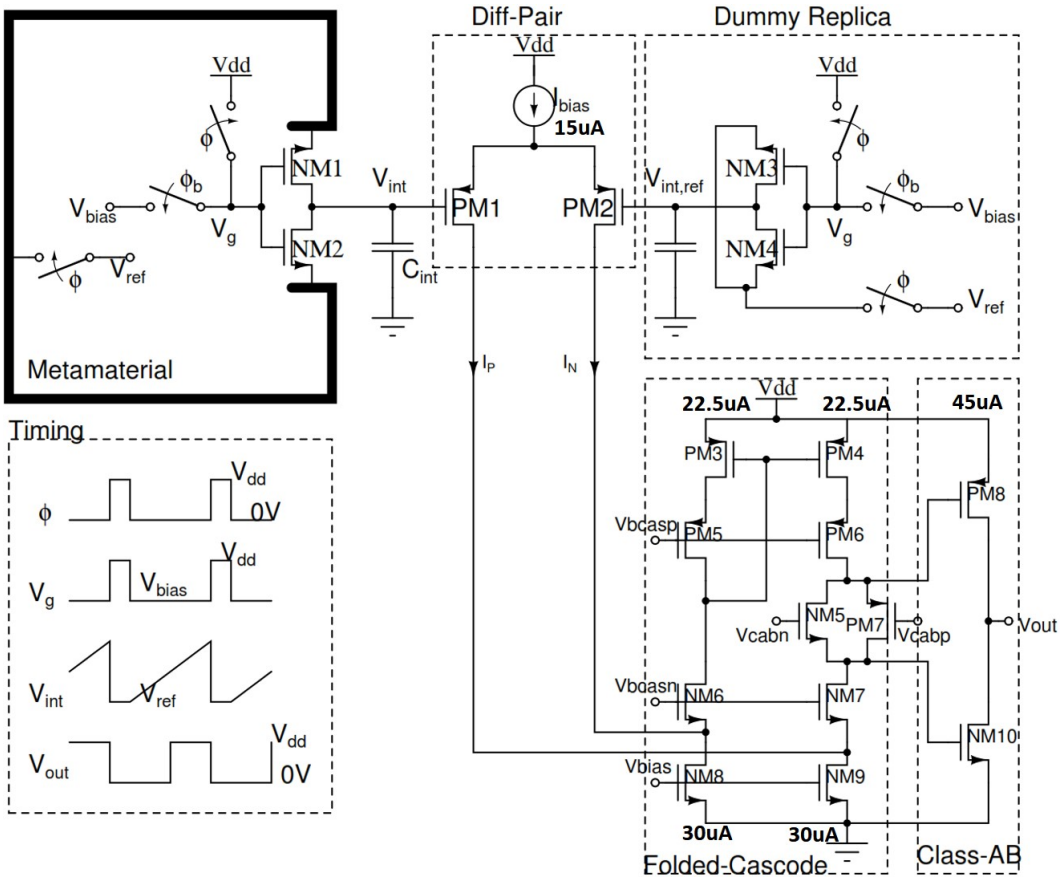

Figure 7-5: Circuit architecture for terahertz detection. A pair of NMOS (NM1 and NM2) are connected between the metamaterial split gap in the source-driven configuration. During the *reset phase* (ϕ is high), the integration cap C_{int} and the gate of PM1 and PM2 are connected to the bias voltage V_{ref}. During the *detection phase* (ϕ is low), the metamaterial is disconnected from the bias voltage and the electric field generated in the split gap will generate a DC current in NM1 and NM2 that is integrated on C_{int}. A dummy replica is used to generate the reference for the diff-pair and mimic all the switching effects of NM1 and NM2. The differential current generated from the differential pair (diff-pair) PM1 and PM2 is fed into a folded cascode stage that converts the differential current to voltage output. And the folded cascode is followed by a class-AB output stage to drive small resistive load. A simplified timing signal with associated voltage is shown in lower left inset. DC bias currents for the main branches are shown in the figure and all transistor sizes are tabulated in table 7.2.

PM2 is connected to V_{ref} through the dummy transistors NM3 and NM4. This sets a equal currents in the differential stage branches PM1 and PM2. The dummy replica stage assures that the diff-pair reference mimics any switching effects associated with the detector NMOS pair NM1 and NM2. Please note, any random or systematic mismatch in PM1 and PM2 can be corrected by adjusting one of the V_{ref} voltages.

During the *detection phase* (ϕ is low), the metamaterial is disconnected from the bias voltage and the terahertz electric field generated in the split gap will generate a DC current in NM1 and NM2 that is integrated on C_{int}. This integrated voltage creates a differential current in the differential pair (diff-pair) , PM1 and PM2, since the reference side of the diff-pair (gate of PM2) should hold constant. The differential current generated from the diff-pair is fed into a folded cascode stage (PM3-PM6, NM6-NM9) [209] with a combined class-AB output stage (PM7, PM8, NM5, NM10) that converts the differential current to voltage output. The purpose of the class-AM output stage is to be able to drive small resistive load.

Finally, the output of the folded cascode stage will be a periodic signal with the same periodicity as ϕ, with the pulse width proportional to the incident THz power which is shown in a simplified timing diagram in the lower-left inset of Fig. 7-5.

7.4 Metamaterial Design for Terahertz Detection

As detailed in section 7.3.1, the method for THz detection is to use the concentrated electric field in a metamaterial split gap to create a DC current using a pair of source-driven NFETs. So the metamaterials design will primarily focus on maximizing the electric field in the split gap. The first experimental demonstration of metamaterial perfect absorber (MPA) in 2008 [73] used split

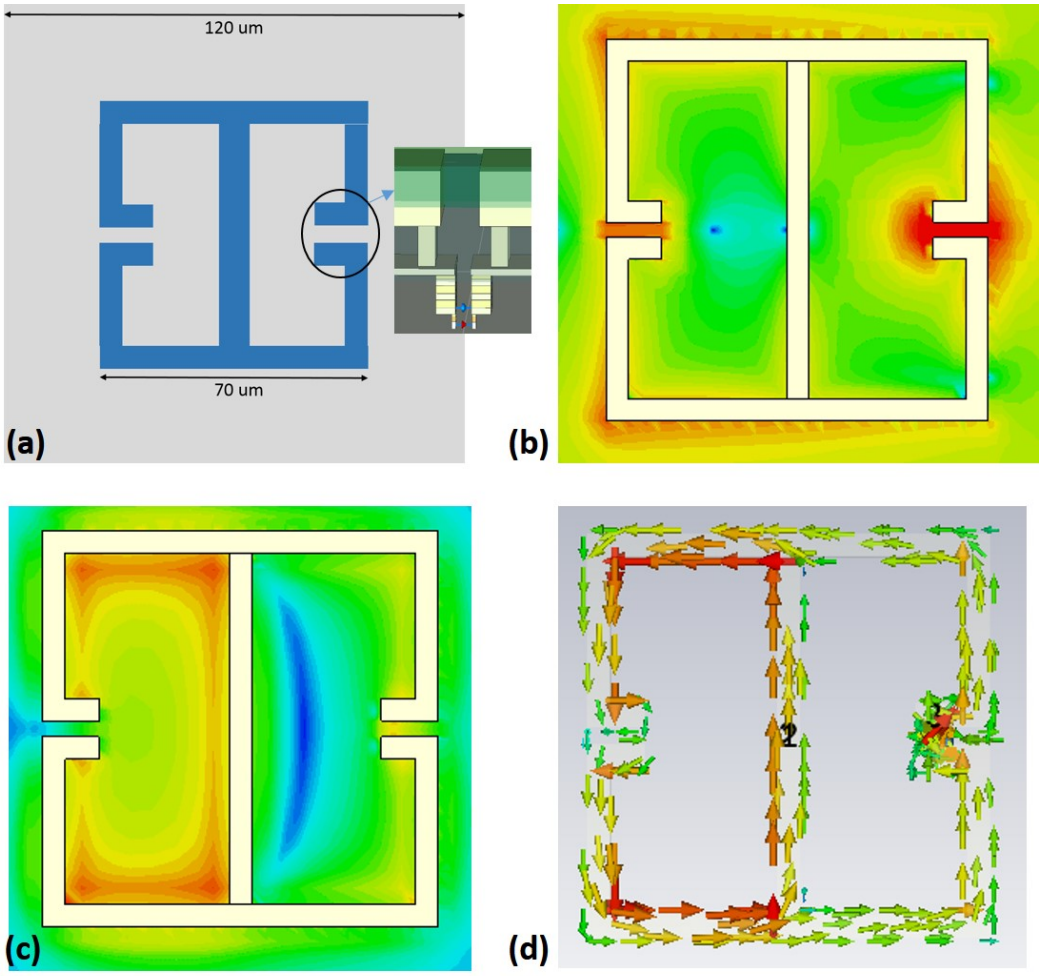

Figure 7-6: Metamaterial design and EM simulation results. (a) ELC with unit size of 70 μm designed to resonate at 325 GHz. The NFET detector is placed underneath one of the split gaps with the drains of the NFETs connected to the split gap through a set of vias as shown in the inset. (b-d) Resonant field and current distribution at the metamaterial plane, (b) electric field distribution (c) magnetic field distribution (d) surface current distribution.

ring and a cut wire underneath to absorb EM radiation at a desired frequency. It was shown in that work that most of the absorbed energy was in dielectric losses occurring in between the two metamaterial elements where the electric field is large. Unfortunately, that is not an ideal location for THz detection in planar semiconductor technology.

Since we are trying to maximize the electric field at the gap, it was natural to choose the electrical-LC (ELC) resonator shown in Fig. 7-6(a). The unit size is 70 μm and repeated every 120 μm. The pair of NFET detector is placed underneath one of the split gap and the drains of the NFETs are connected to the split gap with a set of vertical vias as shown in the inset. For EM simulations, a discrete port with a impedance of 300 Ω at the end of the vias is used to represent the lumped circuit equivalent of the NFET detector. Fig. 7-6(b-d) shows the resonant field and current distributions at the metamaterial plane at 325 GHz. The electric field plot in Fig. 7-6(b) shows the enhanced electric field in the split gap and asymmetry is due to the load on only one of the split gaps. Please note, there is no fundamental reason to have the detector only on one of the split gaps. You can put the detector on both the split gaps if the design rules allow you to. The magnetic field plot show in Fig. 7-6(c) also shows that the field in both the halfs do not cancel each other because of the asymmetric load. That is not an issue with our design since we are not trying to create an effective material.

The key transfer function for our detector is the voltage output of the discrete for a given incident THz power in a unit cell of 120x120 μm^2. Fig. 7-7(a) shows a peak of 9.27 V/W at 325 GHz. The S11 reflection plot in Fig. 7-7(b) shows that the peaks for the effective medium is not necessarily same as that of peak THz detection.

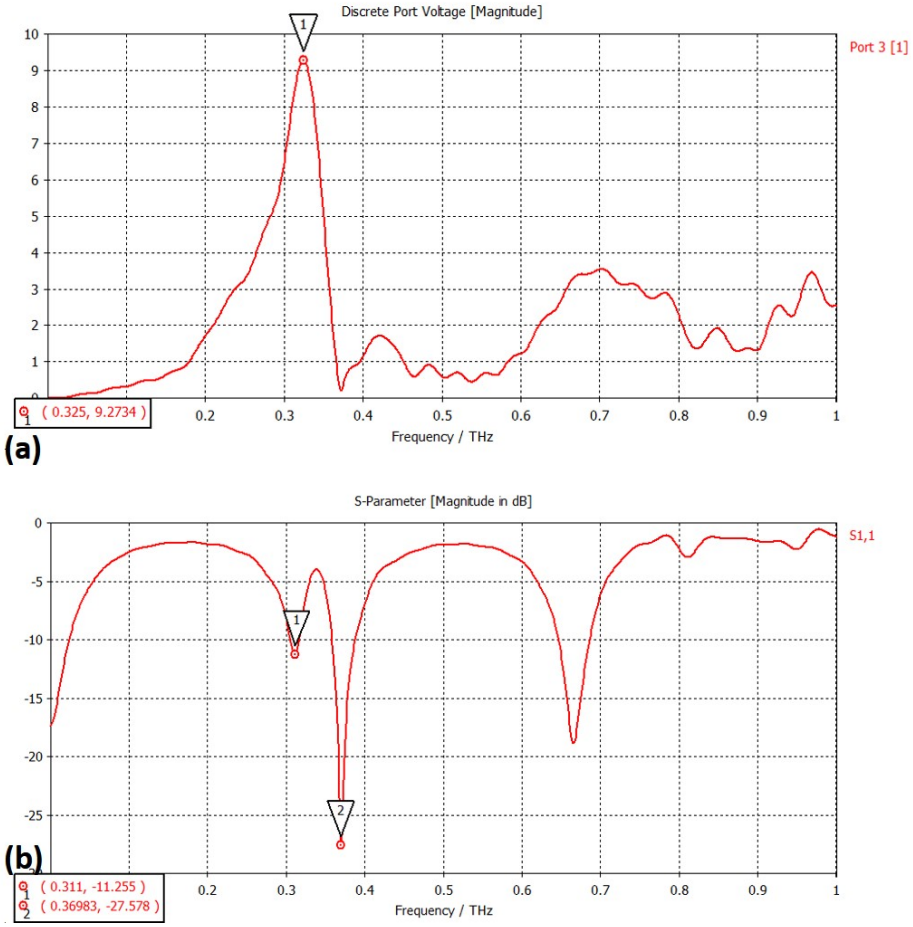

Figure 7-7: (a) Voltage at the discrete port for 1W of incident power on each unit cell of 120x120 μm^2 (b) The reflection co-efficient S11 plot.

7.5 Design of the Test Chip in 0.18um CMOS Process

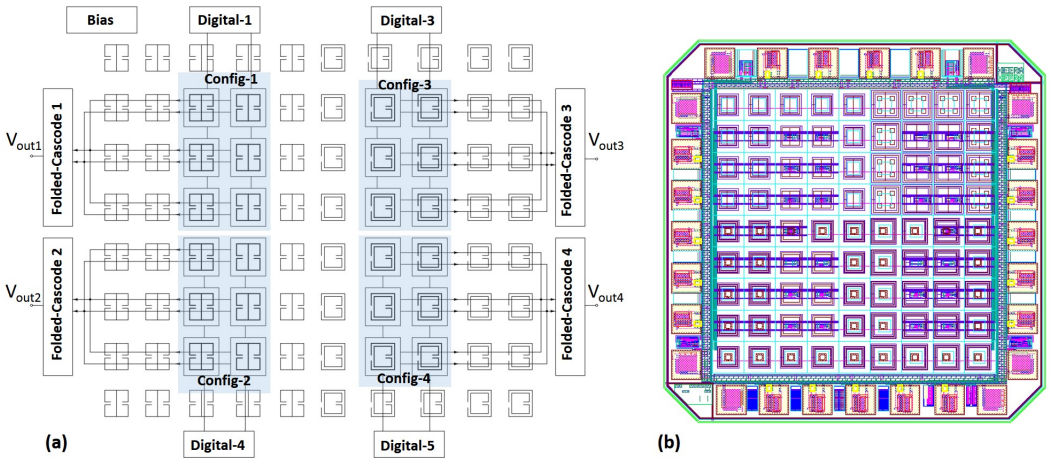

Figure 7-8: Design of the test chip in 0.18um CMOS process. (a) Schematic showing the placement and connection of the major blocks in THz CMOS FPA test chip. (b) Image of the layout of the complete test ship in the 0.18 μm CMOS process.

The schematic of the test chip and it's layout is shown in Fig. 7-8(a) and (b) respectively. The test chip contains four different configuration of meta-materials, two different types of resonators (ELC and SRRs) and for each resonator, two different frequencies as tabulated in table 7.3.

As shown in Fig. 7-8(a), each configuration consists of a 3x2 array of THz metamaterial detectors surrounded by passive metamaterials to minimize scattering effect. The diff-pair output of each element of the 3x2 array are connected to together and fed to a folded cascode stage, one for each configuration. The digital circuitry controls which element is chosen and the diff-pair output current of that selected element is connected to the folded cascode output stage to generate output. The digital block contains a set 16 registers that are used to program inter functionality. The registers are written using a shift register with a standard SPI protocol. A common bias block provides bias currents to all the blocks.

Configuration	Resonator	Unit Size (μm)	Frequency (GHz)
Config-1	SRR	80x80	320
Config-2	SRR	96x96	270
Config-3	ELC	70x70	325
Config-4	ELC	100x100	230

Table 7.3: Design parameters of the four different configurations in the test chip.

7.6 Circuit Simulation Results

In order to do a complete simulation, the THz voltage at the NFET detectors can be estimated at the metamaterials split gap from the simulation results shown in Fig, 7-7(a) for a known incident power. And that THz voltage can be applied in the circuit simulations provided non quasi-static (NQS) model is available for the FETs. Unfortunately, for our technology there were no NQS model available. For a 1 mW THz source illuminating about 2 mm^2 of the the detector area, about 1-5 pA of detector current.

All the circuits were simulated using the industry standard BSIM3 models provided by the foundry. Fig. 7-9 shows the simulation results for a single detector circuit. Fig. 7-9(a) shows the reset and detect pulse with a pulse width of 2 μs and a period of 200 μs. Fig. 7-9(b) shows the voltages on the two inputs of the differential pair, one is the detector integrating voltage and the other is a dummy replica. It can seen from the plot that both voltages are reset to 500 mV and when the switches are turned off/on for the detection phase, there is about 100 mV switching feedthrough and it can also be seen that both the integrating capacitors discharging strongly due to leakage currents of the parasitic diodes of the NFETs. That is the primary reason for creating the dummy replica stage to cancel the common non linear effects. The difference of the voltages are plotted in Fig. 7-9(c) for a 1 pA detection current. Fig. 7-9(d) shows the final output of the folded cascode output stage with a load of 100 kΩ resistor in parallel with 10 pF capacitor. The plot shows result of two detector currents, 1 pA (blue) and 2 pA (red). The method of measuring the

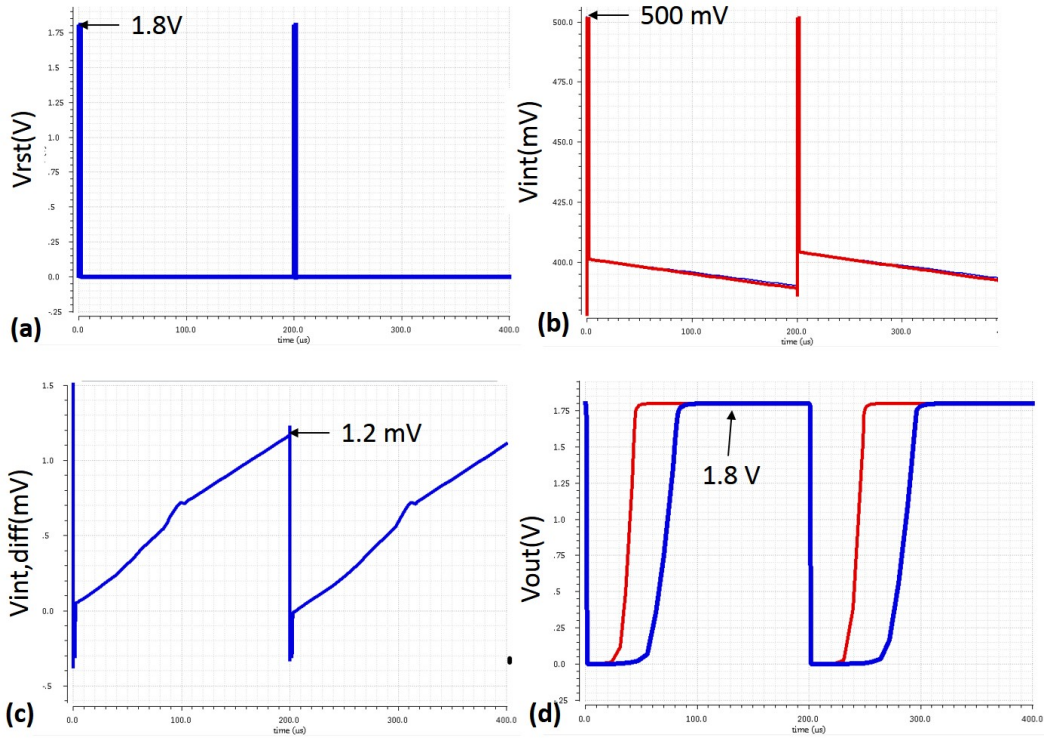

Figure 7-9: Circuit simulation results. (a) The reset and detect signal with reset width of 2 μs and period of 200 μs. (b) Integrating voltages on both sides of the differential pair with 1 pA current injected on the metamaterial side. (c) Differential voltage of the two integrated voltages. (d) Output voltage of the folded cascode for two different detection current 1 pA and 2 pA.

difference in the incident THz power is to measure the time difference between the rising output and back calculate based on the temperature, integrating capacitor and the load of the output stage. For a practical implementation, this can be achieved using on-chip calibration.

7.7 Summary

Given all the unique and useful properties of the terahertz imaging, it's very desirable to build low-cost terahertz imagers but it still remains an engineering challenge.

In this work, we demonstrate a path to realize a terahertz focal plane array (FPA) using a commercial 0.18 μm CMOS foundry process that is a mature low-cost semiconductor process suitable for high volume production. Through EM simulation and circuit simulation we have demonstrated a metamaterial based THz detectors at 230-325 GHz that can be used in a focal plane array. A complete CMOS chip is fabricated with four different designs and associated circuitry for a FPA operation.

With the complete chip designed and laid out using the foundry's design kit for 0.18 μm CMOS, the next step is to fabricate the chip and characterize it using a THz imaging setup. As mentioned in the previous chapter, apart from THz imaging, this FPA will be a key element in a THz communication system using our novel pictorial modulation described in the previous chapter.

Chapter 8

Conclusion

The objective of this thesis has been the analysis, design and application of terahertz metamaterial devices using commercial integrated circuit (IC) foundry process, to make terahertz systems available for mainstream applications.

Towards that goal, we have successfully designed and characterized a terahertz metamaterial modulator using a commercial galium arsenide (GaAs) process. Using a terahertz time-domain spectrometer (THz-TDS), we have demonstrated modulation of THz radiation at frequencies up to 10 MHz, and modulation depths of up to 33% at 0.46 THz with all electronic control. This is the fastest modulation speed reported to date as shown in Table 1.1. The reason for this achievement is result of using high electron mobility transistors (HEMTs) to control the metamaterial resonant frequency locally. This is also the first time, active transistors have been used in standard semiconductor process to dynamically control metamaterial properties at terahertz frequencies. It should be noted that, the modulation speed is limited by large parasitic capacitance that can minimized to achieve modulation speeds even in the gigahertz range. Additionally, the use of localized transistors resulted in a low-voltage (1V) operation of the device consuming sub-milliwatt of power.

Using the HEMT embedded metamaterial modulator, we have designed and implemented a terahertz ($\sim$0.45 THz) spatial light modulator (SLM) and experimentally demonstrated it's application using a single-pixel THz imaging

setup. Using continuous-wave terahertz spectrometer and the 2x2 SLM, we have presented the result of raster scanning a metal object occluded behind a polystyrene screen. This is also the first-time an all-solid state, electrically controlled THz SLM operating at 1V with modulation speed up to 10 MHz has been reported.

In this work, we make two important contribution towards terahertz wireless communication. First, we present a multi-level modulation method using spatial modulation instead of voltage modulation to achieve higher spectral efficiency in presence of voltage noise. We verify our claim with analysis and simulation to show two orders of magnitude improvement in symbol error rate (SER) for 20 dB SNR degradation due to transmit voltage noise. Second, we present a novel modulation technique using an array of THz spatial modulators that modulates the THz wave pictorially and the modulated wave is demodulated using a THz focal plane array. We show through simulation, bandwidth improvement almost linearly with a N-tile spatial modulator compared to a spatial modulation using a single-pixel detector. These two contributions are vital for the present time, given, the demand for high speed wireless access is increasing due to large amounts of data needed for new emerging applications.

Finally, we demonstrate a path to realize a terahertz focal plane array (FPA) using a commercial 0.18 μm CMOS foundry process that is a mature low-cost semiconductor process suitable for high volume production. Through EM simulation and circuit simulation we have demonstrated a metamaterial based THz detectors at 230-325 GHz that can be used in a focal plane array.

In conclusion, we have made significant contributions to bridge the "THz gap" by showing through analysis, design and applications, metamaterial based terahertz devices in matured low-cost semiconductor process that are on-chip integrable to create consumer grade terahertz imaging and communication systems.

Publications as of May 2016

Journals/Chapters

1. Saroj Rout and Sameer Sonkusale, **Pictorial modulation: a novel wireless modulation technique for higher spectral efficiency**. (in preparation)

2. Wangren Xu, Saroj Rout and Sameer Sonkusale, **Numerical Investigation on Terahertz and Far-infrared metamaterials using deeply scaled CMOS technology.** (in preparation)

3. Saroj Rout and Sameer Sonkusale, **A low-voltage high-speed terahertz spatial light modulator using active metamaterial**, *APL Photonics* (Submitted)

4. Saroj Rout and Sameer Sonkusale, **A wireless multi-level terahertz amplitude modulator using active metamaterial-based spatial light modulation**, *Optics Express* (Submitted)

5. Sameer Sonkusale, Wangren Xu, and Saroj Rout., **Active metamaterials for modulation and detection**, *CMC: Computers, Materials & Continua*, **39**(3):301-315, 2014

6. Saroj Rout, D. Shrekenhamer, A. C. Strikwerda, C. Bingham, R. D. Averitt, S. Sonkusale, and W. J. Padilla, **High speed terahertz modulation from metamaterials with embedded high electron mobility transistors**, *Opt. Express*, **19**:10, pp. 9968-9975, May 2011

Conferences/Chapters

1. Saroj Rout and Sameer Sonkusale, **Design and simulation of terahertz focal plane array in 0.18 μm CMOS**, *SPIE Photonics West 2017* (In preparation)

2. Saroj Rout and Sameer Sonkusale, **A low-voltage high-speed terahertz spatial light modulator using active metamaterial**, *SPIE Photonics West 2017* (In preparation)

3. Sameer Sonkusale, Wangren Xu, Saroj Rout, Guoqing Fu, and Pramod Singh, **Terahertz metamaterials for modulation and detection**, *SPIE Sensing Technology+ Applications*, p:948306-948306. International Society for Optics and Photonics, 2015

4. Saroj Rout and Sameer Sonkusale, **Real-time continuous-wave amplitude terahertz modulation system based on active metamaterials**, *International Conference on Metamaterials, Photonic Crystals and Plasmonics (6th) (META '15)*, p:1450, 2015

5. P. Singh, S. Rout, J. Hopwood, and S. Sonkusale., **Metamaterials for wireless generation of microplasma array**, *International Conference on Metamaterials, Photonic Crystals and Plasmonics (6th) (META '15)*, p:1466, 2015

6. D. Shrekenhamer, S. Rout, A. C. Strikwerda, C. Bingham, R. D. Averitt, S. Sonkusale, W. J. Padilla, **High Speed Terahertz Modulation from Metamaterials with Embedded High Electron Mobility Transistors**, *Intl. Congress on Advanced Elecromagnetic Materials in Microwave and Optics, Metamaterials*, 2011.

7. S. Rout, D. Shrekenhamer, S. Sonkusale, and W. Padilla, **Embedded HEMT/metamaterial composite devices for active terahertz modulation**, *IEEE Photonics Society's 23rd Annual Meeting*, pp. 437-438, 2010

Patents

8. S. Sonkusale, W. Padilla, and S. Rout, **Active Manipulation of Electromagnetic Wave Propagation in Metamaterials**, U.S. Patent WO/2012/06134511-May-2012.

Appendix A

Electromagnetic Waves

A.1 Helmholtz's Equation

Taking the curl of $\nabla \times \mathbf{E} + \frac{\partial \mathbf{B}}{\partial t} = 0$ in equation 2.1 [154]:

$$\begin{aligned} \nabla \times (\nabla \times \mathbf{E}) &= -\nabla \times \left(\frac{\partial \mathbf{B}}{\partial t} \right) \\ \nabla(\nabla \cdot \mathbf{E}) - \nabla^2 \mathbf{E} &= -\mu\epsilon \frac{\partial^2 \mathbf{E}}{\partial t} \\ \nabla^2 \mathbf{E} + \mu\epsilon \frac{\partial^2 \mathbf{E}}{\partial t} &= 0 \end{aligned} \tag{A.1}$$

Similarly, the other part of the Helmholtz's equation can be solved by taking curl of $\nabla \times \mathbf{H} - \frac{\partial \mathbf{D}}{\partial t} = 0$ in equation 2.1.

A.2 Electromagnetic Waves *are* Transverse

Let us consider a plane wave (in x-direction) that satisfies both Maxwell's and Helmholtz's equation

$$\begin{aligned} \mathbf{E}(\mathbf{x}, t) &= \mathbf{E}_0 e^{i(kx - \omega t)} \\ \mathbf{B}(\mathbf{x}, t) &= \mathbf{B}_0 e^{i(kx - \omega t)} \end{aligned} \tag{A.2}$$

Whereas every solution to Maxwell's equations (in empty space or non-conductors) must obey the wave equation, the converse is *not* true; it imposes special constraints on $\mathbf{E}_0$ and $\mathbf{B}_0$. Let us consider $\mathbf{E}(\mathbf{x}, t)$ with three orthogonal components as

$$\mathbf{E}(\mathbf{x}, t) = (\mathbf{E}_{0x} + \mathbf{E}_{0y} + \mathbf{E}_{0z})\, e^{i(kx-\omega t)} \tag{A.3}$$

Since $\nabla \cdot \mathbf{E} = 0$,

$$\frac{\partial \mathbf{E}_{0x} e^{ikx}}{\partial x} + \frac{\partial \mathbf{E}_{0y} e^{ikx}}{\partial y} + \frac{\partial \mathbf{E}_{0z} e^{ikx}}{\partial z} = 0 \tag{A.4}$$

Equation A.4 is satisfied only if

$$\mathbf{E}_{0x} = 0 \tag{A.5}$$

Similarly, it can be shown that

$$\mathbf{B}_{0x} = 0 \tag{A.6}$$

Moreover, it can be shown from Faraday's law, $\nabla \times \mathbf{E} = -\partial \mathbf{B}/\partial t$ that

$$\mathbf{B}_0 = \frac{k}{\omega} \left(\hat{i} \times \mathbf{E}_0 \right) \tag{A.7}$$

Thus, equations A.5-A.7 show that the EM plane wave needs to be *transverse* with the vectors $\mathbf{B}_0, \mathbf{E}_0, k$ forming a right-handed triplet.

Bibliography

[1] Hu Tao, W.J. Padilla, Xin Zhang, and R.D. Averitt. **Recent Progress in Electromagnetic Metamaterial Devices for Terahertz Applications**. *Selected Topics in Quantum Electronics, IEEE Journal of*, **17**(1):92 –101, February 2011. 1, 2, 11

[2] Gwyn P Williams. **Filling the THz gap–high power sources and applications**. *Reports on Progress in Physics*, **69**(2):301–326, February 2006. 1, 2, 3, 62, 88

[3] P.H. Siegel. **Terahertz technology**. *IEEE Transactions on Microwave Theory and Techniques*, **50**(3):910–928, March 2002. 1, 3, 8, 9

[4] J. M. Chamberlain. **Where optics meets electronics: recent progress in decreasing the terahertz gap**. *Philosophical Transactions of the Royal Society of London A: Mathematical, Physical and Engineering Sciences*, **362**(1815):199–213, February 2004. 3

[5] A. Maestrini, J. Ward, J. Gill, H. Javadi, E. Schlecht, G. Chattopadhyay, F. Maiwald, N. R. Erickson, and I. Mehdi. **A 1.7-1.9 THz local oscillator source**. *IEEE Microwave and Wireless Components Letters*, **14**(6):253–255, June 2004. 3

[6] Masayoshi Tonouchi. **Cutting-edge terahertz technology**. *Nat Photon*, **1**(2):97–105, February 2007. 3

[7] Daniel Mittleman. *Sensing with Terahertz Radiation*. Springer, February 2013. 3

[8] Wayne S. Holland, Jane S. Greaves, B. Zuckerman, R. A. Webb, Chris McCarthy, Iain M. Coulson, D. M. Walther, William R. F. Dent, Walter K. Gear, and Ian Robson. **Submillimetre images of dusty debris around nearby stars**. *Nature*, **392**(6678):788–791, April 1998. 3

[9] N. C. Luhmann Jr and W. A. Peebles. **Instrumentation for magnetically confined fusion plasma diagnostics**. *Review of Scientific Instruments*, **55**(3):279–331, March 1984. 3

[10] Martin van Exter, Ch Fattinger, and D. Grischkowsky. **Terahertz time-domain spectroscopy of water vapor**. *Optics Letters*, **14**(20):1128–1130, October 1989. 4

[11] Martin van Exter and Daniel R. Grischkowsky. **Characterization of an optoelectronic terahertz beam system**. *Microwave Theory and Techniques, IEEE Transactions on*, **38**(11):1684–1691, November 1990. 4, 53, 54, 55

[12] Robert A. Kaindl, Marc A. Carnahan, Joseph Orenstein, Daniel S. Chemla, Hans M. Christen, Hong-Ying Zhai, Mariappan Paranthaman, and Doug H. Lowndes. **Far-Infrared Optical Conductivity Gap in Superconducting MgB2 Films**. *Physical Review Letters*, **88**(2):027003, December 2001. 4

[13] A. G Markelz, A Roitberg, and E. J Heilweil. **Pulsed terahertz spectroscopy of DNA, bovine serum albumin and collagen between 0.1 and 2.0 THz**. *Chemical Physics Letters*, **320**(12):42–48, March 2000. 4

[14] Samuel P. Mickan, Abdellah Menikh, Haibo Liu, Carmen A. Mannella, Robert MacColl, Derek Abbott, Jesper Munch, and X.-C. Zhang. **Label-free bioaffinity detection using terahertz technology**. *Physics in Medicine and Biology*, **47**(21):3789, October 2002. 4

[15] D. M. Mittleman, M. Gupta, R. Neelamani, R. G. Baraniuk, J. V. Rudd, and M. Koch. **Recent advances in terahertz imaging**. *Applied Physics B*, **68**(6):1085–1094, June 1999. 4

[16] Wai Lam Chan, Jason Deibel, and Daniel M. Mittleman. **Imaging with terahertz radiation**. *Reports on Progress in Physics*, **70**(8):1325, August 2007. 4

[17] T. M. Korter and D. F. Plusquellic. **Continuous-wave terahertz spectroscopy of biotin: vibrational anharmonicity in the far-infrared**. *Chemical Physics Letters*, **385**(12):45–51, February 2004. 4, 62, 88, 107

[18] Nicholas Karpowicz, Hua Zhong, Cunlin Zhang, Kuang-I Lin, Jenn-Shyong Hwang, Jingzhou Xu, and X.-C. Zhang. **Compact continuous-wave subterahertz system for inspection applications**. *Applied Physics Letters*, **86**(5):054105–054105–3, 2005. 4, 5, 6, 62, 68

[19] Kodo Kawase, Yuichi Ogawa, Yuuki Watanabe, and Hiroyuki Inoue. **Non-destructive terahertz imaging of illicit drugs using spectral fingerprints**. *Optics Express*, **11**(20):2549–2554, October 2003. 4, 62, 68

[20] Ruth M. Woodward, Vincent P. Wallace, Richard J. Pye, Bryan E. Cole, Donald D. Arnone, Edmund H. Linfield, and Michael Pepper. **Terahertz Pulse Imaging of ex vivo Basal Cell Carcinoma**. *Journal of Investigative Dermatology*, **120**(1):72–78, January 2003. 4, 62, 88, 107

[21] Bradley Ferguson and Xi-Cheng Zhang. **Materials for terahertz science and technology**. *Nature Materials*, **1**(1):26–33, September 2002. 4

[22] P. Y. Han, G. C. Cho, and X.-C. Zhang. **Time-domain transillumination of biological tissues with terahertz pulses**. *Optics Letters*, **25**(4):242–244, February 2000. 4

[23] Thomas Kleine-Ostmann and Tadao Nagatsuma. **A Review on Terahertz Communications Research**. *Journal of Infrared, Millimeter, and Terahertz Waves*, **32**(2):143–171, January 2011. 4, 5, 88, 100

[24] Radoslaw Piesiewicz, Thomas Kleine-Ostmann, Norman Krumbholz, Daniel Mittleman, Martin Koch, Joerg Schoebel, and Thomas Kurner. **Short-Range Ultra-Broadband Terahertz Communications: Concepts and Perspectives**. *Antennas and Propagation Magazine, IEEE*, **49**(6):24–39, December 2007.

[25] John Federici and Lothar Moeller. **Review of terahertz and subterahertz wireless communications**. *Journal of Applied Physics*, **107**(11):111101, June 2010. 5, 88, 100

[26] Tadao Nagatsuma, H. J. Song, Y. Fujimoto, K. Miyake, A. Hirata, K. Ajito, A. Wakatsuki, T. Furuta, N. Kukutsu, and Y. Kado. **Giga-bit wireless link using 300-400 GHz bands**. In *Tech. Dig. IEEE International Topical Meeting on Microwave Photonics*, 2009. 6, 7, 10

[27] H. A. Gebbie, N. W. B. Stone, and F. D. Findlay. **A Stimulated Emission Source at 0.34 Millimetre Wave-length**. *Nature*, **202**:685, May 1964. 8

[28] T. S. Hartwick, D. T. Hodges, D. H. Barker, and F. B. Foote. **Far infrared imagery**. *Applied Optics*, **15**(8):1919–1922, August 1976. 8

[29] D. H. Auston, A. M. Glass, and P. LeFur. **Tunable farinfrared generation by difference frequency mixing of dye lasers in reduced (black) lithium niobate**. *Applied Physics Letters*, **23**(1):47–48, July 1973. 8

[30] D. H. Auston and K. P. Cheung. **Coherent time-domain far-infrared spectroscopy**. *JOSA B*, **2**(4):606–612, April 1985. 8

[31] Alfred P. DeFonzo, Madhuri Jarwala, and Charles Lutz. **Transient response of planar integrated optoelectronic antennas**. *Applied Physics Letters*, **50**(17):1155–1157, April 1987.

[32] Peter R. Smith, David H. Auston, and Martin C. Nuss. **Subpicosecond photoconducting dipole antennas**. *Quantum Electronics, IEEE Journal of*, **24**(2):255–260, February 1988.

[33] Ch Fattinger and D. Grischkowsky. **Terahertz beams**. *Applied Physics Letters*, **54**(6):490–492, February 1989.

[34] D. Grischkowsky, Sren Keiding, Martin van Exter, and Ch. Fattinger. **Far-infrared time-domain spectroscopy with terahertz beams of dielectrics and semiconductors**. *Journal of the Optical Society of America B*, **7**(10):2006, October 1990. 8

[35] B. B. Hu and M. C. Nuss. **Imaging with terahertz waves**. *Optics Letters*, **20**(16):1716–1718, August 1995. 8

[36] Daniel M. Mittleman, Stefan Hunsche, Luc Boivin, and Martin C. Nuss. **T-ray tomography**. *Optics Letters*, **22**(12):904–906, June 1997. 8

[37] K. McClatchey, M. T. Reiten, and R. A. Cheville. **Time resolved synthetic aperture terahertz impulse imaging**. *Applied Physics Letters*, **79**(27):4485–4487, December 2001. 8

[38] Timothy D. Dorney, Jon L. Johnson, J. Van Rudd, Richard G. Baraniuk, William W. Symes, and Daniel M. Mittleman. **Terahertz reflection imaging using Kirchhoff migration**. *Optics Letters*, **26**(19):1513–1515, October 2001.

[39] Bradley Ferguson, Shaohong Wang, Doug Gray, Derek Abbot, and X.-C. Zhang. **T-ray computed tomography**. *Optics Letters*, **27**(15):1312–1314, August 2002. 8

[40] Alan WeiMin Lee and Qing Hu. **Real-time, continuous-wave terahertz imaging by use of a microbolometer focal-plane array**. *Optics Letters*, **30**(19):2563–2565, October 2005. 8

[41] Q. Wu, T. D. Hewitt, and X.-C. Zhang. **Twodimensional electrooptic imaging of THz beams**. *Applied Physics Letters*, **69**(8):1026–1028, August 1996. 8

[42] M. Helm, E. Colas, P. England, F. DeRosa, and S. J. Allen Jr. **Observation of gratinginduced intersubband emission from GaAs/AlGaAs superlattices**. *Applied Physics Letters*, **53**(18):1714–1716, October 1988. 9

[43] Jerome Faist, Federico Capasso, Deborah L. Sivco, Carlo Sirtori, Albert L. Hutchinson, and Alfred Y. Cho. **Quantum Cascade Laser**. *Science*, **264**(5158):553–556, April 1994. 9

[44] Rdeger Khler, Alessandro Tredicucci, Fabio Beltram, Harvey E. Beere, Edmund H. Linfield, A. Giles Davies, David A. Ritchie, Rita C. Iotti, and Fausto Rossi. **Terahertz semiconductor-heterostructure laser**. *Nature*, **417**(6885):156–159, May 2002. 9

[45] Alan W. M. Lee, Qi Qin, Sushil Kumar, Benjamin S. Williams, Qing Hu, and John L. Reno. **Real-time terahertz imaging over a standoff distance (>25meters)**. *Applied Physics Letters*, **89**(14):141125, October 2006. 9, 62

[46] S. Fathololoumi, E. Dupont, C. W. I. Chan, Z. R. Wasilewski, S. R. Laframboise, D. Ban, A. Mtys, C. Jirauschek, Q. Hu, and H. C. Liu. **Terahertz quantum cascade lasers operating up to 200 K with optimized oscillator strength and improved injection tunneling**. *Optics Express*, **20**(4):3866–3876, February 2012. 9

[47] L. Li, L. Chen, J. Zhu, J. Freeman, P. Dean, A. Valavanis, A. G. Davies, and E. H. Linfield. **Terahertz quantum cascade lasers with >1 W output powers**. *Electronics Letters*, **50**(4):309–311, February 2014. 9

[48] Tg Phillips and J. Keene. **Submillimeter Astronomy**. *Proceedings of the Ieee*, **80**(11):1662–1678, November 1992. WOS:A1992KC43400002. 9

[49] Juraj Darmo, Vincas Tamosiunas, Gernot Fasching, Josef Krll, Karl Unterrainer, Mattias Beck, Marcella Giovannini, Jerome Faist, Christian Kremser, and Paul Debbage. **Imaging with a Terahertz quantum cascade laser**. *Optics Express*, **12**(9):1879–1884, May 2004. 9

[50] Seongsin M. Kim, Fariba Hatami, James S. Harris, Allison W. Kurian, James Ford, Douglas King, Giacomo Scalari, Marcella Giovannini, Nicolas Hoyler, Jerome Faist, and Geoff Harris. **Biomedical terahertz imaging with a quantum cascade laser**. *Applied Physics Letters*, **88**(15):153903, April 2006.

[51] Stefano Barbieri, Jesse Alton, Colin Baker, Thomas Lo, Harvey E. Beere, and David Ritchie. **Imaging with THz quantum cascade lasers using a Schottky diode mixer**. *Optics Express*, **13**(17):6497–6503, August 2005.

[52] K. Lien Nguyen, Michael L. Johns, Lynn F. Gladden, Christopher H. Worrall, Paul Alexander, Harvey E. Beere, Michael Pepper, David A. Ritchie, Jesse Alton, Stefano Barbieri, and Edmund H. Linfield. **Three-dimensional imaging with a terahertz quantum cascade laser**. *Optics Express*, **14**(6):2123–2129, March 2006. 9

[53] H. A. Gebbie. **Some uses of submillimeter waves in science and technology**. In *Proc. Symposium on Submillimeter Waves*. Polytechnic Press of the Polytechnic Institute of Brooklyn, 1970. 9

[54] Akihiko Hirata, Toshihiko Kosugi, Hiroyuki Takahashi, Ryouichi Yamaguchi, Fumito Nakajima, Tomofumi Furuta, Hiroshi Ito, Hirohiko Sugahara, Yasuhiro Sato, and Tadao Nagatsuma. **120-GHz-band millimeter-wave photonic wireless link for 10-Gb/s data transmission**. *Microwave Theory and Techniques, IEEE Transactions on*, **54**(5):1937–1944, May 2006. 9

[55] Akihiko Hirata, Hiroyuki Takahashi, Ryoichi Yamaguchi, Toshihiko Kosugi, Koichi Murata, Tadao Nagatsuma, Naoya Kukutsu, and Yuichi Kado. **Transmission Characteristics of 120-GHz-Band Wireless Link Using Radio-on-Fiber Technologies**. *Lightwave Technology, Journal of*, **26**(15):2338–2344, August 2008. 9

[56] Toshihiko Kosugi, Masami Tokumitsu, Koichi Murata, Takatomo Enoki, Hiroyuki Takahashi, Akihiko Hirata, and Tadao Nagatsuma. **120-GHz Tx/Rx Waveguide Modules for 10-Gbit/s Wireless Link System**. pages 25–28. IEEE, November 2006. 9

[57] Victor Veselago. **The Electrodynamics of Substances with Simultaneously Negative Values ϵ and μ**. *Soviet Physics Uspekh*, **10**(4):509–514, 1968. 12, 13, 14, 32

[58] G. D. Malyuzhinets. **A note on the radiation principle**. *Zhurnal technicheskoi fiziki*, **21**(8):940–942, 1951. 12

[59] L Mandlshtam. **Group Velocity in Crystal Lattice**. *Zhurnal Eksperimentalnoii Teoreticheskoi fiziki*, **15**:476–478, 1945.

[60] D. V. Sivukhin. **The energy of electromagnetic waves in dispersive media**. *Opt. Spektrosk*, **3**(308-31):2, 1957.

[61] Sergei A. Tretyakov. **Research on negative refraction and backward-wave media: A historical perspective**. In *Negative Refraction: Revisiting Electromagnetics from Microwave to Optics, EPFL Latsis Symposium, Lausanne, Switzerland*, pages 30–35, 2005. 12

[62] D.R. Smith, D.C. Vier, W. Padilla, S.C. Nemat-Nasser, and S. Schultz. **Loop-wire medium for investigating plasmons at microwave frequencies**. *Applied Physics Letters*, **75**(10):1425–1427, 1999. 12

[63] D. R. Smith, Willie J. Padilla, D. C. Vier, S. C. Nemat-Nasser, and S. Schultz. **Composite Medium with Simultaneously Negative Permeability and Permittivity**. *Physical Review Letters*, **84**(18):4184, May 2000. 12, 14, 18

[64] D. R. Smith, J. B. Pendry, and M. C. K. Wiltshire. **Metamaterials and Negative Refractive Index**. *Science*, **305**(5685):788–792, August 2004. 12

[65] John Pendry. **Optics: All smoke and metamaterials**. *Nature*, **460**(7255):579–580, July 2009.

[66] John Pendry. **Photonics: Metamaterials in the sunshine**. *Nature Materials*, **5**(8):599–600, August 2006.

[67] Willie J. Padilla, Dimitri N. Basov, and David R. Smith. **Negative refractive index metamaterials**. *Materials Today*, **9**(7-8):28–35, July 2006. 33

[68] Vladimir M. Shalaev. **Optical negative-index metamaterials**. *Nature Photonics*, **1**(1):41–48, January 2007. 12

[69] Koray Aydin, Irfan Bulu, and Ekmel Ozbay. **Focusing of electromagnetic waves by a left-handed metamaterial flat lens**. *Optics Express*, **13**(22):8753–8759, October 2005. 12

[70] J. B. Pendry. **Negative Refraction Makes a Perfect Lens**. *Physical Review Letters*, **85**(18):3966, October 2000.

[71] Nicholas Fang, Hyesog Lee, Cheng Sun, and Xiang Zhang. **SubDiffraction-Limited Optical Imaging with a Silver Superlens**. *Science*, **308**(5721):534–537, April 2005.

[72] Xiang Zhang and Zhaowei Liu. **Superlenses to overcome the diffraction limit**. *Nature Materials*, **7**(6):435–441, June 2008. 12

[73] N. I. Landy, S. Sajuyigbe, J. J. Mock, D. R. Smith, and W. J. Padilla. **Perfect Metamaterial Absorber**. *Physical Review Letters*, **100**(20):207402, May 2008. 12, 21, 119

[74] Hu Tao, Nathan I. Landy, Christopher M. Bingham, Xin Zhang, Richard D. Averitt, and Willie J. Padilla. **A metamaterial absorber for the terahertz regime: design, fabrication and characterization**. *Optics Express*, **16**(10):7181–7188, May 2008. 12, 14, 18, 20, 21

[75] J. B. Pendry, D. Schurig, and D. R. Smith. **Controlling Electromagnetic Fields**. *Science*, **312**(5781):1780–1782, June 2006. 12

[76] Boubacar Kant, Dylan Germain, and Andr de Lustrac. **Experimental demonstration of a nonmagnetic metamaterial cloak at microwave frequencies**. *Physical Review B*, **80**(20):201104, November 2009.

[77] Hu Tao, N.I. Landy, Kebin Fan, A.C. Strikwerda, W.J. Padilla, R.D. Averitt, and Xin Zhang. **Flexible terahertz metamaterials: towards a terahertz metamaterial invisible cloak**. In *Electron Devices Meeting, 2008. IEDM 2008. IEEE International*, pages 1–4, December 2008.

[78] D. Schurig, J.J. Mock, B.J. Justice, S.A. Cummer, J.B. Pendry, A.F. Starr, and D.R. Smith. **Metamaterial electromagnetic cloak at microwave frequencies**. *Science*, **314**(5801):977–980, 2006. 12

[79] Xian Qi Lin, Tie Jun Cui, Jessie Yao Chin, Xin Mi Yang, Qiang Cheng, and Ruopeng Liu. **Controlling electromagnetic waves using tunable gradient dielectric metamaterial lens**. *Applied Physics Letters*, **92**(13):131904, April 2008. 12

[80] Ruopeng Liu, Xin Mi Yang, Jonah G. Gollub, Jack J. Mock, Tie Jun Cui, and David R. Smith. **Gradient index circuit by waveguided metamaterials**. *Applied Physics Letters*, **94**(7):073506, February 2009.

[81] D. R. Smith, J. J. Mock, A. F. Starr, and D. Schurig. **Gradient index metamaterials**. *Physical Review E*, **71**(3):036609, March 2005.

[82] Ruopeng Liu, Chunlin Ji, Jack J. Mock, T. Cui, and D.R. Smith. **Random gradient index metamaterials**. In *2008 International Workshop on Metamaterials*, pages 248–250, November 2008. 12

[83] W. J. Padilla, A. J. Taylor, C. Highstrete, Mark Lee, and R. D. Averitt. **Dynamical Electric and Magnetic Metamaterial Response at Terahertz Frequencies**. *Physical Review Letters*, **96**(10):107401, March 2006. 13, 24, 28, 41

[84] Hou-Tong Chen, Willie J. Padilla, Joshua M. O. Zide, Arthur C. Gossard, Antoinette J. Taylor, and Richard D. Averitt. **Active terahertz metamaterial devices**. *Nature*, **444**(7119):597–600, November 2006. 13, 14, 18, 24, 28, 41, 43, 48, 51, 64, 68, 71, 74, 88

[85] Hou-Tong Chen, John F. O'Hara, Abul K. Azad, Antoinette J. Taylor, Richard D. Averitt, David B. Shrekenhamer, and Willie J. Padilla. **Experimental demonstration of frequency-agile terahertz metamaterials**. *Nat Photon*, **2**(5):295–298, May 2008. 13, 23, 24, 41, 42, 43

[86] Hou-Tong Chen, Willie J. Padilla, Joshua M. O. Zide, Seth R. Bank, Arthur C. Gossard, Antoinette J. Taylor, and Richard D. Averitt. **Ultrafast optical switching of terahertz metamaterials fabricated on ErAs/GaAs nanoisland superlattices**. *Optics Letters*, **32**(12):1620–1622, June 2007. 13, 24, 28, 41, 68

[87] Hou-Tong Chen, Sabarni Palit, Talmage Tyler, Christopher M Bingham, Joshua M. O Zide, John F OHara, David R Smith, Arthur C Gossard, Richard D Averitt, Willie J Padilla, Nan M Jokerst, and Antoinette J Taylor. **Hybrid metamaterials enable fast electrical modulation of freely propagating terahertz waves**. *Applied Physics Letters*, **93**(9):091117–091117–3, September 2008. 13, 28, 43, 44

[88] Hou-Tong Chen, Willie J. Padilla, Michael J. Cich, Abul K. Azad, Richard D. Averitt, and Antoinette J. Taylor. **A metamaterial solid-state terahertz phase modulator**. *Nature Photonics*, **3**(3):148, February 2009. 13, 27, 43, 48, 74, 88

[89] T. Driscoll, S. Palit, M. M. Qazilbash, M. Brehm, F. Keilmann, Byung-Gyu Chae, Sun-Jin Yun, Hyun-Tak Kim, S. Y. Cho, N. Marie Jokerst, D. R. Smith, and D. N. Basov. **Dynamic tuning of an infrared hybrid-metamaterial resonance using vanadium dioxide**. *Applied Physics Letters*, **93**(2):024101, July 2008. 13, 26, 43

[90] Hu Tao, A. C. Strikwerda, K. Fan, W. J. Padilla, X. Zhang, and R. D. Averitt. **Reconfigurable Terahertz Metamaterials**. *Physical Review Letters*, **103**(14):147401, October 2009. 13, 14, 18, 26

[91] Ruopeng Liu, Tie Jun Cui, Da Huang, Bo Zhao, and David R. Smith. **Description and explanation of electromagnetic behaviors in artificial metamaterials based on effective medium theory**. *Physical Review E*, **76**(2):026606, 2007. 13, 14, 18, 40, 44

[92] David R. Smith and John B. Pendry. **Homogenization of metamaterials by field averaging (invited paper)**. *Journal of the Optical Society of America B*, **23**(3):391–403, March 2006. 13

[93] J. B. Pendry, A. J. Holden, W. J. Stewart, and I. Youngs. **Extremely Low Frequency Plasmons in Metallic Mesostructures**. *Physical Review Letters*, **76**(25):4773, June 1996. 14, 17

[94] A. Demetriadou and J. B. Pendry. **Taming spatial dispersion in wire metamaterial**. *Journal of Physics: Condensed Matter*, **20**(29):295222, July 2008. 14

[95] M. C. K. Wiltshire, J. B. Pendry, and J. V. Hajnal. **Chiral Swiss rolls show a negative refractive index**. *Journal of Physics: Condensed Matter*, **21**(29):292201, July 2009. 14

[96] J.B. Pendry, A.J. Holden, D.J. Robbins, and W.J. Stewart. **Magnetism from conductors and enhanced nonlinear phenomena**. *Microwave Theory and Techniques, IEEE Transactions on*, **47**(11):2075–2084, 1999. 14, 18

[97] G. Dolling, C. Enkrich, M. Wegener, J. F. Zhou, C. M. Soukoulis, and S. Linden. **Cut-wire pairs and plate pairs as magnetic atoms for optical metamaterials**. *Optics Letters*, **30**(23):3198–3200, December 2005. 14

[98] Vladimir M. Shalaev, Wenshan Cai, Uday K. Chettiar, Hsiao-Kuan Yuan, Andrey K. Sarychev, Vladimir P. Drachev, and Alexander V. Kildishev. **Negative index of refraction in optical metamaterials**. *Optics Letters*, **30**(24):3356–3358, December 2005. 14

[99] Carsten Rockstuhl, Christoph Menzel, Thomas Paul, Thomas Pertsch, and Falk Lederer. **Light propagation in a fishnet metamaterial**. *Physical Review B*, **78**(15):155102, October 2008. 14

[100] Jason Valentine, Shuang Zhang, Thomas Zentgraf, Erick Ulin-Avila, Dentcho A. Genov, Guy Bartal, and Xiang Zhang. **Three-dimensional optical metamaterial with a negative refractive index**. *Nature*, **455**(7211):376–379, September 2008. 14

[101] David Shrekenhamer, Saroj Rout, Andrew C. Strikwerda, Chris Bingham, Richard D. Averitt, Sameer Sonkusale, and Willie J. Padilla. **High speed terahertz modulation from**

metamaterials with embedded high electron mobility transistors. *Optics Express*, **19**(10):9968–9975, May 2011. 14, 18, 24, 27, 28, 44, 46, 48, 64, 74, 85, 88, 100

[102] David Shrekenhamer, Wangren Xu, Suresh Venkatesh, David Schurig, Sameer Sonkusale, and Willie J. Padilla. **Experimental Realization of a Metamaterial Detector Focal Plane Array**. *Physical Review Letters*, **109**(17):177401, October 2012.

[103] D. Li, Y. Xie, J. Zhang, J. Li, and Z. Chen. **Multilayer Filters with Split-Ring Resonator Metamaterials**. *Journal of Electromagnetic Waves and Applications*, **22**(10):1420–1429, 2008.

[104] C. Rockstuhl, T. Zentgraf, H. Guo, N. Liu, C. Etrich, I. Loa, K. Syassen, J. Kuhl, F. Lederer, and H. Giessen. **Resonances of split-ring resonator metamaterials in the near infrared**. *Applied Physics B*, **84**(1-2):219–227, July 2006.

[105] Jiafu Wang, Shaobo Qu, Zhuo Xu, Jieqiu Zhang, Hua Ma, Yiming Yang, and Chao Gu. **Broadband planar left-handed metamaterials using split-ring resonator pairs**. *Photonics and Nanostructures - Fundamentals and Applications*, **7**(2):108–113, May 2009. 14, 18

[106] David Shrekenhamer. *Dynamic Control of Metamaterials at Terahertz Frequencies*. Ph.D. Dissertation, Boston College, Chestnut Hill, Massachusetts, USA, May 2013. 15, 17

[107] S. OBrien and J. B. Pendry. **Magnetic activity at infrared frequencies in structured metallic photonic crystals**. *Journal of Physics: Condensed Matter*, **14**(25):6383, June 2002. 14

[108] R.N. Bracewell. **Analogues of an ionized medium**. *Wireless Engineer*, **31**:320, 1954. 17

[109] W. Rotman. **Plasma simulation by artificial dielectrics and parallel-plate media**. *Antennas and Propagation, IRE Transactions on*, **10**(1):82–95, 1962. 18

[110] R. Ulrich. **Far-infrared properties of metallic mesh and its complementary structure**. *Infrared Physics*, **7**(1):37–55, March 1967.

[111] T. Timusk and P.L. Richards. **NEAR MILLIMETER WAVE BANDPASS FILTERS.** *Applied Optics*, **20**(8):1355–1360, 1981. 17

[112] J.B. Pendry, A.J. Holden, D.J. Robbins, and W.J. Stewart. **Low frequency plasmons in thin-wire structures**. *Journal of Physics Condensed Matter*, **10**(22):4785–4809, 1998. 17

[113] D Schurig, J Mock, and D. R. Smith. **Electric-field-coupled resonators for negative permittivity metamaterials**. *Applied Physics Letters*, **88**(4):041109–041109–3, January 2006. 18, 44, 50

[114] W. J. Padilla, M. T. Aronsson, C. Highstrete, Mark Lee, A. J. Taylor, and R. D. Averitt. **Electrically resonant terahertz metamaterials: Theoretical and experimental investigations**. *Physical Review B*, **75**(4):041102, January 2007. 18, 20, 44, 50

[115] N. I. Landy, C. M. Bingham, T. Tyler, N. Jokerst, D. R. Smith, and W. J. Padilla. **Design, theory, and measurement of a polarization-insensitive absorber for terahertz imaging**. *Physical Review B*, **79**(12):125104, March 2009. 18, 21

[116] B. J. Arritt, D. R. Smith, and T. Khraishi. **Equivalent circuit analysis of metamaterial strain-dependent effective medium parameters**. *Journal of Applied Physics*, **109**(7):073512, 2011. 18, 40, 44

[117] T J Yen, W J Padilla, N Fang, D C Vier, D R Smith, J B Pendry, D N Basov, and X Zhang. **Terahertz magnetic response from artificial materials**. *Science (New York, N.Y.)*, **303**(5663):1494–1496, March 2004. 19, 20

[118] Abul K. Azad, Antoinette J. Taylor, Evgenya Smirnova, and John F. OHara. **Characterization and analysis of terahertz metamaterials based on rectangular split-ring resonators**. *Applied Physics Letters*, **92**(1):011119, January 2008. 20

[119] Christopher M. Bingham, Hu Tao, Xianliang Liu, Richard D. Averitt, Xin Zhang, and Willie J. Padilla. **Planar wallpaper group metamaterials for novel terahertz applications**. *Optics Express*, **16**(23):18565–18575, November 2008. 20

[120] Nikitas Papasimakis, Sukosin Thongrattanasiri, Nikolay I. Zheludev, and FJ Garca de Abajo. **The magnetic response of graphene split-ring metamaterials**. *Light: Science & Applications*, **2**(7):e78, July 2013. 20, 21

[121] Claire M. Watts, Xianliang Liu, and Willie J. Padilla. **Metamaterial Electromagnetic Wave Absorbers**. *Advanced Materials*, **24**(23):OP98–OP120, 2012. 21

[122] Wangren Xu, Willie J. Padilla, and Sameer Sonkusale. **Loss compensation in Metamaterials through embedding of active transistor based negative differential resistance circuits**. *arXiv:1204.6067 [physics]*, April 2012. 21

[123] Dexin Ye, Kihun Chang, Lixin Ran, and Hao Xin. **Microwave gain medium with negative refractive index**. *Nature Communications*, **5**, December 2014. 21

[124] Claire M. Watts, David Shrekenhamer, John Montoya, Guy Lipworth, John Hunt, Timothy Sleasman, Sanjay Krishna, David R. Smith, and Willie J. Padilla. **Terahertz compressive imaging with metamaterial spatial light modulators**. *Nature Photonics*, **8**, June 2014. 21, 64, 68, 70, 71

[125] David Shrekenhamer, Claire M. Watts, and Willie J. Padilla. **Terahertz single pixel imaging with an optically controlled dynamic spatial light modulator**. *Optics Express*, **21**(10):12507, May 2013. 21, 63, 64, 67, 68, 69

[126] D.L. Donoho. **Compressed sensing**. *IEEE Transactions on Information Theory*, **52**(4):1289–1306, April 2006. 22, 63, 66, 67, 107

[127] T. Vogel, G. Dodel, E. Holzhauer, H. Salzmann, and A. Theurer. **High-speed switching of far-infrared radiation by photoionization in a semiconductor**. *Applied Optics*, **31**(3):329–337, January 1992. 22, 28

[128] Tatsuo Nozokido, Hiroaki Minamide, and Koji Mizuno. **Modulation of submillimeter wave radiation by laserproduced free carriers in semiconductors**. *Electronics and Communications in Japan (Part II: Electronics)*, **80**(6):1–9, June 1997. 22, 28

[129] Takanori Okada and Koichiro Tanaka. **Photo-designed terahertz devices**. *Scientific Reports*, **1**:121, October 2011. 22

[130] Stefan Busch, Benedikt Scherger, Maik Scheller, and Martin Koch. **Optically controlled terahertz beam steering and imaging**. *Optics Letters*, **37**(8):1391–1393, April 2012. 22

[131] E. A. Shaner, J. G. Cederberg, and D. Wasserman. **Electrically tunable extraordinary optical transmission gratings**. *Applied Physics Letters*, **91**(18):181110, October 2007. 24

[132] Hou-Tong Chen, Hong Lu, Abul K. Azad, Richard D. Averitt, Arthur C. Gossard, Stuart A. Trugman, John F. OHara, and Antoinette J. Taylor. **Electronic control of extraordinary terahertz transmission through subwavelength metal hole arrays**. *Optics Express*, **16**(11):7641–7648, May 2008. 25, 28

[133] Jie Shu, Ciyuan Qiu, Victoria Astley, Daniel Nickel, Daniel M. Mittleman, and Qianfan Xu. **High-contrast terahertz modulator based on extraordinary transmission through a ring aperture**. *Optics Express*, **19**(27):26666–26671, December 2011. 25

[134] T Kleine-Ostmann, P Dawson, K Pierz, and M Koch. **Room-temperature operation of an electrically driven terahertz modulator**. *Applied Physics Letters*, **84**(18):3555–3557, April 2004. 25, 28, 44, 57

[135] Seung Hoon Lee, Muhan Choi, Teun-Teun Kim, Seungwoo Lee, Ming Liu, Xiaobo Yin, Hong Kyw Choi, Seung S. Lee, Choon-Gi Choi, Sung-Yool Choi, Xiang Zhang, and Bumki Min. **Switching terahertz waves with gate-controlled active graphene metamaterials**. *Nature Materials*, **11**(11):936–941, November 2012. 25, 26, 28

[136] Long Ju, Baisong Geng, Jason Horng, Caglar Girit, Michael Martin, Zhao Hao, Hans A. Bechtel, Xiaogan Liang, Alex Zettl, Y. Ron Shen, and Feng Wang. **Graphene plasmonics for tunable terahertz metamaterials**. *Nature Nanotechnology*, **6**(10):630–634, October 2011. 25

[137] Berardi Sensale-Rodriguez, Tian Fang, Rusen Yan, Michelle M. Kelly, Debdeep Jena, Lei Liu, and Huili (Grace) Xing. **Unique prospects for graphene-based terahertz modulators**. *Applied Physics Letters*, **99**(11):113104, September 2011.

[138] C.-C. Lee, S. Suzuki, W. Xie, and T. R. Schibli. **Broadband graphene electro-optic modulators with sub-wavelength thickness**. *Optics Express*, **20**(5):5264–5269, February 2012.

[139] Ming Liu, Xiaobo Yin, Erick Ulin-Avila, Baisong Geng, Thomas Zentgraf, Long Ju, Feng Wang, and Xiang Zhang. **A graphene-based broadband optical modulator**. *Nature*, **474**(7349):64–67, June 2011.

[140] Berardi Sensale-Rodriguez, Rusen Yan, Michelle M. Kelly, Tian Fang, Kristof Tahy, Wan Sik Hwang, Debdeep Jena, Lei Liu, and Huili Grace Xing. **Broadband graphene terahertz modulators enabled by intraband transitions**. *Nature Communications*, **3**:780, April 2012. 25, 26, 28, 64

[141] J. Gmez Rivas, M. Kuttge, H. Kurz, P. Haring Bolivar, and J. A. Snchez-Gil. **Low-frequency active surface plasmon optics on semiconductors**. *Applied Physics Letters*, **88**(8):082106, February 2006. 26

[142] Hou-Tong Chen, Hao Yang, Ranjan Singh, John F. OHara, Abul K. Azad, Stuart A. Trugman, Q. X. Jia, and Antoinette J. Taylor. **Tuning the Resonance in High-Temperature Superconducting Terahertz Metamaterials**. *Physical Review Letters*, **105**(24):247402, December 2010. 26, 28

[143] Marco Rahm, Jiu-Sheng Li, and Willie J. Padilla. **THz Wave Modulators: A Brief Review on Different Modulation Techniques**. *Journal of Infrared, Millimeter, and Terahertz Waves*, **34**(1):1–27, January 2013. 27, 28

[144] H. Alius and G. Dodel. **Amplitude-, phase-, and frequency modulation of far-infrared radiation by optical excitation of silicon**. *Infrared Physics*, **32**:1–11, 1991. 28

[145] T. Nozokido, H. Minamide, and K. Mizuno. **Generation of sub-millimeter wave short pulses and their measurements**. *RIKEN Review*, **11**(11), 1995. 28

[146] E. Hendry, M. J. Lockyear, J. Gmez Rivas, L. Kuipers, and M. Bonn. **Ultrafast optical switching of the THz transmission through metallic subwavelength hole arrays**. *Physical Review B*, **75**(23):235305, June 2007. 28

[147] Dibakar Roy Chowdhury, Ranjan Singh, John F. OHara, Hou-Tong Chen, Antoinette J. Taylor, and Abul K. Azad. **Dynamically reconfigurable terahertz metamaterial through photo-doped semiconductor**. *Applied Physics Letters*, **99**(23):231101, December 2011. 28

[148] Oliver Paul, Christian Imhof, Bert Lgel, Sandra Wolff, Jan Heinrich, Sven Hfling, Alfred Forchel, Remigius Zengerle, Ren Beigang, and Marco Rahm. **Polarization-independent active metamaterial for high-frequency terahertz modulation**. *Optics Express*, **17**(2):819–827, January 2009. 28, 43

[149] T. Driscoll, Hyun-Tak Kim, Byung-Gyu Chae, Bong-Jun Kim, Yong-Wook Lee, N. Marie Jokerst, S. Palit, D. R. Smith, M. Di Ventra, and D. N. Basov. **Memory Metamaterials**. *Science*, **325**(5947):1518–1521, September 2009. 28

[150] John David Jackson. *Classical Electrodynamics*. Wiley, 3rd edition, August 1998. 30, 33, 35

[151] Richard W. Ziolkowski and Ehud Heyman. **Wave propagation in media having negative permittivity and permeability**. *Physical Review E*, **64**(5):056625, October 2001. 32, 33

[152] Martin W. McCall, Akhlesh Lakhtakia, and Werner S. Weiglhofer. **The negative index of refraction demystified**. *European Journal of Physics*, **23**(3):353, May 2002. 32, 33

[153] I. V. Lindell, S. A. Tretyakov, K. I. Nikoskinen, and S. Ilvonen. **BW mediamedia with negative parameters, capable of supporting backward waves**. *Microwave and Optical Technology Letters*, **31**(2):129–133, October 2001. 33

[154] David J. Griffiths. *Introduction to Electrodynamics*. Pearson Higher Ed, January 2014. 34, 132

[155] Frederick Wooten. *Optical Properties of Solids*. Academic Press, October 2013. 35, 39

[156] D. R. Smith. **Analytic expressions for the constitutive parameters of magnetoelectric metamaterials**. *Physical Review E*, **81**(3):036605, March 2010. 40

[157] Lothar Mller, John Federici, Alexander Sinyukov, Chongjin Xie, Hee Chuan Lim, and Randy C. Giles. **Data encoding on terahertz signals for communication and sensing**. *Optics Letters*, **33**(4):393, 2008. 43

[158] Wai Lam Chan, Hou-Tong Chen, Antoinette J Taylor, Igal Brener, Michael J Cich, and Daniel M Mittleman. **A spatial light modulator for terahertz beams**. *Applied Physics Letters*, **94**(21):213511–213511–3, May 2009. 43, 64, 68, 71, 85

[159] Chao-Yuan Chen, Tsong-Ru Tsai, Ci-Ling Pan, and Ru-Pin Pan. **Room temperature terahertz phase shifter based on magnetically controlled birefringence in liquid crystals**. *Applied Physics Letters*, **83**(22):4497–4499, December 2003. 44, 57

[160] T. Kleine-Ostmann, K. Pierz, G. Hein, P. Dawson, M. Marso, and M. Koch. **Spatially resolved measurements of depletion properties of large gate two-dimensional electron gas semiconductor terahertz modulators**. *Journal of Applied Physics*, **105**(9):093707, May 2009. 44

[161] P.-C. Chao, M.S. Shur, R.C. Tiberio, K.H.G. Duh, P.M. Smith, J.M. Ballingall, P. Ho, and A. Jabra. **DC and microwave characteristics of sub-0.1-m gate-length planar-doped pseudomorphic HEMTs**. *Electron Devices, IEEE Transactions on*, **36**(3):461–473, 1989. 46, 47, 50, 74

[162] Gregory Snider. **1D Poisson Solver website: http://www3.nd.edu/~gsnider**, December 2015. 47

[163] E. Batke and D. Heitmann. **Rapid-scan Fourier transform spectroscopy of 2-D space charge layers in semiconductors**. *Infrared Physics*, **24**(2-3):189–197, May 1984. 47, 57

[164] P. J. Burke, I. B. Spielman, J. P. Eisenstein, L. N. Pfeiffer, and K. W. West. **High frequency conductivity of the high-mobility two-dimensional electron gas**. *Applied Physics Letters*, **76**(6):745, 2000. 47, 48, 57

[165] David Shrekenhamer, John Montoya, Sanjay Krishna, and Willie J. Padilla. **Four-Color Metamaterial Absorber THz Spatial Light Modulator**. *Advanced Optical Materials*, **1**(12):905–909, December 2013. 49, 68, 69, 70

[166] D. R. Smith, D. C. Vier, Th. Koschny, and C. M. Soukoulis. **Electromagnetic parameter retrieval from inhomogeneous metamaterials**. *Physical Review E*, **71**(3):036617, March 2005. 52

[167] Xudong Chen, Tomasz M. Grzegorczyk, Bae-Ian Wu, Joe Pacheco, and Jin Au Kong. **Robust method to retrieve the constitutive effective parameters of metamaterials**. *Physical Review E*, **70**(1):016608, July 2004.

[168] Xudong Chen, Bae-Ian Wu, Jin Au Kong, and Tomasz M. Grzegorczyk. **Retrieval of the effective constitutive parameters of bianisotropic metamaterials**. *Physical Review E*, **71**(4):046610, April 2005. 52

[169] P. Uhd Jepsen, R. H. Jacobsen, and S. R. Keiding. **Generation and detection of terahertz pulses from biased semiconductor antennas**. *JOSA B*, **13**(11):2424–2436, November 1996. 54, 55

[170] John F. OHara, J. M. O. Zide, A. C. Gossard, A. J. Taylor, and R. D. Averitt. **Enhanced terahertz detection via ErAs:GaAs nanoisland superlattices**. *Applied Physics Letters*, **88**(25):251119, June 2006. 55

[171] W. Knap, J. Lusakowski, T. Parenty, S. Bollaert, A. Cappy, V. V. Popov, and M. S. Shur. **Terahertz emission by plasma waves in 60 nm gate high electron mobility transistors**. *Applied Physics Letters*, **84**(13):2331–2333, March 2004. 57

[172] W. Knap, Y. Deng, S. Rumyantsev, J.-Q. L, M. S. Shur, C. A. Saylor, and L. C. Brunel. **Resonant detection of subterahertz radiation by plasma waves in a submicron field-effect transistor**. *Applied Physics Letters*, **80**(18):3433–3435, May 2002.

[173] Michael Dyakonov and Michael Shur. **Shallow water analogy for a ballistic field effect transistor: New mechanism of plasma wave generation by dc current**. *Physical Review Letters*, **71**(15):2465, October 1993.

[174] M. Dyakonov and M. Shur. **Detection, mixing, and frequency multiplication of terahertz radiation by two-dimensional electronic fluid**. *IEEE Transactions on Electron Devices*, **43**(3):380–387, March 1996. 57, 108

[175] Y. Cai, I. Brener, J. Lopata, J. Wynn, L. Pfeiffer, J. B. Stark, Q. Wu, X. C. Zhang, and J. F. Federici. **Coherent terahertz radiation detection: Direct comparison between free-space electro-optic sampling and antenna detection**. *Applied Physics Letters*, **73**(4):444, 1998. 60

[176] R. Plana, L. Escotte, O. Llopis, H. Amine, T. Parra, M. Gayral, and J. Graffeuil. **Noise in AlGaAs/InGaAs/GaAs pseudomorphic HEMTs from 10 Hz to 18 GHz**. *Electron Devices, IEEE Transactions on*, **40**(5):852–858, 1993. 60

[177] Zhiping Jiang and Xi-Cheng Zhang. **Terahertz imaging via electrooptic effect**. *IEEE Transactions on Microwave Theory and Techniques*, **47**(12):2644–2650, December 1999. 62

[178] E.J. Candes, J. Romberg, and T. Tao. **Robust uncertainty principles: exact signal reconstruction from highly incomplete frequency information**. *IEEE Transactions on Information Theory*, **52**(2):489–509, February 2006. 63, 66, 67, 107

[179] Dana Dudley, Walter M. Duncan, and John Slaughter. **Emerging digital micromirror device (DMD) applications**. **4985**, pages 14–25, 2003. 64

[180] J. Dunayevsky and D.M. Marom. **MEMS Spatial Light Modulator for Phase and Amplitude Modulation of Spectrally Dispersed Light**. *Journal of Microelectromechanical Systems*, **22**(5):1213–1221, October 2013. 64

[181] William P. Bleha and Lijuan Alice Lei. **Advances in Liquid Crystal on Silicon (LCOS) spatial light modulator technology**. **8736**, pages 87360A–87360A–8, 2013. 64, 72

[182] Zhaoyi Li and Nanfang Yu. **Modulation of mid-infrared light using graphene-metal plasmonic antennas**. *Applied Physics Letters*, **102**(13):131108, April 2013. 64

[183] Roderick D. Swift, Richard B. Wattson, John A. Decker, Ralph Paganetti, and Martin Harwit. **Hadamard transform imager and imaging spectrometer**. *Applied Optics*, **15**(6):1595–1609, June 1976. 65, 67

[184] Marcel J. E. Golay. **Multi-Slit Spectrometry**. *JOSA*, **39**(6):437–444, June 1949. 65

[185] Neil J. A. Sloane and Martin Harwit. **Masks for Hadamard transform optics, and weighing designs**. *Applied Optics*, **15**(1):107–114, January 1976. 66

[186] E. J. Candes and M. B. Wakin. **An Introduction To Compressive Sampling**. *IEEE Signal Processing Magazine*, **25**(2):21–30, March 2008. 68

[187] Wai Lam Chan, Kriti Charan, Dharmpal Takhar, Kevin F. Kelly, Richard G. Baraniuk, and Daniel M. Mittleman. **A single-pixel terahertz imaging system based on compressed sensing**. *Applied Physics Letters*, **93**(12):121105, September 2008. 68

[188] Martin van Exter and D. Grischkowsky. **Optical and electronic properties of doped silicon from 0.1 to 2 THz**. *Applied Physics Letters*, **56**(17):1694–1696, April 1990. 69

[189] Christian C. Nadell, Claire M. Watts, John A. Montoya, Sanjay Krishna, and Willie J. Padilla. **Single Pixel Quadrature Imaging with Metamaterials**. *Advanced Optical Materials*, **4**(1):66–69, January 2016. 71, 86

[190] Claire M. Watts, Christian C. Nadell, John Montoya, Sanjay Krishna, and Willie J. Padilla. **Frequency-division-multiplexed single-pixel imaging with metamaterials**. *Optica*, **3**(2):133–138, February 2016. 71, 86

[191] Salvatore Savo, David Shrekenhamer, and Willie J. Padilla. **Liquid Crystal Metamaterial Absorber Spatial Light Modulator for THz Applications**. *Advanced Optical Materials*, **2**(3):275–279, March 2014. 72

[192] **see Toptica Photonics website, http://www.toptica.com**, November 2015. 78

[193] A. Roggenbuck, H. Schmitz, A. Deninger, I. Camara Mayorga, J. Hemberger, R. Gusten, and M. Gruninger. **Coherent broadband continuous-wave terahertz spectroscopy on solid-state samples**. *New Journal of Physics*, **12**(4):043017, April 2010. 80

[194] Withawat Withayachumnankul and Derek Abbott. **Metamaterials in the Terahertz Regime**. *Photonics Journal, IEEE*, **1**(2):99–118, August 2009. 88

[195] Harald Haas and Stephen McLaughlin. *Next Generation Mobile Access Technologies: Implementing TDD*. Cambridge University Press, 2007. 88

[196] Leon Couch. *Digital & Analog Communication Systems, 7/E*. Pearson Education, September 2008. 95

[197] Michel C. Jeruchim. **Techniques for Estimating the Bit Error Rate in the Simulation of Digital Communication Systems**. *Selected Areas in Communications, IEEE Journal on*, **2**(1):153–170, January 1984. 97

[198] J. L. Hesler and T.W. Crowe. **Responsivity and noise measurements of zero-bias schottky diode detectors**. pages 89–92, Pasadena, 2007. 107, 108

[199] P. Helisto, A. Luukanen, L. Gronberg, J. S. Penttila, H. Seppa, H. Sipola, C. R. Dietlein, and E. N. Grossman. **Antenna-coupled microbolometers for passive THz direct detection imaging arrays**. pages 35–38. IEEE, September 2006. 107

[200] A. Tessmann, I. Kallfass, A. Leuther, H. Massler, M. Schlechtweg, and O. Ambacher. **Metamorphic MMICs for Operation Beyond 200 GHz**. In *Microwave Integrated Circuit Conference, 2008. EuMIC 2008. European*, pages 210–213, October 2008. 108

[201] S. Sankaran and K. K. O. **Schottky barrier diodes for millimeter wave detection in a foundry CMOS process**. *IEEE Electron Device Letters*, **26**(7):492–494, July 2005. 108

[202] A. Theuwissen. **CMOS image sensors: State-of-the-art and future perspectives**. In *Solid State Circuits Conference, 2007. ESSCIRC 2007. 33rd European*, pages 21–27, September 2007. 108

[203] R. A. Barret. **Broadband RF detector using FET**, 1987. 108

[204] H. G. Krekels, B. Schiek, and E. Menzel. **Power Detector with GaAs Field Effect Transistors**. **1**, pages 174–179. IEEE, September 1992. 108

[205] W. Knap, F. Teppe, Y. Meziani, N. Dyakonova, J. Lusakowski, F. Boeuf, T. Skotnicki, D. Maude, S. Rumyantsev, and M. S. Shur. **Plasma wave detection of sub-terahertz and terahertz**

radiation by silicon field-effect transistors. *Applied Physics Letters*, **85**(4):675–677, July 2004. 108

[206] R. Tauk, F. Teppe, S. Boubanga, D. Coquillat, W. Knap, Y. M. Meziani, C. Gallon, F. Boeuf, T. Skotnicki, C. Fenouillet-Beranger, D. K. Maude, S. Rumyantsev, and M. S. Shur. **Plasma wave detection of terahertz radiation by silicon field effects transistors: Responsivity and noise equivalent power**. *Applied Physics Letters*, **89**(25):253511, December 2006. 108

[207] U.R. Pfeiffer and E. Ojefors. **A 600-GHz CMOS focal-plane array for terahertz imaging applications**. In *Solid-State Circuits Conference, 2008. ESSCIRC 2008. 34th European*, pages 110 –113, September 2008. 108

[208] E. Ojefors, U.R. Pfeiffer, A. Lisauskas, and H.G. Roskos. **A 0.65 THz Focal-Plane Array in a Quarter-Micron CMOS Process Technology**. *Solid-State Circuits, IEEE Journal of*, **44**(7):1968 –1976, July 2009. 108, 109, 111, 113, 114, 115, 117

[209] Paul R. Gray, Paul J. Hurst, Stephen H. Lewis, and Robert G. Meyer. *Analysis and Design of Analog Integrated Circuits*. John Wiley & Sons, 5th edition, January 2009. 112, 119